MULTI-SCALE THERMAL AND STRUCTURAL CHARACTERIZATION OF CARBON FOAM FOR THE PARKER SOLAR PROBE THERMAL PROTECTION SYSTEM

by
Elizabeth Ann Congdon

A dissertation submitted to the Johns Hopkins University in conformity with the requirements for the degree of Doctor of Philosophy

Baltimore, Maryland
February 2021

ABSTRACT

Since the founding of the National Aeronautics and Space Administration (NASA), a top mission priority has been to study the Sun in situ. For sixty years, this mission remained just an aspiration of heliophysicists due to the inherent limitations of the engineering technology required to make the mission possible. One critical spacecraft element is the thermal protection system (TPS) or heat shield, a low mass self-supporting structure that required implementation of a structurally integral insulation sandwich panel.

For this multifunctional sandwich panel approach to be successful, the thermal and structural properties of the main insulative core, carbon foam, needed to be understood to validate that the TPS could survive the launch loading and the extreme temperatures at its perihelion. An extensive test program including coupon, subscale and full-scale evaluation was undertaken to determine the properties of this low-density lattice and to compliment full-scale modeling. Candidate foams, ranging from 3% to 10% relative density, were evaluated using both the guarded hot plate method and thermal diffusivity methods for effective thermal conductivity. The effective thermal conductivity was primarily driven by solid conductivity around room temperature and shown to follow simple Gibson and Ashby predictions. At temperatures beyond 900°C, radiation was much more important and the test data diverged from the model. These coupon-level tests were also used to show the influence of relative density and foam architecture on the effective thermal conductivity of these foams. Subscale thermal evaluation of a representative thickness was performed at Oak Ridge National

Laboratory (ORNL). The subscale results from this testing at temperatures above 900°C diverged from the coupon results and model predictions, indicating that thickness plays an important role in the overall effective thermal conductivity at these higher temperatures.

Structural testing of coupon, subscale and full-scale specimens were conducted in concert with the thermal experiments. Tension, compression and shear loading were executed in the three primary directions of the foam. The coupon results revealed anisotropy, which could not be explained by purely geometric structural anisotropy as advocated by Gibson and Ashby. Subscale bending tests were consistent with coupon test data but size effects were observed; the smaller region of elevated stress, associated with bending, resulted in lower variability than was seen in the uniaxially loaded coupons.

The data obtained in these experiments formed the baseline material properties database that was used for full scale modeling, which employed a margining approach and was dependent on material properties consistent with the success criteria for spaceflight missions. All full-scale units successfully survived acoustic, vibration and cold thermal testing and were used to certify the flight design. On August 12, 2018, the Parker Solar Probe (PSP) spacecraft lifted off from Cape Canaveral, FL on its way to the Sun. To date, it has successfully completed six passes around the Sun, and it has broken the record for being the closest manmade object to the Sun three times. The heat shield is performing as expected, and the mission has already returned groundbreaking science.

Primary Reader and Advisor: Professor Kevin Hemker

Secondary Readers: Professor Jamie Guest and Professor Jaafar El-Awady

ACKNOWLEDGEMENTS

To begin, I would like to thank my Ph.D. advisor, Professor Kevin J. Hemker for his support, guidance, patience, encouragement and mentoring over the last ten years. I was an unusual Ph.D. student and he saw my abilities even when I could not see them in myself. He was constantly encouraging me and supporting me throughout my time at Hopkins. I would also like to thank my readers Professor Jamie Guest and Professor Jaafar El-Awady for their time and support during this process.

If there is one thing that I have learned in the last 10 years, it is that I am someone who loves working with people. I have been lucky enough to be surrounded by wonderful, dedicated people who have generously taught me about materials, testing, life, and friendship. I like to say that my favorite part of my job is that no one person with all the time and knowledge can build a spacecraft. It takes hundreds of thousands of people working towards a singular goal. Before launch during press events, I would say we are going to rewrite science textbooks and that my children would learn about the Sun differently due to the work that we did. What is amazing is that is already true. I am humbled to be a small part of that. It is an understatement to say that this work would not have been possible without hundreds of people who supported me in big and small ways along the way. Specifically, I would like to thank Doug Mehoke for his mentoring, support, kindness and leadership. I would not be where I am today without you. Ed Schafer has taught me a lifetime of knowledge about structural materials and spacecraft and much of that is reflected here. Shelly Conkey has always supported me, guided me and taught me about technical matters and friendship. I am lucky to be

working with her currently on my second spacecraft. Luke Becker has been a constant supporter of mine and read through every chapter of this dissertation and for that I cannot thank him enough.

Others at APL that contributed to this work and my growth are Liz Abel, Elizabeth Heisler, Ted Hartka, Andy Driesman, Neal Bachtell, Erin LaBarre, Andy Lennon, Bruce Trethewey, Ryan Deacon, Craig Leese, Tony Ahan, Daniel Eby, and Kelles Gorges. At C-CAT and Plasma Processes, Aaron Brown, James Thompson, Erika Rensden, Johnny Menidola, Chris McKelvey and Daniel Butts were important friends and colleagues without whom this work would not have been possible. This work was done as part of the Parker Solar Probe program for NASA and I would be amiss to not thank them for their support.

I would also like to thank friends both at WSE and without for all their support throughout my graduate studies. There have been many additions to the Hemker group throughout my time and everyone has been supportive and encouraging. I am honored to be a part of such a wonderful group of people. Specifically, Dr. Justin Jones was an early collaborator on Solar Probe and Dr. Gianna Valentino came into the group later in my studies. Both provided great friendship and council. Outside of Hopkins, Simmie Berman, Shelby Martin, David Solomon, Patrick Sanders, Jennifer Glicoes, Kevin Fox, and Miranda Selover, thank you all for your unwavering support through this dissertation and your friendship. There are too many other people to name but all the friends and members of the Mechanical Engineering department that helped me through my studies and research were important.

Finally, I would like to thank my family for all their support and love. My parents, Lee and Kathy, my mother-in-law, Patti and my brother-in-law Deny, all supported and cheered for me throughout. To my husband, Billy Gallagher, I know that I started this Ph.D. before I met you, but it would not have been completed without you. Thank you for always believing in me, loving me and supporting my goals.

I dedicate this work to my parents. To my mother, Kathy Bissell who taught me that women can do anything and to always fight the good fight for what you believe in. To my father, Lee Congdon who gave me a curiosity about the world that has always taken me to great places.

TABLE OF CONTENTS

LIST OF TABLES

LIST OF FIGURES

CHAPTER 1. Introduction

Parker Solar Probe (PSP), a National Aeronautics and Space Administration (NASA) mission to study the corona of the Sun, launched in the summer of 2018. The PSP spacecraft has already travelled closer to the Sun than any human-made object and is planned to get within 10 solar radii in the next five years. This mission has been an aspiration of scientist and engineers since before the founding of NASA, but was not possible until recently because the materials required to protect the spacecraft from such a harsh environment were not available or well understood [1]. PSP, originally named Solar Probe Plus, was renamed in 2017 after Dr. Eugene Parker, the S. Chandrasekhar Distinguished Service Professor Emeritus, Department of Astronomy and Astrophysics at the University of Chicago. Dr. Parker theorized the existence of the solar wind in the 1950s and is the only living person to have a NASA spacecraft named after them [2].

As an enabling technology for the mission, a Thermal Protection System (TPS), or heat shield, was designed to sit between the Sun and the spacecraft during the majority of the mission, particularly during solar encounters, to manage the heat from the Sun. Resultantly, the spacecraft could be designed to operate at nominal temperatures using standard space rated components. As part of the development and fabrication of the PSP spacecraft, the TPS was designed, analyzed, built, and tested. This TPS development effort was successful, in part, due to a qualification and materials test plan that enabled the rapid maturation of a unique system that met all mission requirements. Due to the nature of this technology effort, the carbon foam which forms the core of the heat

shield, needed to be tested, analyzed and empirically understood. Carbon foam is delicate, as such, handling and testing was extremely difficult to accomplish in the environments of interest. As a result of these challenges, a unique qualification plan had to be generated and implemented. The foam was tested both structurally and thermally, on multiple scales to determine the behavior of the foam in the relevant environments. Post-test analysis involved distinguishing test artifacts from material behavior. This dissertation details the multiscale characterization of the carbon foam structurally and thermally that formed the linchpin of the PSP TPS development. This methodology enabled successful development of a structurally integral insulation system. As novel technology, these types of multifunctional thermal protection systems will benefit future missions such as Interstellar Probe, a NASA mission to study interstellar space, and the development of hypersonic thermal protection systems.

1.1. Motivation-Parker Solar Probe

NASA's PSP spacecraft was built by the Johns Hopkins University Applied Physics Laboratory (JHUAPL) from 2014-2018. Its mission is to study the energetic particles and magnetic fields that surround the Sun and investigate the origins of the solar wind by exploring within 10 solar radii of the Sun. Figure 1-1 depicts the PSP spacecraft and the location of the TPS on the PSP spacecraft. During most on-orbit operations, particularly solar encounters, the TPS remains pointed towards the Sun providing required thermal protection for the body of the spacecraft from the harsh solar environment.

A mission to probe the inner workings of the Sun was first imagined in 1958, when it was on the list of missions that the newly formed NASA should undertake, as

recommended by the Simpson committee [3]. In the decades that followed, eight major science and engineering studies were conducted on the feasibility of a mission that would travel inside of Mercury's orbit to study the Sun [1]. Throughout this time, due to the technological challenges of such an undertaking, these proposed missions never progressed beyond the concept phase. In 2008, a pair of reports, the 2008 Solar Probe Plus Science and Technology Definition Team Report and the Solar Probe Plus Mission Engineering Study Report, formulated a new concept that relied on an innovative mission design, solar power and a heat shield sandwich design [1]. The sandwich panel design was formed by having two facesheets bonded to a foam core. Like an aluminum honeycomb panel, a sandwich panel design functions as a low mass structural member, but unlike an aluminum honeycomb panel it is also designed to resist heat thermally. Ultimately this approach results in a lower mass design. With this new mission concept, the science objectives that had long been sought by the heliophysics community were within reach; however, significant engineering challenges remained. As noted by Fox, et al in 2015,

> *[PSP] will be exploring a region of space not yet explored – one potentially damaging to spacecraft and instruments. Surfaces of the spacecraft exposed to the Sun will experience about 475 Suns (649 kWm^{-2}), or 475 times the solar irradiance experienced at Earth (1366 Wm^{-2}) at [PSP's] minimum perihelion. The high irradiance requires development and implementation of a thermal shield to enable the majority of the spacecraft systems and instruments to operate in a typical space thermal environment, and drives the thermal environment of the solar array and the solar exposed instruments [1].*

All of these extreme environments – the temperature, the plasma, the energetic particles and the dust – needed to be accounted for in the design of the spacecraft.

Designing for these extreme environments was even more challenging given no spacecraft had been to the region before and these environmental elements lacked in situ characterization, the primary objective of PSP. This dissertation focuses on the work that was done to test the materials used to develop a TPS that enabled PSP.

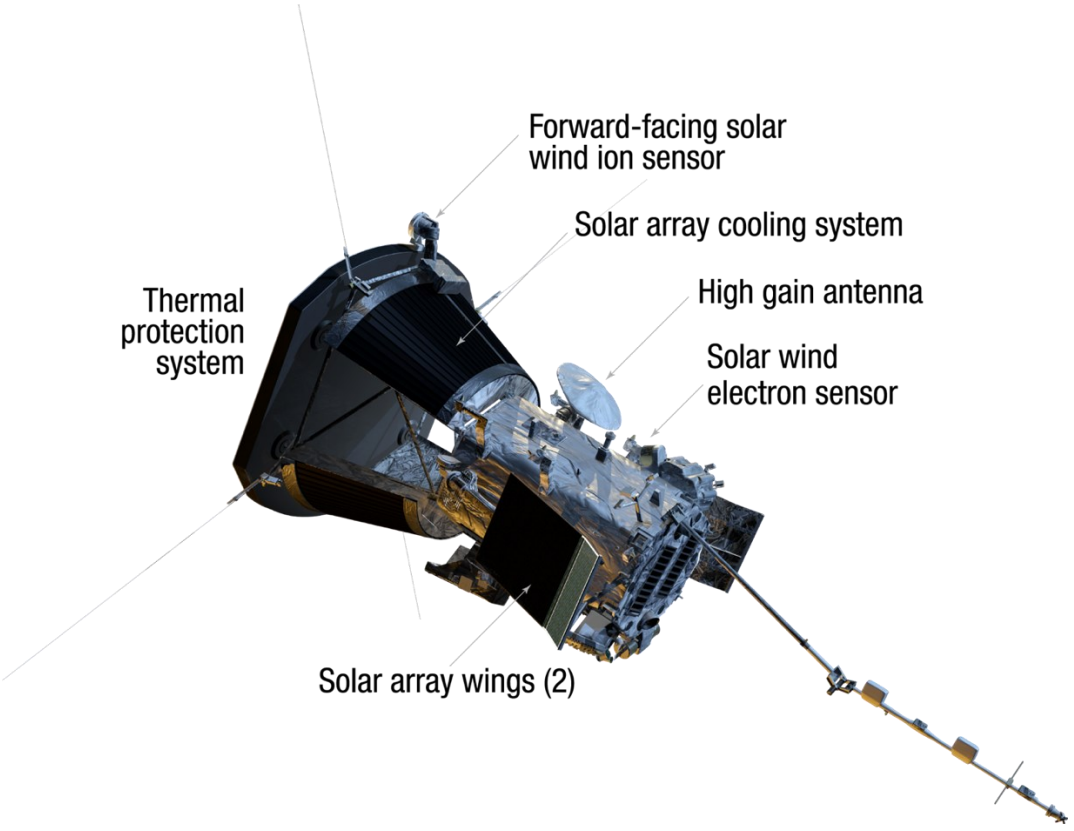

Figure 1-1 The spacecraft layout for Parker Solar Probe. The approximately 2.4-meter diameter Thermal Protection System (TPS) is on the far left of the picture. The FIELDS antennas and the forward-facing solar wind ion sensor (part of the SWEAP suite) peak out into the solar environment. The rest of the spacecraft, including the solar arrays, the high gain and the rest of the instruments remain in the shadow, or umbra, of the TPS [3].

PSP is groundbreaking within the discipline of heliophysics. As Thomas Zurbuchen, the Associate Administrator for Science at NASA, stated:

> *"Observing the Sun up close rather than from a much greater distance is giving us an unprecedented view into important solar phenomena and how they affect us on Earth, and give us new insights relevant to the understanding of active stars*

across galaxies. It's just the beginning of an incredibly exciting time for heliophysics with Parker at the vanguard of new discoveries," [4].

The scientific drive to undertake a mission to the Sun is the unknown physical phenomena exhibited by our star. PSP seeks to answer many mysteries about the Sun, including the origins of the solar wind and why the Sun's corona is hotter than its surface. The presence of highly ionized heavy metals, such as Fe^{14+} and Fe^{13+}, in the low corona region was discovered in the 1930s indicating that this area is several million degrees Celsius. Since then, it has been a mystery as to why the photosphere, the Sun's visible surface, which sits at 5800°C, is so much cooler [5]. PSP is designed and built to unravel these scientific questions by allowing us to study the energy that heats and accelerates the solar wind, the plasma and magnetic field dynamics at the source of the solar wind and the mechanisms that transport and accelerate the energetic particles that form the basis of the solar wind [2]. These investigations are critical to understanding the space weather that impacts Earth and causes disruptions in satellites and communication technology. As humans seek to further explore the universe, understanding the Sun will be critical in protecting astronauts from exposure to dangerous solar events while on extended deep-space missions throughout the solar system. Since this expanse of space around the Sun is previously unexplored there is a potential for even greater discoveries. As Dr. Parker notes, "as PSP explores a region of space never transversed before, the potential for unforeseen discoveries beyond these science objectives is huge," [5].

In order to meet these science objectives, PSP is designed to support four instrument suites that are investigating the Sun: the Electromagnetic Fields Investigation

(FIELDS), the Integrated Science Investigation of the Sun (ISʘIS), the Solar Wind Electrons Alphas and Protons Investigation (SWEAP) and the Wide Field Imager for Solar Probe (WISPR). FIELDS, led by the University of California at Berkeley, consists of electric fields antennas which measure electric and magnetic fields and waves and a set of fluxgate and search coil magnetometers. SWEAP, led by the Smithsonian Astrophysical Observatory, is a suite composed of a Faraday cup and two electrostatic analyzers and it measures the particles in the solar wind –protons, electrons and helium ions. WISPR, led by the Naval Research Laboratory, is a white light imager which provides images of the solar wind. Finally, ISʘIS is an instrument suite that studies high energy protons, electrons and heavy ions [1]. These instruments are the core of the PSP spacecraft and are designed to study the Sun from within the corona.

From the Earth, over ninety million miles away from the Sun, the solar wind seems relatively uniform with only occasional turmoil, but this perspective of the solar wind has been formulated from the observations of near-Earth spacecraft. PSP is now closer to the source of the solar wind than any previous mission. From this vantage point, the Sun is dynamic and complicated revealing structures and delicacies never before seen [4]. Just two years into the mission, the science returned has already been extraordinary. During the first two orbits of PSP, the spacecraft was effectively corotational with the Sun meaning that it was hovering over the same area of solar surface throughout the pass. Additionally, the Sun was at a solar minimum, the less active part of the solar cycle, when these first passes were made. As the probe gets further into its mission, the Sun will be moving towards solar maximum. Even at solar

minimum, there has been great science from the first two passes. As Parker notes in his overview article in *Nature*, "the physical picture that is developing is markedly different from that engendered in past decades based on data from other missions located farther from the Sun, where only low-amplitude fluctuations were routinely recorded," [5].

As an example of the science already discovered, WISPR, the white light imager on PSP, is showing the environment around the Sun in stunning pictures. Figure 1-2 is a combined image that has been adapted from images taken by WISPR. WISPR is optically baffled by the TPS, meaning the TPS is blocking the intense part of the Sun, so that it can image the fine structures emanating from the star. Figure 1-2 shows an image of the visible structures coming off the Sun. An empirical model of the F-corona, the dust or zodiacal light, has been removed from the image to highlight the other visible objects. These images feature our galaxy in the middle of the frame. To the left, a streamer from the Sun can be seen bursting from the edge. The white dot path outlines the path of the asteroid 3200 Phaethon and Jupiter is the bright spot farthest to the right. Images like these from WISPR are reshaping our view of the Sun and illuminating the Sun's fine structures that we have never seen before. As the probe gets closer to the Sun, the hope is that WISPR will observe the theoretically-predicted dust free zone around the Sun that has never been observed before since there has never been a view from so close to the Sun [6].

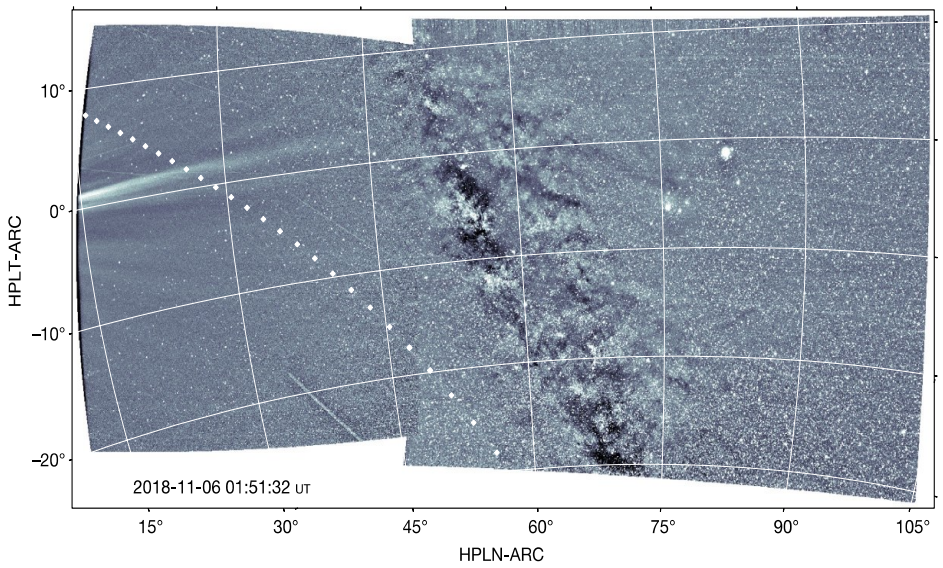

Figure 1-2 Image from WISPR from which an empirical model of the F-corona has been removed from 6 November 2018 at 01:44 UT. The image shows the dust trail of asteroid 3200 Phaethon which is traced by the white dots. Also present is a streamer on the left which appears to be coming from the Sun and outlines the heliospheric current. The middle of the image is the Galaxy and the bright object in the upper right is Jupiter [6]

In addition to the images from WISPR, the particle and fields instruments have also been studying the Sun from up close. Another major finding based on the data from the first two passes of PSP is the presence of S-bends in the magnetic field that have been dubbed *switchbacks*. These unexpected phenomena could explain how stars lose angular momentum throughout their lifetime. Figure 1-3 summarizes the particle and fields data from the instrument sensors on PSP during encounter 1 at a distance of 35.7 solar radii from the Sun. The grey area in the picture is the area of interest with the transition in and out of this region shown in light blue. As shown in the figure, the proton velocity, V_p, peaks (graph a, blue line) while the angle of the magnetic field relative to the outwards radial direction from the Sun, θ_B, changes direction (graph a, red line) and the proton density, n_p, drops (graph b, green line).

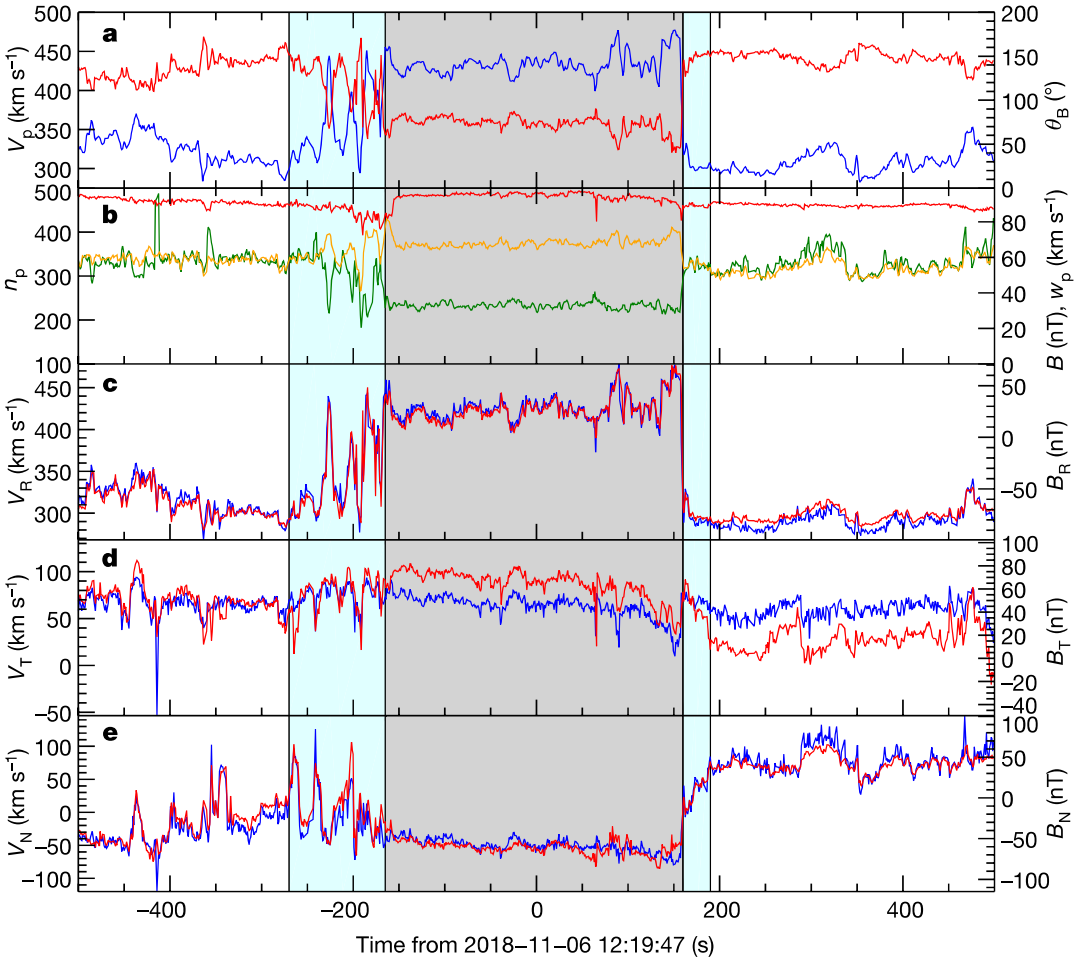

Figure 1-3 The bulk properties of the solar wind protons during a peak which was seen during encounter 1 at a distance of 35.7 solar radii. The grey shaded area is the occurrence of one of these peaks with the light blue shaded areas the transition from the normal activity to the peak. Note the volatility in the transition region compared to the consistent data in the white and grey shaded areas. Graph a compares the V_p, the proton velocity (blue), to the angle of the magnetic field relative to the radial outwards from the Sun direction, θ_B (red). V_p peaks upwards as θ_B settles downwards indicting the presence of the peak. In graph b, n_p, the proton density (green), B, the magnetic field (red), and w_p, the thermal proton speed (yellow), are compared. The proton density drops during one of these peaks. The bottom three graphs break out the radial, transverse and normal components of the magnetic field and proton velocity [7].

Figure 1-4 shows a diagram of the magnetic field switchbacks that is suggested by the data in Figure 1-3. The left graphic represents the observations of the spacecraft of velocity, electron strahl (the electron component of the solar wind) and magnetic

field of the Sun. The black square represents the spacecraft as it is flying through the pink lines that represent the magnetic field with the arrows pointing back at the Sun [7]. The right graphic is an artistic representation of these switchbacks. The Sun, field lines and spacecraft are not to scale [8]. The cause and complete picture of these unexpected switchbacks are still unknown but as PSP dives in closer to the Sun, scientists expect that more data will provide a deeper understanding of our star and all stars in the universe [7]. Data from Parker Solar Probe has revealed unexpected results by studying the Sun in situ but there is still more to investigate as PSP gets closer on future orbits.

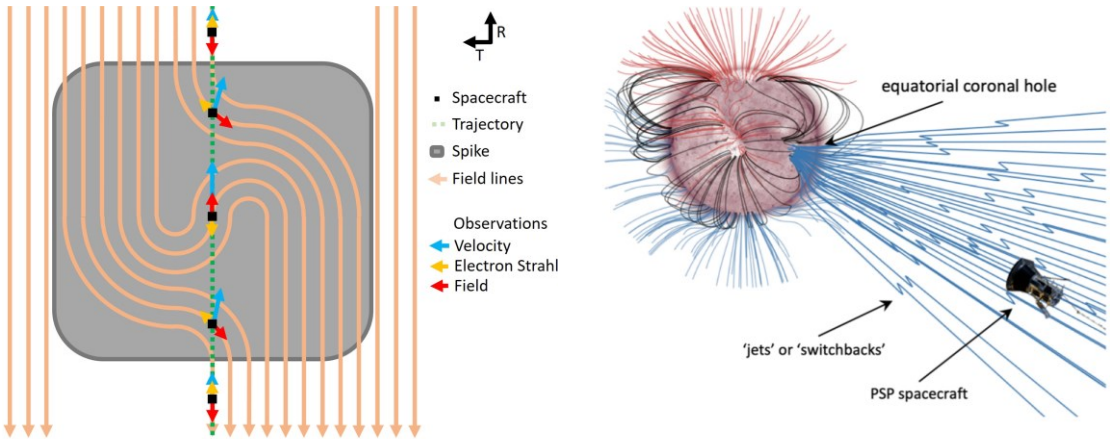

Figure 1-4 A graphical representation of the switchbacks. One the left, a figure describing the velocity, electron strahl, and field vectors on the magnetic field lines [7]. On the right, an artistic representation of the switchbacks, note the Sun, magnetic field lines and PSP spacecraft are not to scale [8].

The science discovered to date is possible due to the engineering behind the spacecraft. The mission concept that was executed and now exists as Parker Solar Probe relies on a unique mission architecture, which drove many of the requirements for the

TPS. Using a unique mission trajectory, the spacecraft repeatedly uses Venus as a gravity assist body to get closer to the Sun throughout the life of the mission. The PSP mission design is for the spacecraft to complete 24 orbits of the Sun over the course of 7 years. Figure 1-5 is a graphic of the mission profile showing passes made, as of September 2020, in green.

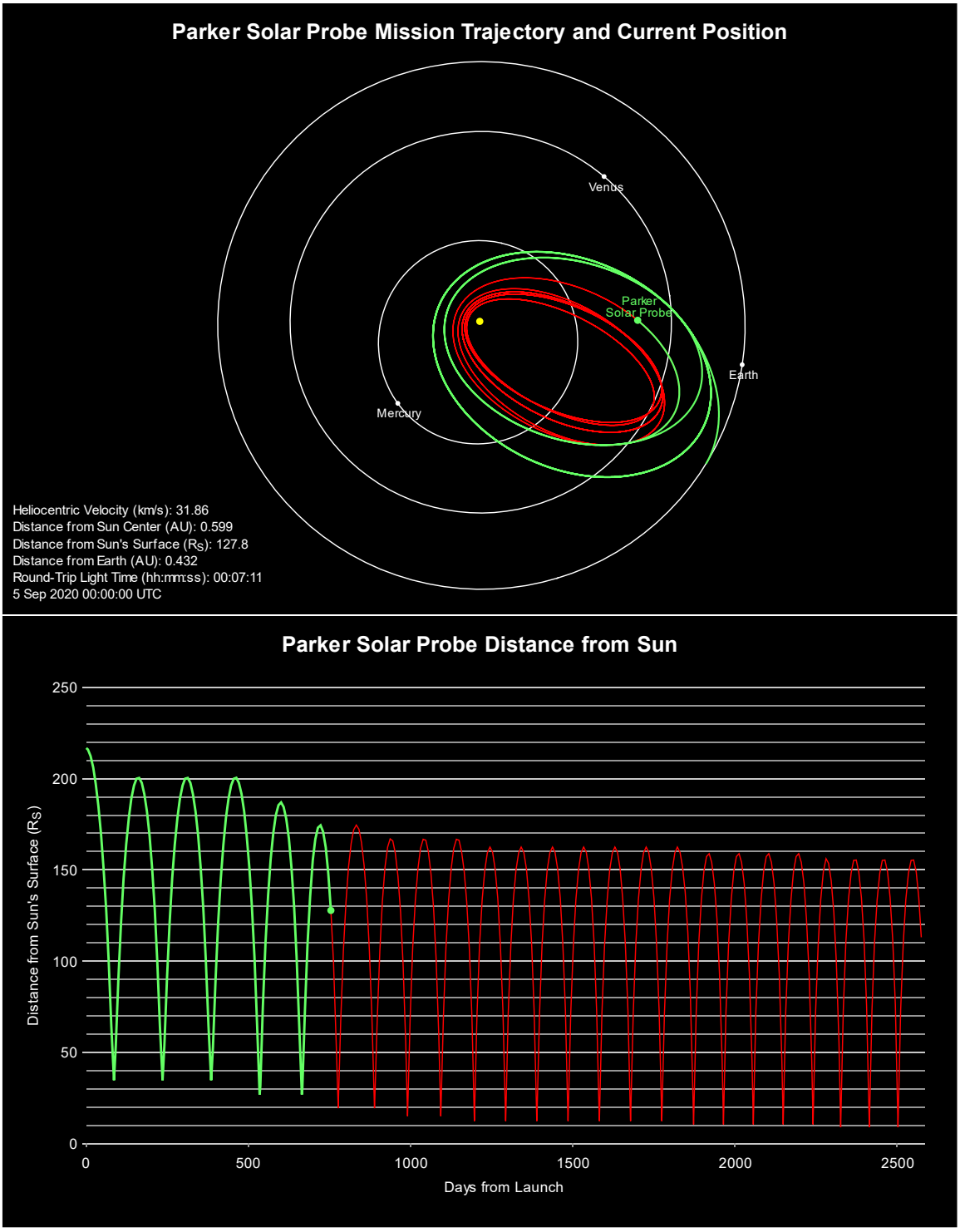

Figure 1-5 Mission design profile as of September 4, 2020. The green lines indicate where PSP has traveled in the top chart shown in orbits and the bottom graph showing distance from the Sun. As the mission progresses, Venus is used as a gravity assist body for PSP to get closer and closer to the Sun. Despite being on the farther orbits, PSP has already broken the record for the closest man made object to the Sun [3]

As shown in Figure 1-5, there are several sets of encounters at the same distance punctuated by Venus being used as a gravity assist body to get the spacecraft closer to the Sun over the seven-year mission. This design has scientific benefits over previously proposed versions of a mission to the Sun in that there are many more orbits and there are repeated orbits for scientific comparison [1]. This mission design had important implications for the design of the spacecraft and by extension the TPS. First, it means that the harshest environmental passes are at the end of the seven-year mission. Additionally, the Sun-to-Venus oblong orbits mean that the TPS is experiencing cyclical thermal loading going from, at the extremes, -100°C to 1300°C throughout the seven-year mission. Ultimately, the science objectives and the mission design were the driving factors for the overall design of the spacecraft and the TPS. These temperatures drove the materials development plan.

Another factor that influenced the development of the TPS was the spatial requirements driven by the design of the spacecraft. Figure 1-1 presents the layout of the PSP Spacecraft with components identified. The left-hand side of the figure is the TPS. Behind the TPS is a truss structure that holds on the solar array cooling system radiators and attaches the TPS to the rest of the spacecraft. Figure 1-6 shows the connection between the multifunctional TPS and the truss structure that connects it with the rest of the spacecraft. The PSP spacecraft is solar powered, and solar arrays are less efficient when they are hot. Therefore, the spacecraft has a water filled liquid cooling system to allow the solar arrays to perform at closest approach. This solar array

cooling system has radiators mounted to the truss structure between the TPS and the spacecraft so that the flowing water can be cooled by viewing deep space before streaming back into the solar arrays. Below the solar array cooling system in Figure 1-1 is the spacecraft bus. Most of the electronics, communication equipment and instruments are located on this part of the system. The components that are closest to the edge of the shadow of the TPS are the solar limb sensors. These sensors are used by the autonomy system to keep the TPS sun pointing during solar encounters. The figure also shows the high gain antenna used to communicate with Earth and the solar arrays which articulate to keep them protected from the Sun during the mission. Also shown in the figure are two of the four instrument suites on the spacecraft, the forward-facing solar wind ion sensor and the solar wind electron sensor located on the spacecraft bus. As shown in the figure, the TPS is "sized to nearly eliminate the heat flow to the spacecraft and instruments from the 475 Suns environment closest approach, enabling the majority of [PSP] components and instruments to operate in a near standard spacecraft thermal environment," [1]. An important part of this particular type of technology development is to understand that the technology being developed is part of a spacecraft system and therefore all the materials need to be understood and selected within the context of the larger system.

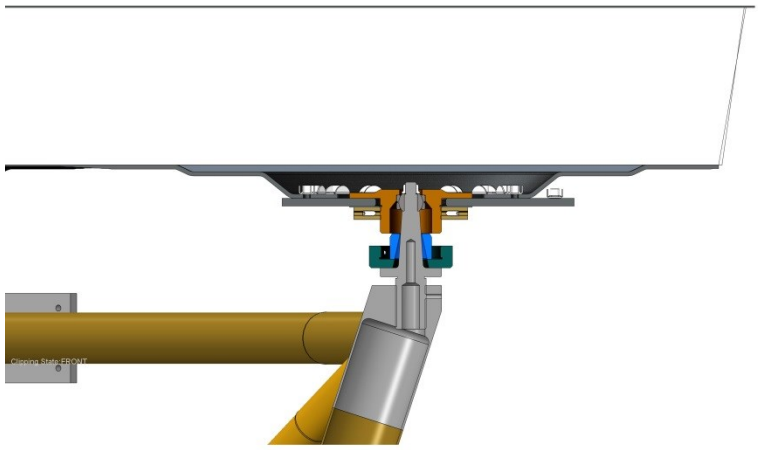

Figure 1-6 Computer Aided Design (CAD) picture of the connection between the TPS and the truss structure which connects it to the rest of the spacecraft at six discrete points

The TPS is a critical part of this spacecraft system that is a non-ablative, lightweight sandwich panel that thermally protects the rest of the spacecraft. It is composed of a composite sandwich panel made of two thin facesheets of carbon-carbon composite with a core of carbon foam. The sun-facing facesheet is coated with a plasma-sprayed white coating that is specially designed for the application. The heat shield is approximately 2.4 meters in diameter and weighs 73 kg. The TPS shape is driven by the requirement to keep the spacecraft bus, key elements of which are described in the previous paragraph, in the shadow of the shield during solar encounters; it has long straight edges that are used to precisely shadow the solar arrays while they are articulated. The TPS also has shorter flat areas that are used by the solar limb sensors on the spacecraft bus to autonomously maintain a TPS-to-Sun pointing angle during every pass around the Sun. The TPS must limit the heat into the solar array

cooling system and spacecraft bus, which drives the thermal design requirements on its design.

Since the beginnings of a formulation of a mission to the Sun, technology development efforts for the heat shield were performed. Table 1 outlines the recent and specific technology development effort that led to the development of the heat shield that launched on PSP. As noted at the beginning of this chapter, the formulation of a mission to the Sun which relied on solar power was first published in the 2008 Solar Probe Plus Mission Engineering Study. This report envisaged a flat sandwich panel, a design that framed the research in this dissertation.

Table 1: PSP TPS development

	Years
Solar Probe: An Engineering Study	2002
Solar Probe: Report of the Science and Technology Definition Team	2005
Solar Probe Thermal Protection System Risk Mitigation Study	2006
Solar Probe Plus Mission Engineering Study Report	2008
TPS Risk Mitigation Funding and Development	2008-2013
Solar Probe Mission Preliminary Design Review	2014
TPS Verification Plan Execution	2014-2018
TPS Flight and Flight Spare Delivery	2017
TPS Flight and Flight Spare Testing	2017-2018

As shown in the table, the technology development of the TPS went from a paper study to a full-scale tested unit in approximately 5 years (TPS Risk Mitigation Funding and Development). This technology development effort, led by JHUAPL, required an in-depth understanding of the materials, system and design constraints that led to the development of the multifunctional full-scale unit. The design constraints that

drove the overall TPS design were limited mass, extreme temperature thermal cycling and survival of launch loads.

The mission design drove the mass limitations on the TPS. A large amount of energy was needed to get the spacecraft into the proper orbit around the Sun. PSP launched on a Delta IV-Heavy rocket, the most powerful rocket available at the time of launch, but mass was very limited in order to meet mission requirements. As noted, the TPS is separated from the spacecraft by a titanium truss that also holds the solar array's radiators. The titanium truss acts to connect the TPS to the rest of the spacecraft while minimizing heat flow. The six discrete points of attachment to the truss, as shown in Figure 1-6, mean that the TPS sandwich structure needs to survive launch loading as a system without additional structural support. The design of the PSP TPS is known as structurally integral insulation because the thermal materials in the system also need to take structural loading. This methodology is a change from thermal protection systems on the Space Shuttle and other reentry vehicles, which are designed such that the thermal protection systems are supported on metallic frames which take the structural loading. The structurally integral insulation approach was a break from traditional thermal protection systems and was pursued for use on the PSP mission due to the mass constraints. A history of thermal protection system development more broadly is discussed in Chapter 2. A sandwich panel is a structurally robust lightweight material system that is often found in aircraft and spacecraft in the form of aluminum or composite honeycomb. The PSP mission would not exist without the development of the TPS as a high temperature sandwich panel.

Using this innovative sandwich panel approach meant that the materials needed to be investigated and tested in ways different than for traditional thermal protection systems. The critical component of the PSP TPS was its carbon foam as it served as the structural core of the sandwich panel as well as the main insulation. Studies throughout the development of the heat shield focused on understanding the behavior of this foam. Thermal and structural testing was done at multiple scales to characterize and understand the in-flight behavior. This dissertation focuses on the methodology used to characterize the carbon foam; thermal and structural testing of this foam at multiple scales is discussed and analyzed.

The carbon foam materials testing approach that is examined in this dissertation is part of a larger engineering effort that successfully launched on the PSP spacecraft. This approach can be used to design future high temperature systems, such as thermal protection systems for hypersonic vehicles and the heat shield for Interstellar Probe. The development of this system required an understanding of the material components, the manufacturing methods and the behavior of the system of materials. The PSP TPS was taken from a paper drawing to the first full scale article in five years. To accomplish this task, a qualification process was established for the rapid development of high temperature systems. It is expensive and difficult to test the TPS materials fully at the temperatures and vacuum conditions that will be present in the flight environment. Further, there is sufficient uncertainty in the temperatures and dust environment that comprehensively testing all the possibilities is prohibitive at the coupon scale, subsystem scale and full scale. Additionally, while coupons are easier to test, they are

not always representative of the full system. The challenge was therefore to understand the behavior of the material at multiple scales and in a variety of conditions as is practical.

Figure 1-7 shows the TPS fully integrated on the spacecraft a few weeks before launch in August 2018. The successful development of the PSP TPS was dependent on careful integration of material testing and development coinciding with large system level engineering development [9]. The PSP TPS provides a road map for how to design, develop and test these types of systems in the future, which will be key to enabling future NASA missions, as well as hypersonic thermal protection systems.

Figure 1-7 TPS fully integrated on PSP, photo credit: Ed Whitman (JHU/APL)

1.2. Overview of Dissertation

The focus of this dissertation is on the multiscale characterization of carbon foam, which is the primary core and insulation of the PSP TPS. The carbon foam makes up the core of the sandwich panel for the PSP TPS and needed to be fully understood in order to achieve mission success. The carbon foam was investigated not only on the coupon level scale but in the full-scale application that is the PSP TPS. The thermal and structural material properties of the foam needed to be validated at multiple scales in terrestrial testing so that the extrapolated behavior of the full-scale system when at the Sun could be determined. Chapter 2 provides the background of the traditional approaches to determining properties of foams and the traditional methodologies for thermal protection systems for spacecraft. The chapter includes a literature review on low-density carbon foams. It also outlines the foams of interest and describes the carbon foam manufacturing process.

Chapter 3 focuses on the techniques for thermal property determination and the results from these assessments. The chapter highlights two of the testing types that were performed for thermal properties. The first set employed traditional test standards for determining the properties of effective thermal conductivity. As described in the chapter, there are limitations to these types of tests. Additional testing performed was at the subscale level. There are also limitations to this subscale testing which is elaborated on in this chapter. Despite not being able to test a full-scale unit in the

proper environment before launch, the full-scale TPS thermal performance at the Sun is predictable based on the multi-scale testing program.

Chapter 4 outlines structural property testing and results at multiple scales. Much like the thermal property testing, the structural testing needed to be understood on multiple scales in order to determine the material response of the PSP TPS at launch. In this chapter, coupon level testing and the results of three-point bend subscale testing are outlined. The limitations of each test and how these tests are used to ultimately understand the behavior of the carbon foam at scale is highlighted.

Finally, in chapter 5, the interpretation of the test data across multiple scales is commented on. The similarities between the thermal and structural testing and what can be inferred about the carbon foam of interest is discussed. The TPS design effort is summarized and future applications for these types of multifunctional systems are discussed.

CHAPTER 2. Background

The historical approach for designing thermal protection systems separated the design tasks into thermal and structural components. Within the thermal design approach, thermal loading was addressed by using insulation to reduce the temperature to appropriate levels for the structural components that were shielded by the thermal insulation. The subsequent structural design approach resulted in this thermal insulation being bonded to a structural frame that was ultimately responsible for absorbing the structural loading. This bifurcated design was and continues to be employed throughout the history of aerospace design and spaceflight. Examples of this heritage approach within NASA include the Space Shuttle, the Apollo capsules and the new Orion capsules. While this historical approach is prevalent and technically sound, it is extremely inefficient from the perspective of both mass and its associated margin.

While thermal materials tend to be less robust to applied loads than structural materials, the system as a whole will be lighter if all materials can be relied upon to take both structural and thermal loading. From a design perspective, there is engineering conservativism that increases the mass of the whole system. Thermal protection technology for aerospace applications has long been limited by the bondline temperature between the thermal insulation and the structural frame that is supporting it. This bond material is structural and therefore must be kept below temperatures for structural adhesives. Traditional bond materials, usually RTV (room-temperature vulcanizing) silicone, have needed to be kept below 200°C. Since a temperature violation

at the bondline would result in catastrophic failure, extra insulation is added to ensure colder bondline temperatures leading to an increase in mass of the overall system.

The total mass for Parker Solar Probe at launch was 685 kg [2] and this constraint drove mass limitations on all the subsystems. Therefore, the thermal insulation needed to be designed to take both thermal and structural loading as part of a sandwich panel. This new combined load design approach drastically reduced the mass necessary for the overall TPS system. But, doing so meant the carbon foam insulation structural and thermal properties needed to be more thoroughly understood than was necessary for previous designs. This innovative multifunctional approach is known as structurally integral insulation and the PSP TPS was the first ever mission to implement this design methodology.

2.1. Overview of Historical Thermal Protection Systems

Historically, TPS designs were matched to the environments that they need to perform in. Models of these materials typically had high uncertainty factors; therefore, the testing program also needed to match the TPS environment. As such, there have been many forms and variations on TPS design approaches. Two specific design approaches include ablative and reusable. Ablative examples include the Apollo capsule, Mars landers and the new Orion mission. The most famous reusable example is the Space Shuttle.

2.1.1. Overview of Ablative Systems

Most historical TPS have been ablative systems utilizing tiles or separate pieces to minimize structural loading. As Venkatapathy, et al., explains, ablation is a complex thermal management approach:

> *Ablative TPS materials involve many complex physical and chemical processes, but their basic principle is energy management through material consumption…a typical ablative composite contains an organic resin that pyrolyzes when heated, producing gaseous products and a condensed phase carbonaceous residue called char. The gases percolate through the porous char to the heated surface, providing some convective cooling of the hot near-surface material. The gases are injected into the adjacent boundary layer at the surface, providing some transpiration cooling. Dependent upon the chemical composition of the char and the boundary layer, the surface char can be consumed through chemical reactions with the boundary layer gases. A carbonaceous surface char is advantageous, as it allows very high surface temperatures. For such materials, surface re-radiation is the major energy accommodation mechanism, [10].*

For these ablative systems, the thermal protection components are tiled onto a structural frame. In this configuration, thermal tiles only need to support themselves and are subjected to minimal structural loads. For example, Mars missions prior to Mars Science Laboratory (MSL), which launched in November 2011, used SLA-561V as a thermal isolation material, which was first used on the 1976 Viking Lander. More recently, Phenolic-Impregnated Carbon Ablator (PICA), a material developed at NASA Ames Research Center in the 1990s, was used on Stardust and further developed for MSL. On Stardust PICA was used as a continuous shield TPS, meaning it was made all in

one piece, but due to size constraints and thermal expansion concerns, MSL had to use tiles on the heat shield. Having a fibrous carbon base infused with phenolic resin, PICA was designed to be an ablative system and is still in use on systems today.

A tiled PICA TPS design is limited by the structural bond adhering the thermal tile material to the frame and the adhesives used at the bondline between the structural frame and the thermal material are generally only capable of structural loading at $T < 200°C$. To further complicate matters, there are often thermal expansion concerns at this critical interface. To minimize this effect, for the Orion Crew Exploration Vehicle (CEV) PICA is used with a strain isolation pad (SIP) under the PICA tiles which allows the TPS to be attached to a metallic frame. For MSL, the frame was composite thereby eliminating the need for a SIP [11]. Figure 2-1 shows the edge engineering model for the MSL heat shield.

Figure 2-1 Mars Science Laboratory Edge Engineering Model, the edge is tiled with multiple blocks of PICA of different shapes and sizes [11]

2.1.2. Overview of Reusable Systems

An emerging class of heat shields are reusable systems. These systems are designed to be non-ablative so that they do not need to be replaced with each use. While orbiting the Sun, the PSP TPS must survive multiple thermal cycles to achieve its mission objectives. The PSP TPS differs from legacy reusable systems in that it is load bearing. Despite being non-ablative, the legacy reusable heat shields are still based on similar principals in that the thermal system is taken out of the primary load path and is instead bonded onto the structure. The most famous and recognizable example of that type of system is the Space Shuttle.

While not an exact analogy, the reusable factor of the Space Shuttle TPS design means that it is a worthy comparison for the many years of use the PSP TPS will see during its twenty-four orbits around the Sun. The design of Shuttle tiles relied on engineering principles to move away from an ablative shield towards one that was designed to take multiple thermal excursions without degradation. However, similar to previous heat shields, the Space Shuttle relied on a tiled structure. Figure 2-2 depicts a Shuttle tile layout. The picture shows multiple blocks of different sizes that were required to accommodate the geometry of the Space Shuttle. The design of the tiles on the Space Shuttle, also referred to as the Orbiter, used some black and some white tiles to accommodate different heating profiles. The black and white tiles were made of different materials, carbon-carbon and silica respectively. The white tiles were used in areas on the Orbiter that were exposed to the Sun during maneuvers or operations; the black tiles were placed on the higher heat surfaces like those exposed to the heat of reentry [12].

Like the ablative TPS, there were gaps between the tiles and a SIP to accommodate thermal expansion. The SIP was made of a felt-like material and allowed for thermal growth differences between the metallic structure and the thermal tile. The body of the Space Shuttle was an aluminum structure that had been primed with Koropon to allow for the bonding of the silicone RTV adhesive [13]. The tiles themselves were mostly made of silica fibers whose thickness was designed to keep the Shuttle's primary aluminum load skin below 177°C [12]. Keeping the bondline between the structural skin and the thermal tiles at a temperature below the operational temperature of the

adhesive was a driver in the design of the Space Shuttle. The coefficient of expansion and the thermal capability of the adhesive drove the overall system design. By moving away from a tile-based system, the PSP TPS no longer relied on defining the system around this temperature. Due to the sandwich panel design of the PSP TPS, the bondline on the front and backside of the sandwich were designed to operate at the same temperature which was 1300°C .

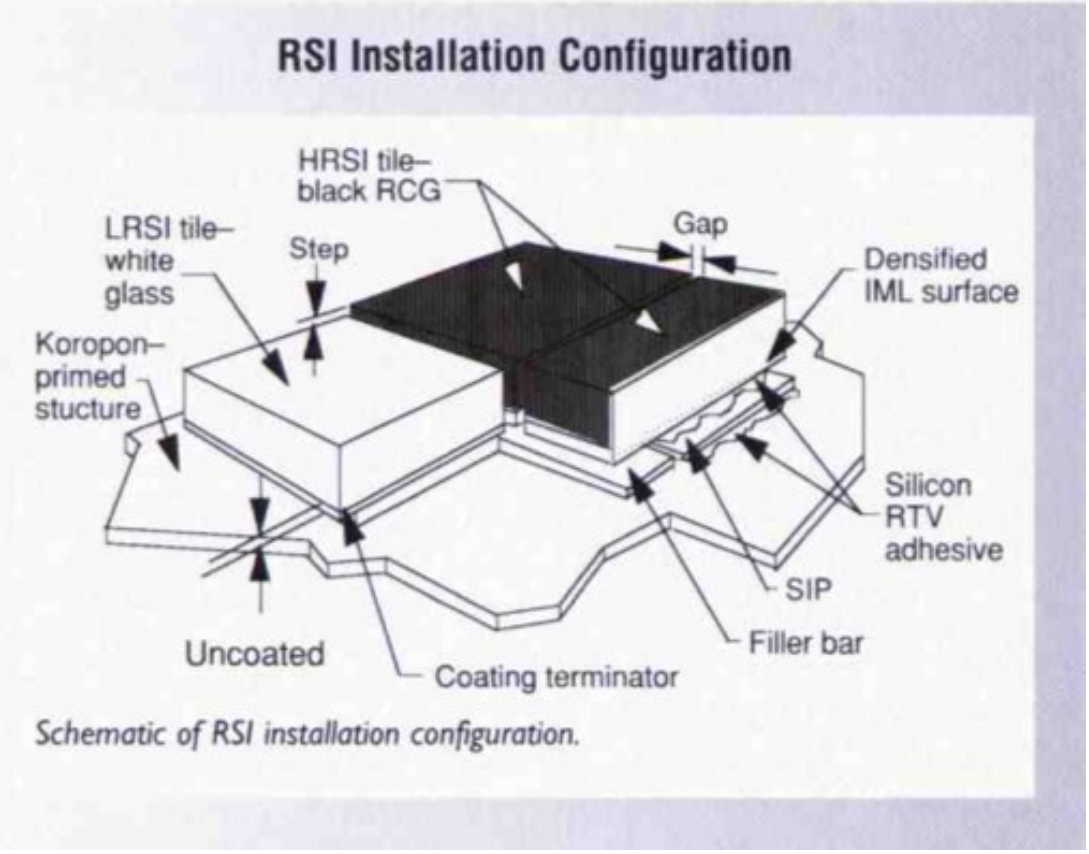

Figure 2-2 Shuttle tile schematic which pictures the complex system that was developed for the Space Shuttle heat shield. There were different tile types of various sizes which were held on to the aluminum structure via a SIP pad and an RTV adhesive [13]

The Space Shuttle's complex system of bonds and tiles was similar to the historical ablative TPS, and the development of such a complicated heat shield

significantly contributed to a three-year delay at the start of the Shuttle program. The Shuttle had over 24,000 tiles covering its surface, with the largest being 10 inches by 11 inches, though the average was about 6 inches by 6 inches [12]. Despite being designed to be reusable, all tiles has to be inspected and on average 30 to 100 tiles had to be replaced per mission, [12].

2.1.3. Impact of Historical TPS Approaches on the PSP TPS

While the PSP TPS was designed to simplify and revolutionize the approach to thermal protection, some of the same difficulties with design and testing remained. It is impossible to fully test and analyze these systems on Earth, makes it extremely difficult to adapt them to new applications. The inability to test in the applicable environment is colloquially referred to in engineering as a violation of the principle of *test as you fly, fly as you test*. When testing cannot be performed at the full scale, material and subscale testing is traditionally used to predict the performance of the TPS. These smaller tests can be difficult to scale to full-scale performance. As Venkatapathy, et al., noted in their article about the future of TPS systems, “a critical issue in designing an ablative TPS is the requirement to understand failure mechanisms [10]. Unfortunately, experiments to define failure thresholds and identify failure mechanisms are rarely performed. Consequently, defining a TPS design ‘margin’ has been, in reality, quite arbitrary,” [10]. Difficulty in understanding the limits of designs can have drastic consequences. Launched in 2011, the MSL spacecraft TPS was originally designed with the traditional materials that had been used since the Viking lander. However, the MSL spacecraft was larger and the entry speed was different. The inconsistency in the performance of the

original shield design was not discovered until well into materials testing. After a catastrophic failure of the planned TPS material during qualification testing, the MSL team moved to a tiled heat shield using an experimental material, PICA. As the authors noted in an article on lessons learned during the design process, “one of the central tenets of TPS design is that the material must be robust with respect to the environment in which it will be placed and, largely because accurate modeling and precise environment qualification is nearly impossible, the material system must not exhibit any catastrophic, unexplained behaviors in relevant environments,” [11]. A historical review of TPS designs concluded that these systems must be tested outside of the normal *test as you fly* engineering approach. To test a new TPS design, like that developed for PSP, coupons, subscale and full-scale testing needed to be used in concert to understand the full system behavior.

Given the difficulty of testing in the relevant environments and the limitations of the analytical tools available, it was not surprising when models and test results do not match. As Szalai, et al., noted, modeling at the joints between the PICA tiles showed there should be failure in the relevant environments [11]. However, tests consistently proved this prediction wrong. As Szalai et al. note, “the team was faced with the choice of developing complex analyses and failure criteria to describe the gap regions of the design or developing an empirical test program to demonstrate margined structural and thermal performance of the design. The team chose the latter route and relied on analytical margins for the acreage areas of PICA tiles and on experimentally determined margins for the gap region of the system,” [11].

Due to the mass limitations and unique environmental profile of PSP, we set out to develop a radically new TPS. This new approach has the same limitations as previous TPS in that testing on Earth is limited and unique design considerations must be understood. However, despite these limitations, the PSP TPS serves as a model for future TPS systems and could revolutionize heat shield technology.

2.2. Overview of Carbon Foams Under Study

Being able to use carbon foam as a structurally-integral insulation in the TPS made PSP possible. Carbon foam can act both as a thermal insulator and a structural member in high temperature sandwich systems, but the structural and thermal properties must be established in order to optimize performance and assure reliability. A survey of the carbon foam landscape was undertaken to understand how the chemical composition, manufacturing process, structure and density could affect these properties.

Table 2 is an overview of the carbon foams that were studied. These carbon foams were chosen because they were commercially available and able to be manufactured at scale at the time of the study. These factors were important because of the short timeline required for the development of the PSP TPS. The system had to be developed in five years and included advancement work in bond material, in facesheet material, in manufacturing processes at scale, in qualification test program approaches, in materials test programs for all components, in coating development and in coating manufacturing processes. Therefore, the foam selected needed to be scalable and manufacturable from the beginning of the study so systems level progress work could happen concurrently on all these other development items that led to a successful TPS.

Table 2: Survey of carbon foams that were used for this study

Carbon Foam	Relative Density	Cell Type	Manufacturer
Ultramet 100 ppi 3%	3%	Open	Ultramet
ERG 100 ppi 3% Duocel®	3%	Open	ERG Aerospace
Calcarb®	10%	Fibrous	Mersen
GraFoam FPA-02	2%	Mixed (Open/Closed)	GrafTech
GraFoam FPA-05	5%	Mixed (Open/Closed)	GrafTech
GraFoam FPA-10	10%	Mixed (Open/Closed)	GrafTech

All of the foams studied in this dissertation and considered for PSP are low density carbon foams with relative densities of less than 10%. Relative density is the actual mass of the foam divided by the hypothetical mass of a solid block of that material. In practice, this gives an idea of the open volume versus solid volume in the foam. Foams of the same relative density can have different structures. For example, there are open celled, closed celled and mixed open and closed cell foams. Open celled foams are not closed off on the sides and are completely permeable. Closed celled foams can trap air or other gases inside individual cells. Mixed open and closed cell foams are a mix of open and closed cells. For aerospace applications, closed celled foams are not practical due to the change in pressure during ascent from Earth into space. The trapped air is unable to expand, causing an increase in pressure and a

potential explosion that would result in the destruction of the sandwich panel and loss of the mission.

Carbon foam, in its most basic form, is made by impregnating a shape of interest with phenolic resin and then pyrolyzing that material. Each foam type is produced with a specialized and usually patented process, but the approaches are similar. For example, the Ultramet 100 pores per inch (ppi) 3% foam studied here is based on a polyurethane foam that is impregnated with phenolic resin and then pyrolyzed [14]. This foam was a reticulated vitreous carbon (RVC) foam. These foams could be made with a variety of pore sizes and can also be coated with things like silicon carbide to manipulate the thermal and structural properties. The foam could also be manufactured with forced anisotropy to increase the structural strength of the material in certain directions. Some of these options for Ultramet foams were explored as part of the larger PSP development, but the focus of this dissertation was Ultramet 100 ppi 3% foam.

Similarly, ERG manufactured an RVC foam using a patented process that is marketed as Duocel®. This foam could be compressed to achieve anisotropic material properties. The method was also branded for metallic foams. For this dissertation, the focus of the testing was on ERG Duocel® 100 ppi 3% carbon foam. Traditional applications for this foam were acoustic regulation, porous electrodes and filters [15]. In this study, another foam type that was considered was GraFoam which was a mixed open and closed cell foam that was marketed as a composite tooling foam [16]. GraFoam-FPA02, GraFoam-FPA05 and GraFoam-FPA10 were analyzed, where the number at the end of the product denotes the relative density of the foam. Calcarb® was marketed as rigid insulation for

high temperature furnaces. It came as a pressed board of millimeter length scale fibers in a phenolic resin [17]. Given that its original application was not for a lightweight foam but instead furnace insulation, this foam was the densest. The Calcarb® foam was fibrous, which was a contrast to the other foams that are either open or mixed open and closed cell.

Figure 2-3 shows scanning electron microscope (SEM) images of the three structure types that were present in this study. In this case, the ERG Duocel®, on the far left, was an open celled foam with tetrahedron shapes; the GraFoam FPA-05, in the middle, was a mixed open and closed celled foam with varying sizes of cells; and, the Calcarb® standard board was the fibrous pressed board on the far right.

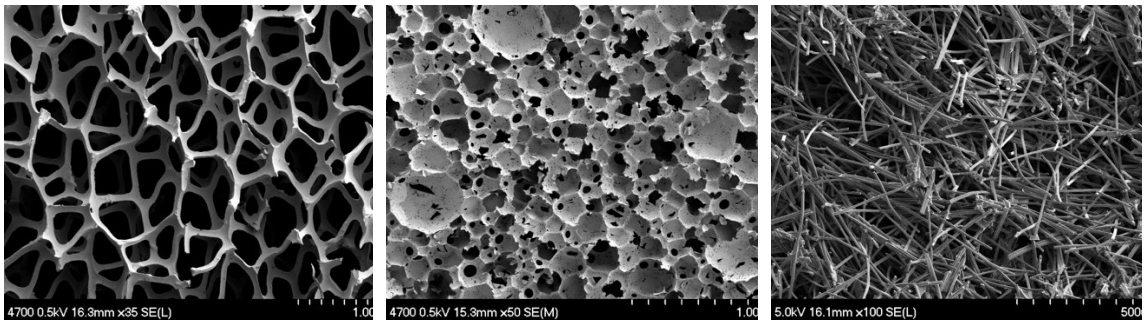

Figure 2-3 ERG Duocel® 100 ppi 3%, GraFoam FPA-05, and Calcarb® Standard Board are shown from left to right. The structure of the ERG Duocel® 100 ppi was open celled with ligands in tetrahedron shapes. The GraFoam FPA-05 was mixed open and closed celled with varying sizes of cells. The Calcarb® was a fibrous pressed board. (Courtesy of Ryan Deacon)

The Ultramet 100 ppi 3% under study had the same structure and density as the ERG 100 ppi 3% but was just made by a different manufacturer. The GraFoam FPA-05 was a mixed open and closed celled foam and was the middle density of the GraFoams under study. The structure for all three foams were similar, however the foams were varied in density. Finally, the Calcarb® was the densest foam under study though similar

in density to the GraFoam-10. It had a fibrous structure as shown in Figure 2-3. The Calcarb® did not have continuous pathways but was composed of disparate fibers. While this structure was very good for effective thermal conductivity disruption, it is not good for structural properties as continuous load paths benefit structural properties.

To give another view of the differences in cross section for the foams, Figure 2-4 are polished cross sections of the ERG Duocel® and the Calcarb®. These images are on the same scale and present a very different cross section from one another. Without the 3-D context, it might seem like the image on the right would be the less conductive of the two since there is less surface area in the cross section. In the figure, the white area is the structure of the foam while the grey is open area that has been filled with resin for imaging purposes. However, the effective thermal conductivity does not scale purely in this dimension as will be shown in later sections.

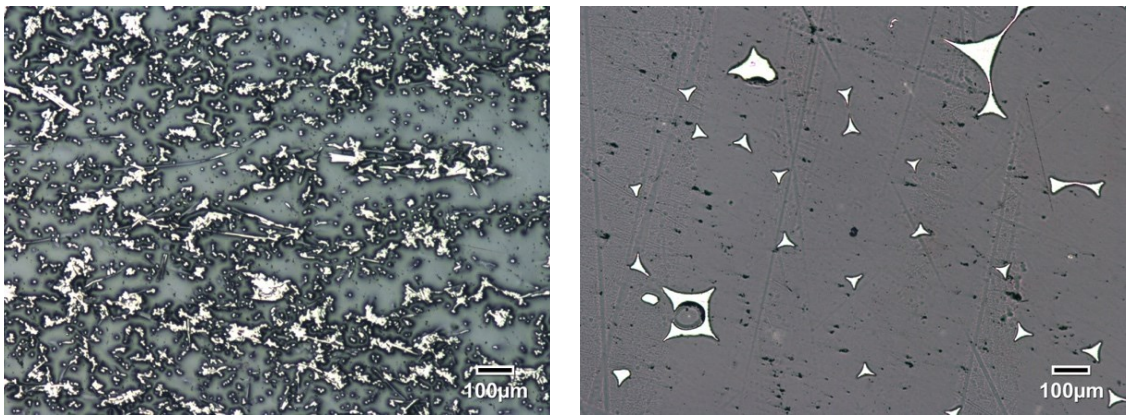

Figure 2-4 Calcarb® cross section and ERG cross section. The white area is foam structure while the grey is open space that has been filed with resin for the purposes of preparing the sample for imagery. (Courtesy of Ryan Deacon)

The Ultramet 100 ppi 3% and the ERG 100 ppi 3% had the same relative density, were similar in structure, and were both open celled foams. These foams offered a

comparison base in the measurements taken for this study. The GrafTech foams, FPA-02, FPA-05 and FPA-10, also offered a scaled comparison as they are all mixed open and closed celled foams made by the same manufacturer with similar processes but had different relative densities. Finally, the Calcarb® and GrafTech FPA-10 had the same relative density, so these foams were used as a comparison for the differences in structure between the foams. These varying foams allowed for comparisons in absolute density, relative density, and structure which were examined further in this dissertation.

Ultimately many factors drove the design of the PSP TPS. While the materials properties discussed here played a role in the overall TPS development, for rapid development of systems such as the PSP TPS, considerations such as manufacturing size and capabilities played a significant role in final decisions. For the PSP TPS to be used on the final spacecraft, it first needed to be shown to be feasible to manufacture multiple full-scale articles, subscale articles, and coupons, all in a short period of time. Additionally, minimizing joints was an overarching driver in design, because joints complicate the interplay between thermal and structural properties.

2.3. Historical References of Foam Behavior

The literature review shows that there has been extensive modeling of foam in general, and of carbon foam specifically, but no holistic understanding of the real foam behavior. There are models and published results that give a foundation for understanding the behavior of lattice materials such as foams. However, these models are limited in use because they are not very realistic when compared to the less idealized as-manufactured real-world foams. These limitations led to the need to

perform coupon tests on the foams of interest and this information was used to drive the development of subscale and full-scale structural and thermal testing. Despite the limitations of the classic models, they are useful to understand the behavior of foams.

This section outlines the work done by Gibson and Ashby to understand the behavior of foams as well as more recent work on foams [18-23]. Traditionally, foam behavior has been characterized based on its relative density. The classic authoritative literature experts on foams are Gibson and Ashby, whose work provided the foundation for understanding and modeling foam behavior [23]. Gibson and Ashby outlined the history of foams and stressed how these lattice structures have been used by humans for centuries. In nature, foams can be found in wood, cork, bone, and coral, and all possess unique properties. Many of the foods we eat are foams. Meringue, breads and cornflakes are food foams that rely on mechanical beating, yeast as a blowing agent and steam as a blowing agent [23]. Foams have a large range in relative densities, from 5% to 20% for polymeric foams, while most softwoods having a relative density between 15% and 40%. Generally, however, foams are classified as materials with a relative density of less than 30% since that is where the transition to solid with isolated pores occurs [23].

Foams have long been used for their unique properties, specifically their low mass. As Gibson and Ashby noted foams are useful in thermal, electrical and acoustic applications due to their generally low effective thermal conductivity, low dielectric loss and sound absorption ability [23]. They also noted that due to their properties, foams are often found as thermal insulators, packaging components, cores in structural

sandwich panels and as bodies used for buoyancy. All of these reasons made foams a natural choice for an application that needed a high strength to mass ratio and needed to be thermally insulative.

While this history of foams is interesting, the foams relevant to the current course of study are low density carbon foam insulators. Wood, bone and coral possess unique specific strengths, but low-density carbon foam insulators have a unique capability in space due to their thermal insulation properties as well as their ultra-low density. These foams are lower in density than traditional structural foams. However, they can be explored using the similar methodologies.

2.4. Thermal Properties of Cellular Materials

In general, mathematical models that have been developed for foam effective thermal conductivity have focused on cryogenic to room temperature properties [23-25]. More recently, models and testing have been extending to higher temperatures above 800°C but this is still an emerging field of research [26-28].

The foundational work on foams by Gibson and Ashby relied on the properties of the solid scaled by the relative density. Gibson and Ashby addressed the thermal properties of foams by starting with a closed cell model and noted that the thermal transfer of a foam is actually made up of multiple components that add together: conduction through the solid material, conduction through the gas if present, convection within the cells, and radiation within the cells. They showed that for a closed cell polyurethane foam, the dominant component is the conduction through the gas assuming there was no convection due to the size of the voids within the cells [23]. As

Gibson and Ashby note, "closed-cell foams have the lowest thermal conductivity of any conventional non-vacuum insulation. Several factors combine to limit heat flow in foams: the low volume fraction of the solid phase; the small cell size which virtually suppresses convection and reduces radiation through repeated absorption and reflection at the cell walls; and the poor conductivity of the enclosed gas," [23]. However, examining the model that Gibson and Ashby presented for the effective thermal conductivity, the PSP environment does not lead to the same conclusion.

For the application of interest, closed cell foams were not an option because of the launch environment; all objects on the spacecraft needed to be able to vent during the ascent to reduce loading that occurs due to vacuum. Therefore, only mixed open and closed cell foams and entirely open celled foams were options. These foams, when used in vacuum, employ only the conduction and radiation components. At low temperatures, the radiative component plays a small role. Yet at high temperatures, the radiative component is more dominant, as the equation is varying with T^4. Additionally, in vacuum, the conduction and convection components of the gas would not be present. The critical features to be considered when calculating the heat transfer such of these foams are the solid conduction and the radiative component.

Gibson and Ashby offered several useful observations on the thermal behavior of foam. First, they note, “heat transfer increases with cell size... This is partly because radiation is reflected less often in a foam with large cells and partly because, for cells of more than 10 mm or so in diameter, cell convection starts to contribute,” [23]. In their simplest form, the Gibson and Ashby equations scale the solid properties by relative

density of the foam, but this observation hints at the concept that the structure of the foam does play a role in properties, particularly when distinguishing between two similar foams.

These observations led to a series of equations based on the theory of relative density. Gibson and Ashby noted that the important properties for heat conduction are thermal conductivity, λ, and thermal diffusivity, a, [23]. The thermal property of interest for this application was the steady-state effective thermal transport or the backside temperature state that will be reached under a constant incoming heat flux. This property, instead of the transient property, was of interest because the path profile around the Sun leads to hours and days of time at temperature. The exposure of the PSP TPS is significantly longer than the timescale for which transient effects are present, so the transient effects can be considered negligible. This state is in contrast to other thermal protection systems that are used for re-entry into Earth's atmosphere or for entry into another planet. These systems rely on the transient properties, low thermal diffusivity, to keep the temperatures lower. Thankfully, it is easier to create proper test conditions for the steady state case.

Ultimately, Gibson and Ashby posed equations for thermal diffusivity, thermal conductivity, the radiative component of the thermal property and the effective thermal conductivity. Eq. (1) is Gibson and Ashby's equation for thermal diffusivity [23]:

$$a = \frac{\lambda}{\rho C_p} \tag{1}$$

Where:
$a = \ thermal\ diffusivity$
$\lambda = thermal\ conductivity$
$\rho = density$
$C_p = specific\ heat$

This relationship between the thermal diffusivity and the effective thermal conductivity was used for the thermal diffusivity test methods, which were some of the methods used in this research. Gibson and Ashby also looked at the components that make up the effective thermal conductivity and break it down into components. Eq. (2) gives the equation for thermal transport broken down by component, [23].

$$\lambda^* = \lambda_s^* + \lambda_g^* + \lambda_c^* + \lambda_r^* \tag{2}$$

Where:
$\lambda_s^* = conduction\ through\ the\ solid\ component$
$\lambda_g^* = conduction\ through\ the\ gas\ component$
$\lambda_c^* = convection\ of\ the\ gas\ through\ the\ cells$
$\lambda_r^* = radiation\ throughout\ the\ foam$

The equation above separates the foam effective thermal conductivity into the components of conduction through the gas and solid, convection of the gas and solid and radiation through the foam. Breaking this equation into these components allowed Gibson and Ashby to tackle each component independently. They assumed an efficiency factor of 2/3 on the solid conductivity and that the cells are sufficiently small to repress the convection in the foam, which results in Eq. (3), [23].

$$\lambda^* = \frac{2}{3}\left(\frac{\rho^*}{\rho_s}\right)\lambda_s + \left(1 - \frac{\rho^*}{\rho_s}\right)\lambda_g + 4\beta_1\sigma\bar{T}^3 texp - (K_s\frac{\rho^*}{\rho_s}t) \quad (3)$$

Where:
$\rho^* = density\ of\ the\ foam$
$\rho_s = density\ of\ the\ solid$
$\lambda_s = thermal\ conductivity\ of\ the\ solid$
$\lambda_g = thermal\ conductivity\ of\ the\ gas\ present\ in\ the\ foam$
$\beta_1 = a\ constant\ that\ represents\ the\ emissivity\ of\ the\ surface$
$\sigma = Stefan's\ constant$
$\bar{T} = mean\ temperature\frac{T_1 + T_0}{2}$
$K_s = extinction\ coeffiecent\ of\ the\ solid$
$t = thickness\ of\ the\ foam$

The three components of this equation are the conduction of the solid, conduction of the gas and the radiative component through the foam. The first term describes the solid component of the foam. It depends on the ratio of the thermal conductivity of the solid and the relative density of the foam of interest. The equations include an efficiency factor of 2/3. It suggests that there are more complex effects that the model does not capture and may be a source of uncertainty in the model. The second component describes the conduction through the gas within the foam, which depends on the inverse of the relative density of the foam. The final term is the radiative component of the effective thermal conductivity. This component is based on constants related to radiation and the optical properties of the foam.

The density-based approach of Gibson and Ashby was adequate for understanding the gross behavior of foams of varying relative density. However, their work also showed that density alone might not be able to completely predict the behavior. The hypothesis of this dissertation is that shape and thickness influence the results of testing and must be taken into account beyond just the relative density of the foam. Understanding these influences is critical to being able to use these carbon foams to build the full-scale PSP TPS.

2.5. Structural Properties of Cellular Materials

Gibson and Ashby developed equations for the elastic behavior of foam by examining a periodic cubic structure, which can be used to understand their structural properties. By defining relative density, $\frac{\rho^*}{\rho_s}$, *shape anisotropy ratios* R_{12} and R_{13}, and whether a foam is open or closed celled, they were able to show that the linear elastic behavior of open celled foams is dominated by the cell wall or ligand bending and derive equations for Young's modulus and shear modulus. Building on the model that they developed for linear-elastic honeycomb deformation, Gibson and Ashby derived a model for a simple open-cell foam starting with a periodic cube of dimension, *l*, and wall thickness, *t*. Figure 2-5 shows a simple periodic element of an open celled foam that assumes an isotropic structure.

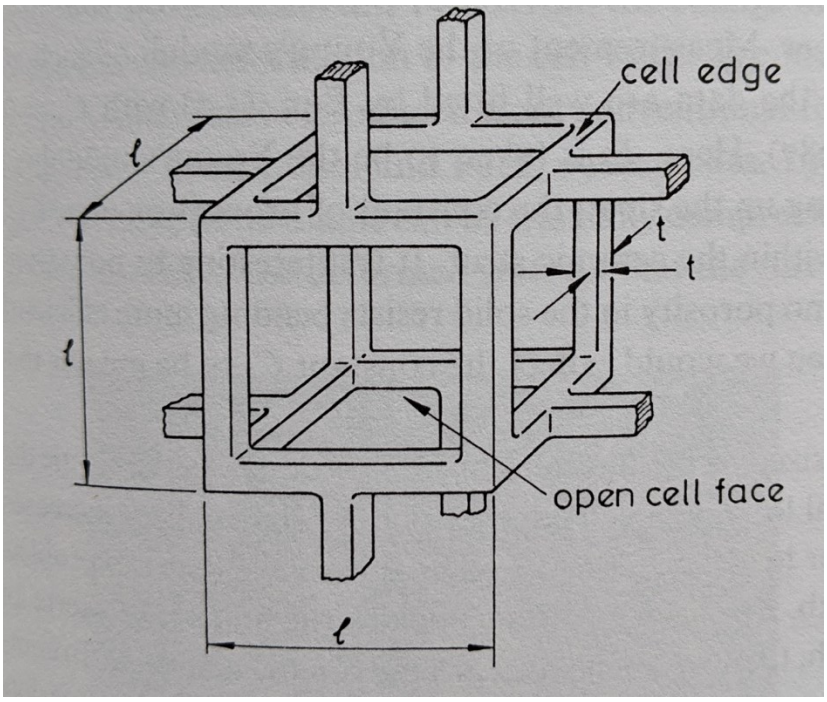

Figure 2-5 Simple periodic foam element used for the Gibson and Ashby model [23]

Using this framework Gibson and Ashby developed equations for isotropic foams assuming a compressive loading. While all the foams studied were anisotropic, the isotropic model illuminates the modes of failure for the foam. Gibson and Ashby noted that, in compression, as the load on the cell increases the elastic distortion causing a moment on the edge before it buckles. This moment was not accounted for in the derivation above so, in practice at finite strains, the modulus in compression should be smaller than in tension [23]. For brittle foams such as the ones considered for this study, brittle fracture dominates the failure. “In the brittle foam a crack nucleates at a weak cell wall or pre-existing flaw and propagates catastrophically, giving fast brittle fracture,” [29]. The population of pre-existing flaws in real-world, meters-long foams components is difficult to inspect or determine. Additionally, flaws could be introduced through testing, manufacturing or operation.

Gibson and Ashby noted that these equations are simplifications that match the behavior of real-world foams but have limitations. Real world foams have anisotropy both in the material and in the structure. Additionally, there may be flaws in the materials due to manufacturing. These flaws are particularly important to the failure capabilities of these brittle foams.

2.5.1. Anisotropic Models for Linear Elastic Behavior

All the foams studied in this dissertation presented with anisotropy. Gibson and Ashby expanded beyond on the simple periodic open foam to develop equations assuming architectural or structural anisotropy which was driven by the geometric differences in the lengths of the cell walls. Figure 2-6 represents a simplified anisotropic foam geometry.

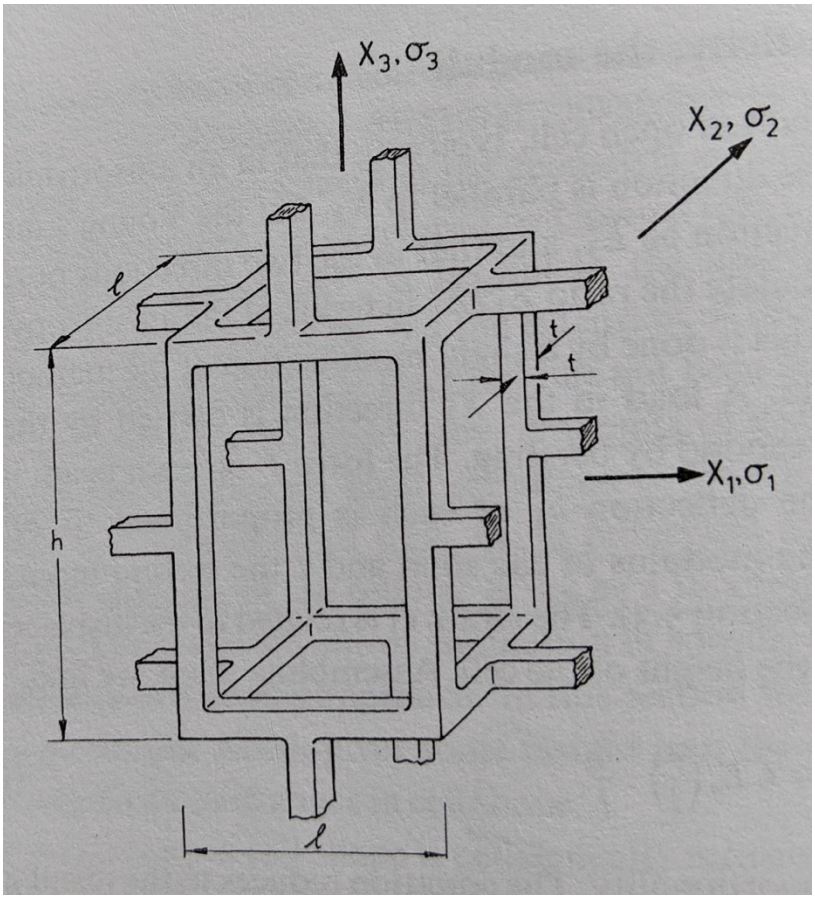

Figure 2-6 Anisotropic simple periodic foam structure used for the Gibson and Ashby models [23]

In this figure, the third dimension is the elongated direction. Building on the modeling that they used for honeycomb structures, Gibson and Ashby defined the effects of this anisotropy on the modulus in the third dimension as shown in Eq. (4) [23].

$$E_3^* = \frac{\sigma_3}{\varepsilon_3} = \frac{CE_sIh}{l^5} = CE_s\left(\frac{t}{l}\right)^4\left(\frac{h}{l}\right) \quad (4)$$

Where:

$E_3^* = Young's\ Modulus\ of\ the\ Foam\ in\ the\ third\ dimension$
$\sigma_3 = uniaxial\ stress\ applied\ to\ the\ foam$
$\varepsilon_3 = strain$
$C = a\ constant\ developed\ to\ account\ for\ proportional\ geometric\ constraints$
$E_s = Young's\ modulus\ for\ the\ cell\ ligand\ material$
$I = Second\ moment\ of\ Inertia\ of\ a\ cell\ ligand$
$l = cell\ edge\ length\ as\ shown\ in$ Figure 2-6
$h = cell\ edge\ height\ as\ shown\ in$ Figure 2-6

Using the relationship between the deflection of the shorter-length beams and longer-length beams per beam theory, the equation for the modulus in the other directions can be derived. This derivation is shown in Eq. (5) [23].

$$E_1^* = \frac{\sigma_1}{\varepsilon_1} = \frac{CE_sI}{2h}\left(\frac{1}{l^3} + \frac{1}{h^3}\right) \tag{5}$$

Where:
$E_3^* = Young's\ Modulus\ of\ the\ Foam\ in\ the\ third\ dimension$
$\sigma_3 = uniaxial\ stress\ applied\ to\ the\ foam$
$\varepsilon_3 = strain$
$C = a\ constant\ developed\ to\ account\ for\ proportional\ geometric\ constrants$
$E_s = Young's\ modulus\ for\ the\ cell\ ligand\ material$
$I = second\ moment\ of\ Inertia\ of\ a\ cell\ ligand$
$l = cell\ edge\ length\ as\ shown\ in$ Figure 2-6
$h = cell\ edge\ height\ as\ shown\ in$ Figure 2-6

The Young's modulus and the shear modulus in each direction can be related by the ratio of anisotropy relating *h* and *l*. Eq. (6) and Eq. (7) are for Young's modulus and shear modulus respectively [23]. The shear modulus ratio depends less on the anisotropy of the foam:

$$\frac{E_3^*}{E_1^*} = \frac{2R^2}{\left(1 + \left(\frac{1}{R}\right)^3\right)} \quad (6)$$

Where:
$E_3^* = Young's\ Modulus\ of\ the\ Foam\ in\ the\ third\ dimension$
$E_1^* = Young's\ Modulus\ of\ the\ Foam\ in\ the\ other\ dimensions$
$R = \frac{h}{l}$
$l = cell\ edge\ length\ as\ shown\ in$ Figure 2-6
$h = cell\ edge\ height\ as\ shown\ in$ Figure 2-6

$$\frac{G_{31}^*}{G_{12}^*} = \frac{2}{(1 + R)} \quad (7)$$

Where:
$G_{31}^* = Shear\ Modulus\ of\ the\ Foam\ in\ the\ third\ related\ to\ first$
$G_{12}^* = Shear\ Modulus\ of\ the\ Foam\ in\ the\ symmetric\ dimensions$
$R = \frac{h}{l}$
$l = cell\ edge\ length\ as\ shown\ in$ Figure 2-6
$h = cell\ edge\ height\ as\ shown\ in$ Figure 2-6

Understanding the effect of anisotropy on structural behavior is important since anisotropy is present in most foams [29] and was present in all foams studied here.

Despite the presence of anisotropy in most foams, it is difficult to model. As Gibson and

Ashby note, “A rigorous treatment of anisotropy poses considerable theoretical difficulties,” [23]. Part of the difficulty arises from the inability to separate out the shape and structure variation (structural anisotropy) and the material variation (material anisotropy). While both can be measured separately to a degree, coupon testing will inevitably have both present. In fact, Gibson and Ashby note that in nature, for example in bone, the two anisotropies work in tandem to produce desired structural properties. The Gibson and Ashby hypothesis in this anisotropic model was that the variation in properties in different direction was driven by this geometrical variation or structural anisotropy. This hypothesis is tested in this dissertation using coupon test data of carbon foams.

2.5.2. Discussion of Anisotropy in Literature

Material anisotropy, structural anisotropy, the presence of flaws and the mathematical imperfection of real-world foams have all been researched to understand the behavior of carbon foams. Fundamentally, the complexity of real-world foams makes modeling difficult and extensive material testing is required to understand the behavior of large-scale foams. Material anisotropy, or the variation in the material itself within the struts, can be difficult to measure. As Gibson and Ashby noted, work by Choi, et al., and Ryan and Williams demonstrated the difficulty in measuring cell-wall moduli [30, 31]. The difficulty arose from the small samples and the geometric variability within the samples or variation in the material in the samples. These challenges are amplified in real world foams. Foams that are outside the geometric perfection of modeling have variability that make testing difficult.

Structural anisotropy presents similar challenges for modeling. Attempts in the literature to deduce the effects of structural anisotropy still assumed simplified periodic shapes like the Gibson and Ashby example above. Foams rarely adhere to this type of rigid mathematical structure unless they are specifically printed or designed that way. While this modeling provides insight into material behavior, the foams and materials that constitute the PSP TPS were composed of materials that have been manufactured, and therefore do not have the same regular periodic structure as these idealized models. These papers investigated the effects of variations in the materials and periodic lattice on the material property data [32]. Other research has utilized imaging to characterize the structural behavior of foams [33]. It is not surprising that material and structural anisotropy effect foam behavior, but it is not well understood how this would affect the properties of the carbon foam under study.

In addition to the structural and material anisotropy, flaws in the material are an important factor in brittle foams such as carbon foams of interest here. Statistical probability of failure must be evaluated to accurately predict failure. As Letellier, et al., note:

> *For brittle materials, it is nevertheless known that fracture is initiated by inhomogeneities and flaws. As their distribution in the structure is generally non-uniform, the sample's volume has an influence on the resultant mechanical properties, as predicted by Weibull's theory. For instance, long struts are more likely to break than shorter ones when compressed in the same conditions. It follows that the number of struts broken at a given stress in brittle foams with large cells is likely to be proportionally higher than in similar materials having smaller cells, [20].*

Many authors have addressed the complexities above and expanded the mathematical modeling to predict the behavior of realistic foams and structures by constructing regular lattice simulations [19, 32, 34-37]. There has been renewed academic focus on lattice structures due to the possibilities in additive manufacturing. These modeling efforts are often based on the periodic foam structures that Gibson and Ashby first developed. For example, Triantafillou and Gibson developed predicted strength data for uniaxial, biaxial and axisymmetric loading from bulk material properties, the properties of a single cell strut and the failure mechanism [38]. These results were compared to test data from the appropriately loaded testing. There is significant variation (on the order of 10%) in the results, which is attributed to macrocracking and manufacturing variability. Using the equations developed for tensile rupture of bent cell struts, elastic buckling and brittle fracture, a failure surface is developed for carbon foams by Triantafillou and Gibson but the variability in the test data made it difficult to extend these results to other similar materials such as the carbon foams under study here.

Building on these modeling efforts, Valdevit, et al., constructed a design framework for mathematically solving for the optimal design of cellular structures around several parameters. The authors acknowledge the limitations to some of the assumptions in material properties but note that this design framework is a powerful tool in optimizing lattice structures [39]. Sihn and Roy also developed a geometric mathematical model and used it to run parametric studies in ANSYS [21]. Limitations

due to the complexity of the carbon foam led them to make assumptions and simplifications which may have had affected their results. The authors focused on the unit cell as the defining volume for analysis. They argued that analyzing several cells together is too numerically intensive. However, this approach is of limited utility because it assumes the behavior of a cell is not affected by those around it. Additionally, their models loaded the unit cell in uniaxial strain in one direction and constrained deformation in the two perpendicular directions and assumed isotropy of material properties [21]. These modeling efforts are beginning to provide a scientific framework of the design of unit cells, but they are still very rudimentary and their limitations mean that they do not model the behavior of large real foam structures.

To address some of the difficulty in measuring the properties of these foam structures due to the difficulties in handling, Salari-Sharif and Valdevit used non-contacting vibrometry and finite element analysis to determine the Young's modulus of an ultralight lattice structure. Their approach yielded higher Young's Modulus than traditional Instron approaches; but the results from their testing are consistent with their finite element predictions. The authors attribute the differences to the drawbacks of the traditional methods which tend to cause localized failure at the loading surfaces [40].

Letellier, et al., surveyed the application of the Gibson and Ashby model over studies done by Zhang, Maiti, Brenzy, and Gibson [20]. The authors found a variety of constants that were inconsistent with each other but noted that the inherent assumptions in the Gibson and Ashby model, such as the knowledge of strut strength,

probably led to these inconsistencies. They also noted that previous literature indicates that mechanical properties of carbon foam can depend on both the relative density and the average cell size. However, the authors noted that their findings show that the compressive strength and modulus's influence are dominated by relative density, and that the compressive modulus should be independent of cell size. While Letellier, et al., found that their data confirmed that the failure mechanism of carbon foams was strut failure in bending as predicted by Gibson and Ashby, they found that the failure also related to the percent of material in the struts and not just the material properties of the struts themselves as the Gibson and Ashby model predicts.

In addition to the foam literature, there has been work into the theoretical limits for a multiphase material for elastic modulus and effective thermal conductivity. Hashin and Shtrikman defined the bounds for the elastic modulus of a multiphase material [41] and this work has been built on since to optimize additive manufactured structures that resemble the foam structures of interest for this work. Tarantino and Zerhouni showed that random distribution of various sized spherical voids down to a relative porosity of approximately 25% approached the Hashin-Shrikman bounds [42, 43]. Unlike the foams under study here, these foam-like structures were optimized for a random distribution of voids, ensured isotropic materials and were printed at the small scale. The theoretical bounds of effective thermal conductivity for a multiphase material has also been extensively studied [44, 45]. Carson et al. proposed differentiating between internal and external porosity [46]. Internal multiphase materials, such as the foams under study here, were shown to have a generally higher effective thermal conductivity than

external porous materials. The authors noted that there is no unifying model for internal or external porosity even at room temperature [46]. Similarly to the Gibson and Ashby theory, the literature on theoretical bounds of effective thermal conductivity is focused on a gas/solid multiphase relationship at or near room temperature.

The literature review shows that there has been extensive modeling of foam in general, and of carbon foam specifically, but no holistic understanding of the real foam behavior. This lack of universal understanding means that it is difficult to translate the general results from literature to the specific behavior of these large-scale carbon foams like those used in the PSP heat shield. Anisotropy, flaws and material property variation are all difficult to model and independent of each other. Since these elements are difficult to separate from each other, models with minimal material property data are not a realistic approach to understanding the carbon foam. An extensive coupon test program in multiple directions with loading in tension, compression and shear was undertaken for the foams in this study. Building on this coupon data, subscale and full-scale models was built and tested against. While coupon testing and modeling give insight into foam behavior, a multiscale test program was needed to qualify and build the PSP TPS.

2.6. Testing for Qualification of Space Components

Qualifying new technologies for space is a difficult endeavor due to the harsh environments and the necessary reliability for a component or spacecraft that cannot be retrieved or fixed. NASA developed a framework for understanding this process in the 1970s and has been refining it ever since. Figure 2-7 is a diagram of the current NASA

Technology Readiness Level (TRL) framework which describes the path from a basic research concept through a successful flight technology demonstration.

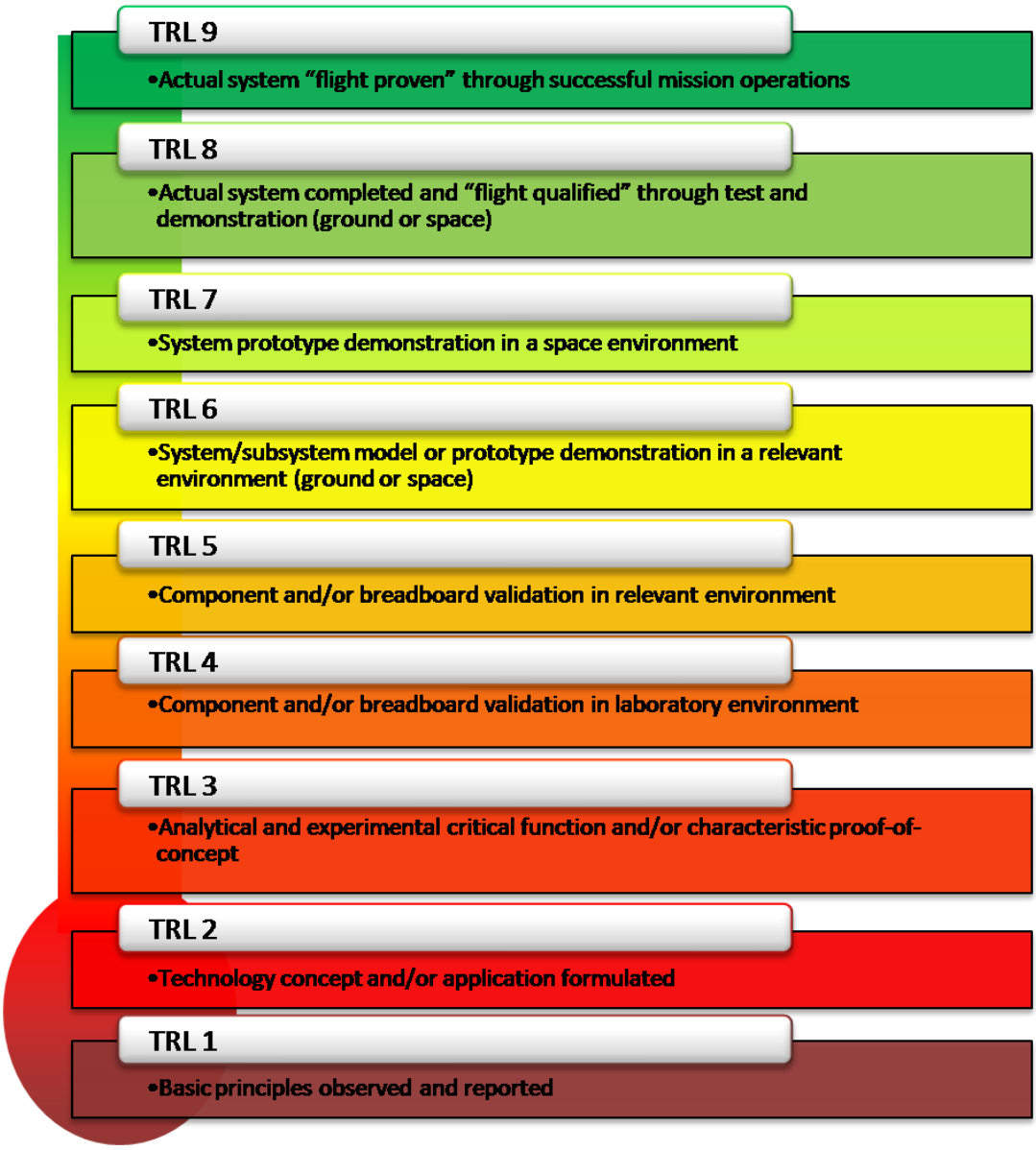

Figure 2-7 NASA's Technology Readiness Framework which describes the development process from a basic research project to a flight technology application [47]

Components and technologies begin at the bottom of the scale and work through experimental results, prototype proof of concept, subscale testing, system prototyping and then into full flight qualification. This approach is used to determine if a new

technology is ready to be flown as part of a mission. Most NASA missions are the first and only example of a system, and require a large financial investment to design, test and launch. While they might be considered prototypes, they must work as intended the first time to successfully accomplish mission and science objectives, and, for manned missions, ensure the safety of the crew. “System failures can be costly in virtually any environment, but perhaps none more so than in space–where even a single computing event upset can bring an untimely end to an entire and very expensive mission,” [48]. Every component and the system as a whole must work as designed. In many cases, for fly-bys of planets or landings, there is only one opportunity for the system to function as designed. As a result, it is extremely important that system testing be well designed to avoid any failures.

As Olechowski, et al., note, the NASA TRL definitions have spread beyond the context of NASA and aerospace applications as a way to indicate and track the maturity of high-risk technologies. Through interviewing practioners across industries, the authors found that the TRL framework is being increasingly used outside of aerospace, but there are challenges that hamper its effectiveness, particularly in system complexity, planning and review and assessment validity [49].

The technology readiness levels are broad, and when needing to implement a test and validation program on a new system that has limitations on capabilities to *test as you fly,* the path towards successful launch is not obvious. The work in this dissertation fits into this larger qualification plan and framework. The testing of the materials at

multiple scales enabled an understanding of the behavior of the PSP TPS during launch and at the Sun.

2.7. Summary

Gibson and Ashby developed equations for linear elasticity based on simple periodic open celled foam models. In their writing and in work done after, it was clear that real world foams are more complex than these simple models. A review of this literature suggests that small deviations from this simplified model may be developed, but that there are limits to the practical application of these deviations due to the issues noted here. These limitations are the foundation of this dissertation. When moving away from simplified, mathematically perfect foam structures, models cannot be used to bridge the distance between coupon testing and full-scale units. For space qualification, the materials must be very well understood given the reliability requirements for a high value NASA mission. These factors drove an approach to do multiscale testing of materials to bridge the understanding of the material at multiple levels of use and ultimately ensure the success of Parker Solar Probe.

CHAPTER 3. Thermal Properties

3.1. Thermal Properties Approach

To have a successful PSP mission, the temperatures that are realized on either side of the heat shield needed to be understood and managed. The temperature of the heat shield depends on several factors, including distance from the Sun, optical properties of the outer surfaces and thermal conductivity through the heat shield. These elements can be deconstructed and understood as separate phenomena. For the purposes of this dissertation, the focus was on the effective thermal conductivity of the carbon foam that forms the core of the heat shield.

The philosophy of space flight hardware is *test as you fly, fly as you test* but the constraints, the inability to get a large test chamber to the appropriate temperatures in the appropriate vacuum for long holds, of testing facilities meant that high temperature full-scale flight thermal testing on the heat shield was impossible given the resources and timeline. Therefore, an understanding of the thermal performance of the heat shield had to be developed through coupon testing, subscale testing and modeling. Each of these elements have limitations. Coupon testing inherently did not match the boundary conditions of the full-scale unit and therefore had to be complimented with modeling as a bridge to understand full-scale performance. Flaws in the modeling, errors in testing, conditions not captured in the coupon testing or a misunderstanding of the relationship between the full-scale unit and the coupon testing could all lead to a poor predictions of full-scale behavior. Generally, coupon testing was not meant to

replicate the behavior of the actual system but instead was meant to isolate a particular material property, and therefore the coupon was fundamentally different from the full-scale system. Subscale testing was meant to more accurately represent the system. In particular, edge effects in both thermal and structural testing often needed to be understood and mitigated.

Extensive testing was done at the coupon, subscale and full scale. The test program, which spanned institutions across the United States, from Armstrong Flight Research Center (AFRC) to Johnson Space Center (JSC) to Oak Ridge National Laboratory (ORNL), involved many different coupon test approaches, subscale tests with a variety of heat sources, attempts at full scale hot testing and qualification tests with full scale units in cold testing. These tests were part of a larger testing and analysis program that qualified the flight PSP TPS. The results documented here are a limited subset of the testing program, primarily focused on the effective thermal conductivity testing of the carbon foam.

Understanding the effective thermal conductivity of the carbon foams under study was needed to assure their thermal performance in the thermal protection system. There are a variety of standard protocols for determining the effective thermal conductivity of a given material. However, the studied foams were porous and fragile, which had an impact on the testing. Additionally, the environment of interest presents considerable challenges as testing at ultra-high temperatures and in a space-like vacuum was hard to replicate on Earth and therefore it was difficult to get precise results. Given all these limitations, testing was approached in a variety of ways.

The thermal behavior of a material is driven by three factors: the thermal conduction of the materials present, the convection driven by gases that are present and the radiative component. Given that the use case of the material will be in the vacuum of space, which eliminates convection, it was important to understand the effective conductivity in vacuum, which is the combination of the solid conductivity and radiation, in these conditions. Traditional American Society for Testing and Materials (ASTM) methods focus on determining the conduction of heat in a solid and therefore rely on thin, wide samples to avoid boundary effects. This method does not capture the radiative properties that occur within a low-density foam. The limitations of coupon testing meant that a broad testing approach that included both coupon testing and subscale testing was needed to predict the thermal behavior the PSP TPS will have at the Sun. This chapter starts by describing the test methods used and examining the coupon data and the applicability of the Gibson and Ashby model for the carbon foam and environment of interest in this dissertation. The coupon data will then be used to understand the material mechanisms that can affect effective thermal conductivity. Next, the subscale testing done at ORNL will be compared to the coupon results and the subscale unit testing will be used to understand how effective thermal conductivity is influenced by thickness and size scale. Finally, full-scale testing and its validation of the design will be considered.

3.2. Coupon Testing Methodologies

In order to determine the effective thermal conductivity of the foam, JHUAPL contracted effective thermal conductivity testing to a few testing organizations:

Precision Measurements and Instruments Corporation (PMIC) in Corvallis, OR and Thermophysical Properties Research Laboratory (TPRL) in West Lafayette, IN. This testing was overseen and directed by me and supplemented the subscale testing and modeling that was also performed to determine the performance of the PSP TPS. The environments that the tests were conducted in are critical: the range of test temperature, from room temperature to 1500°C, as well as the vacuum levels, from $p \leq 1.0 \times 10^{-2}$ torr to $p \leq 2.0 \times 10^{-5}$ torr, that were achieved during testing influenced the results and their applicability to the PSP TPS performance. Vacuum levels represent the lack of air in a given space or test. Therefore, the smaller the number, the better the vacuum and the more representative it is of deep space, where no air is present. High vacuum is used to refer to smaller numbers while low vacuum is used to refer to larger numbers. The test methodologies for coupon testing are outlined in Table 3. These methods are discussed in detail in the following sections.

Table 3 Overview of the effective thermal conductivity coupon tests

Testing Organization	Standard Name	Descriptive Name	Temperature Ranges	Environment
PMIC	ASTM C1114	Guarded Hot Plate Method	100°C-1100°C	$p \leq 2.0 \times 10^{-5}$ torr
TPRL	ASTM E1461	Thermal Diffusivity Method	23°C-1500°C	$p \leq 1.0 \times 10^{-2}$ torr and 760 torr Argon
TPRL	N/A-TRPL Developed	3P	23°C-1000°C	$p \leq 1.0 \times 10^{-2}$ torr and 760 torr Argon

3.2.1. Guarded Hot Plate Testing

One of the standard test methods that was used was the guarded hot plate method, or ASTM standard C 1114. Table 4 lists the materials that were tested at PMIC using the guarded hot plate method.

Table 4 Test coupons for guarded hot plate testing [50]

Qty.	Specimen ID	Foam Type	Length (cm)	Width (cm)	Thickness (cm)
4	A	Calcarb Std Board	15.24	15.24	1.27
4	B	GrafTech FPA-02	15.24	15.24	1.27
4	C	ERG 100 ppi 3% Duocel	15.24	15.24	1.27
4	D	Ultramet 3% 100 ppi	15.24	15.24	1.27
4	E	GrafTech FPA-05	15.24	15.24	1.27
4	F	GrafTech FPA-10	15.24	15.24	1.27

This technique uses Fourier's First Law to determine the absolute steady-state effective thermal conductivity. This approach was in contrast to other methods which used a reference standard to compare the given material under test and determine its effective thermal conductivity. The setup of ASTM C 1114 is shown in Figure 3-1.

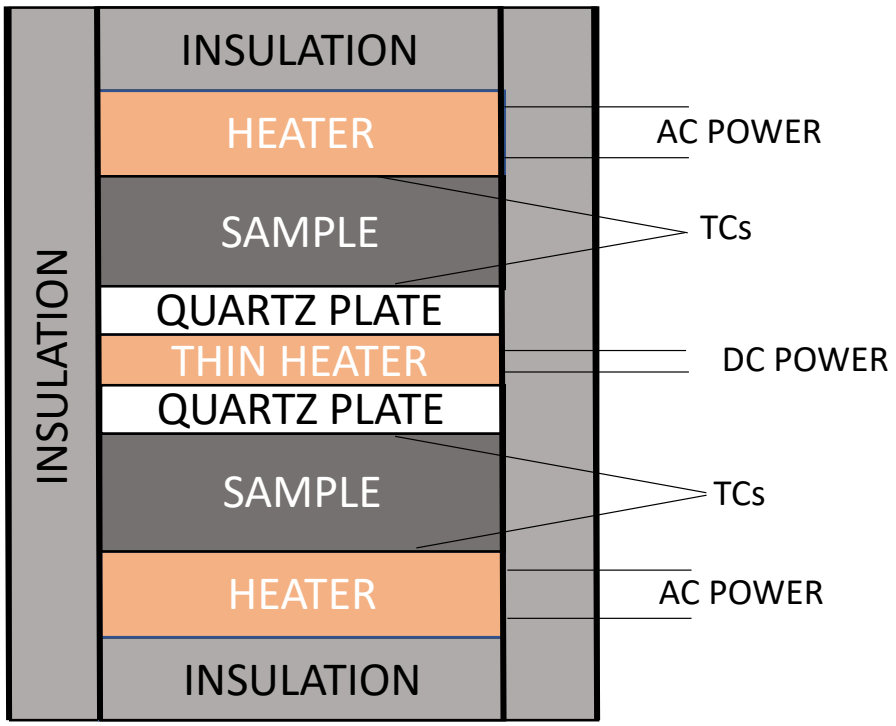

Figure 3-1 For ASTM test set up for guarded hot plate (GHP) testing, a pair of samples were surrounded by heaters and thermocouple readings are taken on either side, adapted from [50]

In this test, a pair of thin samples, which were 15.2 cm x 15.2 cm square and 1.27 cm thick, were sandwiched between heater plates. The two outer heater plates were set at a temperature slightly above the temperature at which the effective thermal conductivity is to be measured. Once the system stabilizes, the thin heater in the middle was set to a known power and the system was allowed to stabilize again. The effective thermal conductivity could be determined using [50]:

$$k = \left(\frac{t}{A}\right)\left(\frac{Q_t}{2}\right)\left(\frac{1}{\Delta T}\right)R_h R_e \tag{8}$$

where:

$k = calculated\ thermal\ conductivity\ \ [\frac{W}{mK}]$

$A = cross\ sectional\ area$

$t = thickness\ of\ the\ specimen\ under\ test\ [m]$

$Q_t = power\ on\ middle\ thin\ heater\ [W]$

$\Delta T = average\ temperature\ change\ due\ to\ the\ applied\ additional\ heat$

R_h

$= the\ ratio\ of\ the\ surface\ of\ the\ thin\ heater\ that\ is\ contacting\ the\ specimen$

$R_e = correction\ factor\ due\ to\ edge\ losses$

In this test, *Q, A,* and ΔT were the measured values. R_e and R_h were correction factors based on the geometry of the samples. $R_e$was unity for this testing because the samples meet the guidelines for ASTM C1114 and therefore did not require extra corrections for edge losses. For this testing, $R_h = 0.9415$ which represented the calculated ratio of the heater surface contacting the specimen to the total surface area of the heater [50]. Three type K thermocouples were used at all of the measurement interfaces and they were used to calculate the average temperature change across the sample, ΔT. This testing was done at high vacuum, where the pressure was never worse than 2x10^{-5} torr. Edge effects and degradation of the sample due to oxidation could have been sources of error, but precautions were taken to ensure the required vacuum levels were achieved and that the sample size was sufficiently wide. None of the samples changed dimensions as a result of the testing. Since these samples were carbon, the samples would oxidize in the presence of oxygen at high temperatures. Measurements of the power of the thin heater and the thermocouples for each sample were taken approximately every 100°C from room temperature to 1100°C.

3.3. Thermal Coupon Results: Ultramet 3% 100 ppi Foam

The first step was to compare the GHP Ultramet 100 ppi 3% data to the widely referenced Gibson and Ashby model [23] that scales effective thermal conductivity as a function of relative density. This model is directly intuitive, mechanics-based and widely employed, but it requires a few simplifying assumptions and comparing the experimental data to the model prediction allowed the limitations associated with those assumptions to be understood. First, the model assumes that the material is homogenous and isotropic. The foams studied here are neither ideally isotropic nor homogenous. As an example, the Ultramet 3% 100 ppi foam data was detailed as it is close to this ideal.

An interesting note is that Gibson and Ashby focused on foams generally used in insulation for cold storage. The temperature ranges explored in their work were more limited and colder than the temperatures of interest in this dissertation, up to 1300°C, and therefore the relative importance of conduction, convection and radiation were different between Gibson and Ashby and the PSP application. Moreover, their work focused on closed cell foams filled with an insulating gas whereas PSP operates in vacuum.

Gibson and Ashby broke down the effective thermal conductivity of foam into three components: solid conduction, conduction through the gas present, and radiation. They ignored convection due to the size of the pores. The guarded hot plate experiments employed in the current study were performed at a vacuum better than $p \leq 2.0 \times 10^{-5}$ torr. Therefore, it could be assumed that conduction through the gas was

negligible leaving only two components of the effective thermal conductivity model: solid conduction and radiation. Consequently, the equation for effective thermal conductivity for this test was adapted from Eq. (2) and led to:

$$\boldsymbol{\lambda}^* = \boldsymbol{\lambda}_\mathbf{s}^* + \boldsymbol{\lambda}_\mathbf{r}^* \tag{9}$$

where:

$\lambda_s^* = conduction\ through\ the\ solid\ component$

$\lambda_r^* = radiation\ throughout\ the\ foam$

The radiative component will be more prominent at higher temperatures. Taking Eq. (3) and Eq. (9), the Gibson and Ashby model for effective thermal conductivity can be simplified to [23]:

$$\lambda^* = \frac{2}{3}\left(\frac{\rho^*}{\rho_s}\right)\lambda_s + 4\beta_1\sigma\bar{T}^3 texp - (K_s\frac{\rho^*}{\rho_s}t) \tag{10}$$

where:

$\rho^* = density\ of\ the\ foam$

$\rho_s = density\ of\ the\ solid$

$\lambda_s = thermal\ conductivity\ of\ the\ solid$

$\beta_1 = a\ constant\ that\ represents\ the\ emissivity\ of\ the\ surface$

$\sigma = Stefan's\ constant$

$\bar{T} = mean\ temperature\frac{T_1 + T_0}{2}$

$K_s = extinction\ coeffiecent\ of\ the\ solid$

$t = thickness\ of\ the\ foam$

The solid conduction component is a straightforward comparison of the solid conductivity and the relative density multiplied by an efficiency factor. The solid conductivity of amorphous carbon is well known although it changes drastically over the temperatures of interest [51]. Appendix A has the details of the effective thermal conductivity of amorphous carbon.

One limitation of the model was the unknown constants that are present. For example, the radiative component has β_1, a constant that represents the emissivity of the surface, and K_s, the extinction coefficient of the solid. These unknowns for this foam were not readily available in literature nor easy to measure so the first step taken was to compare the solid conductivity to the measured conductivity. Based on the Gibson and Ashby model, the testing in vacuum should be a straightforward additive relation between the solid component and the radiative component. Figure 3-2 displays the data for the guarded hot plate data from the Ultramet 100 ppi 3% foam collected for this coupon test.

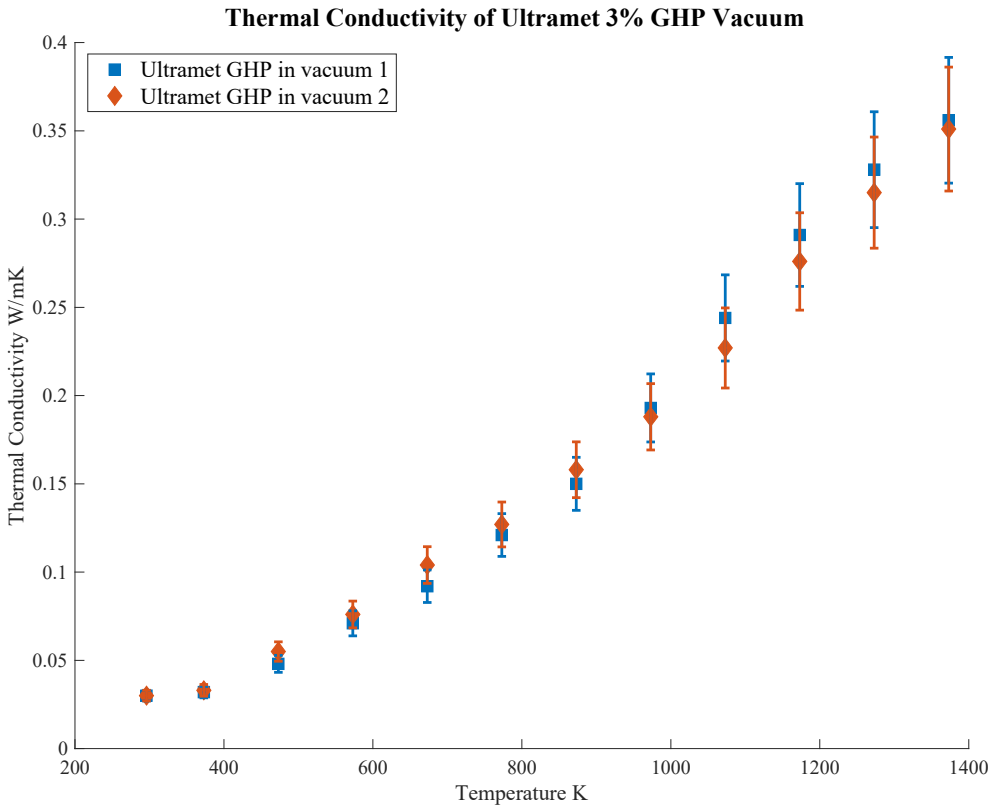

Figure 3-2 Effective thermal conductivity data from the guarded hot Plate method (GHP) in vacuum for Ultramet 100 ppi 3% with error bars. There are two sets of test data that demonstrate that effective thermal conductivity increases with temperature.

For each foam type using the guarded hot plate method, two pairs of samples were tested in separate tests. These two tests are denoted with squares and diamonds data in Figure 3-2. The reported uncertainty of this test method is up to 20%, consequently, this data is displayed in the graph as 10% error bars on either side of the samples [50]. As shown in the figure, the two samples of the Ultramet 100 ppi 3% foam were precise and fall within the error bar of each measurement.

As noted in Eq (9), for this testing, since it was completed in vacuum, the effective thermal conductivity consisted of a solid conductivity component and a radiation component. While the radiation component had a few unknowns, the solid

component could be calculated with the relative density, $\left(\frac{\rho^*}{\rho_s}\right)$, and the effective thermal conductivity of the solid, λ_s. While Gibson and Ashby did not specify that the solid conductivity was temperature dependent, the effective thermal conductivity of the amorphous carbon increases significantly with temperature. As a result, by using the temperature dependent property, the component of the solid thermal conductivity was calculated and compared to the total effective thermal conductivity. Figure 3-3 shows the test data for guarded hot plate in vacuum compared to the calculated component of the solid conductivity based on the Gibson and Ashby model.

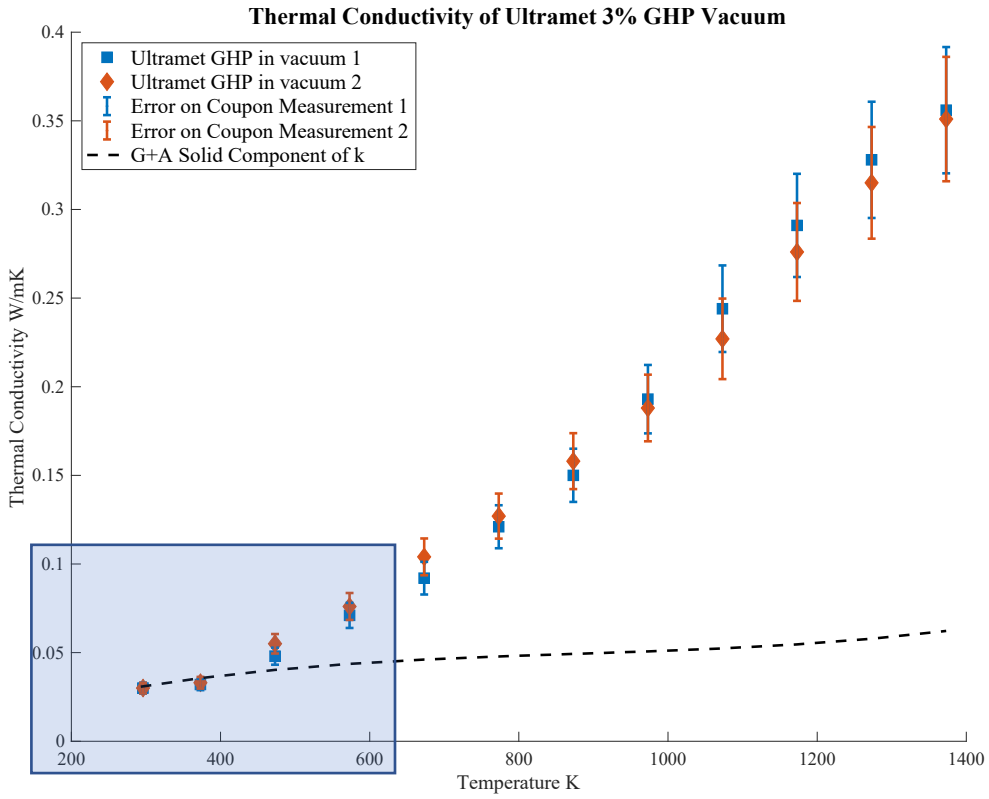

Figure 3-3 Ultramet 100 ppi 3% guarded hot plate (GHP) coupon data compared to the calculated solid component of thermal conductivity based on Gibson and Ashby model (dashed line). The solid component of thermal conductivity is the primary component of effective thermal conductivity at room temperature and then grows only slightly as temperature increases; other components are principal at the PSP perihelion temperatures. The shaded blue area is highlighted in the next figure.

As shown on the graph, the prediction based on conduction was on the mark at 300 K but significantly different than the data at higher temperatures. At lower temperatures, the effective thermal conductivity was dominated by the solid conductivity while at higher temperatures the solid conductivity was a small fraction and the thermal transport may be assumed to be dominated by the radiative component. This result was logical as the radiative component is a function of $\overline{T}^3$. The material dependent constants, β_1 and K_s, are unknown for the carbon foam and therefore the radiative component cannot be directly calculated, however if the data was consistent with the model then these constants could be determined from the data and extrapolated. The shaded area in Figure 3-3 is shown zoomed on in Figure 3-4.

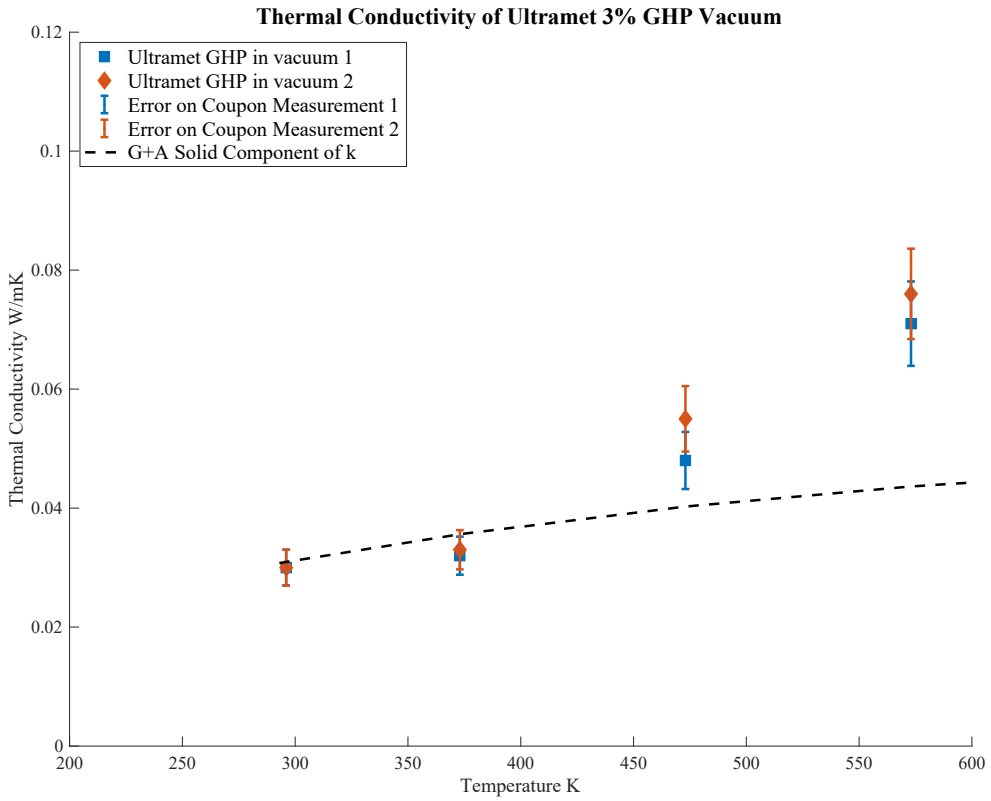

Figure 3-4 The effective thermal conductivity of the Ultramet 100 ppi 3% compared to the Gibson and Ashby model for solid conductivity around room temperature and up to 300°C. At room temperature, the main component of the effective thermal conductivity was the solid thermal conductivity component.

Since that the Gibson and Ashby model has two components, solid conduction and radiation, the conduction could be subtracted from the data in order to isolate the radiative component. Figure 3-5 has a solid line that is the calculated radiation component calculated from Eq. (10) by subtracting the solid component.

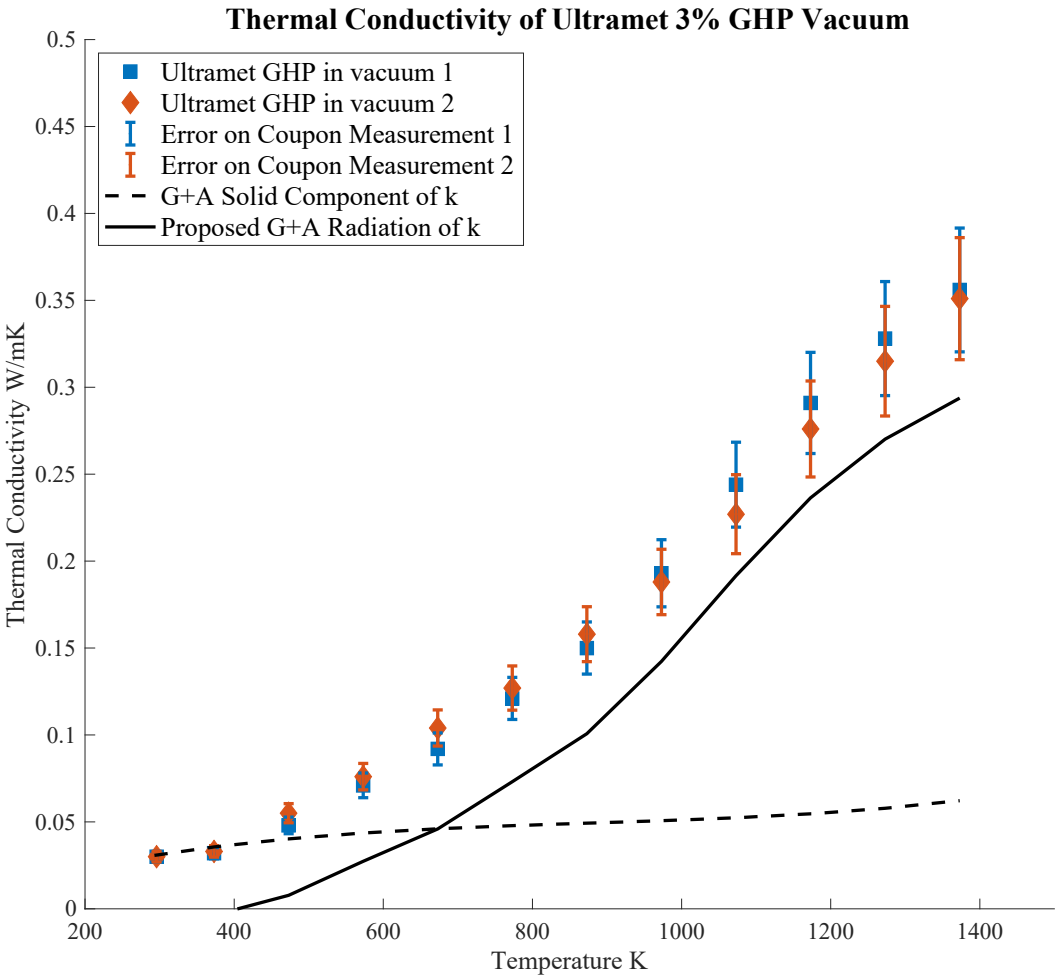

Figure 3-5 Using the guarded hot plate data (GHP), the Gibson and Ashby solid component (dashed line) was subtracted from the GHP data (blue and orange data points) to isolate the proposed radiative component from the Gibson and Ashby model (solid line).

Assuming that Eq. (10) is applicable and subtracting the solid component, λ_s^* , the radiative component is:

$$\lambda_r^* = 4\beta_1\sigma\bar{T}^3 texp - (K_s\frac{\rho^*}{\rho_s}t) \tag{11}$$

Schuetz and Glicksman suggested that the Rossland approximation could be used to determine the radiative component [52] and is:

$$\lambda_r^* = \frac{16n^2\sigma T^3}{3\beta} \tag{12}$$

where:

$n = \ refractive\ index\ of\ the\ foam$

$\sigma = Stefan - Boltzman\ constant$

$T = mean\ temperature$

$\beta = total\ extinction\ cofficient$

As shown in Eq. (11) and Eq. (12), both models assume a cubic equation with temperature for the radiative component using different model properties that are related to the material. A limitation of all of these models is the determination of these material properties. As Li and Wang noted in their study of ceramic foams, measuring these radiative properties is difficult since they are dependent on wavelength, the foam structure and the optical properties of the solid [26]. Li and Wang suggested that *n* is 1 for these porous materials [26] so β could be calculated using Eq. (12) and the test data. Figure 3-6 compares the calculated radiative models to the test values. Table 5 enumerates the values for the extinction constant used in Figure 3-6.

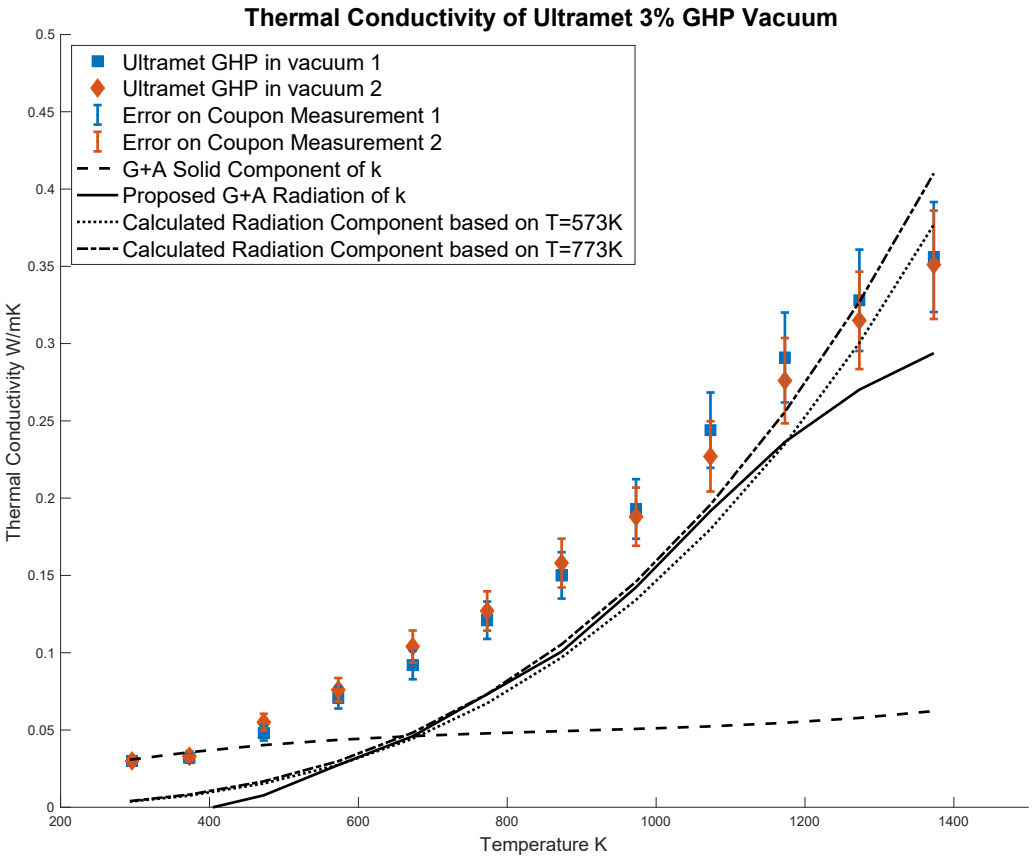

Figure 3-6 The radiative component calculated by subtracting the solid thermal conductivity from the data (black solid line) is compared to the radiative component calculated based on the Rossland equation (dotted and dot dashed lines). The dotted line used an extinction coefficient calculated from the value at 573 K and the dot dashed line used an extinction coefficient calculated from the value at 773 K.

Table 5 Calculated extinction coefficients based on the Rossland equation using the guarded hot plate data

	Calculated from value @ T= 573K	Calculated from value @ T= 773K
Extinction Coefficient, β	2076	1908

In Figure 3-6, the solid line (the solid conductivity subtracted from the guarded hot plate data) was compared to the dotted and dot-dashed lines which are both radiative

component models using two different extinction coefficients. Interestingly, the models, no matter the extinction coefficient, followed the test data from about 500 K to about 1100 K. However, above 1110 K the model diverged from the test data. Above 1400 K, the model for the radiation component alone was above the measured value for the effective thermal conductivity which has solid and radiative components. For this study, temperatures above 1600 K were of interest so the discrepancy between the model and the test data at these higher temperatures were important.

3.3.1. Thermal Diffusivity Testing

The thermal diffusivity method was also used to determine the effective thermal conductivity of all samples. Two types of thermal diffusivity tests were performed: ASTM E1461 and 3P. Both tests are described below. The basic approach to this method was to measure the thermal diffusivity, α, and the density of a sample, and then calculate the effective thermal conductivity, λ. The equation for this approach is Eq. (13). This testing was performed at TPRL, Inc in West Lafayette, IN [53]. Due to the differences between the candidate foams, different methods for determining effective thermal conductivity needed to be used; four of the samples were tested using the laser flash method, ASTM E1461, while the other two were tested using the 3P method. The differences between the testing were driven by the foams themselves. The 3% density open pore foams, ERG 100 ppi and Ultramet 100 ppi, were too porous to get successful infrared (IR) measurements and ASTM E1461 relies on IR for temperature measurements [53]. Therefore, the 3P method needed to be used for these materials.

$$\lambda = ac_p d \quad (13)$$

Where:

$a = the\ measured\ thermal\ diffusivity\ of\ the\ sample$

$c_p = the\ specific\ heat\ of\ the\ sample$

$d = density\ of\ the\ sample$

All testing was performed in a low vacuum ($p \leq 1.0 \times 10^{-2}$ torr) or in an argon cover gas (760 torr). Both these environments were less like the vacuum of space than the environment used for the guarded hot plate method, but given the temperatures desired for this testing, the vacuum of space was difficult to achieve in a test lab on Earth. Since these samples were carbon foam, any presence of oxygen introduced the possibility of oxidation and therefore mass loss in the samples. Having higher temperatures on the samples generally meant that it was difficult to maintain a good vacuum. Additionally, the objective of this testing was to measure the steady-state effective thermal conductivity which means that the sample must be kept at high temperatures for long periods of time, further exacerbating these issues. As the vacuum of the testing degrades, oxidation and convection were introduced into the test. Testing in argon limited the amount of mass loss from oxidation on the samples at high temperatures but introduced the effects of convection and conduction in the gas into the effective thermal conductivity measurements. Testing in a $p \leq 1.0 \times 10^{-2}$ torr vacuum limited convection but introduced the mass loss due to oxidation into the effective thermal conductivity measurements. By testing in both environments and

comparing these measurements with the better vacuum measurements discussed in the previous section, the real effective thermal conductivity of these foams could be assessed, and therefore the performance of each material at the Sun could be understood.

For the thermal diffusivity methods, the density of each sample was calculated from the masses and the measurement of the dimensions of the samples. The samples that were tested in vacuum were also checked for mass loss after testing. The mass loss of these samples was seen to be from -5% to -15%. Gembarovic and Freeman note that based on mass loss observed for the material in vacuum, there was no concern of mass loss in deep space or in an inert atmosphere concluding that the 15% mass loss was test driven, by the atmosphere present or the handling, as opposed to a phenomenon that would be present in the atmosphere of space [53]. The samples were very fragile and therefore they were difficult to handle which could have resulted in small pieces breaking off during handling. Another reason why the density measurements might vary was that the material could be inhomogeneous due to processing and manufacturing variability. The accuracy of the density measurement was a variable in the accuracy of the effective thermal conductivity value since it was a basis used for the calculation in the thermal diffusivity methods.

The specific heat, c_p, is a material property that is defined as the energy required to raise the temperature of a unit mass of a substance by one degree [54]. In this case, the value being measured was the specific heat at constant pressure. Due to the difficulties in testing these materials at higher temperatures, the specific heat for each sample was

measured from room temperature to 400°C using a Perkin-Elmer Model DSC-2 with a sapphire reference material using ASTM 1269. Using the mass of the sample, the mass of the sapphire and the differential power required to heat the samples, the specific heat of each foam was calculated. The graph of the calculated specific heat capacity values and their relation to the specific heat of carbon is shown in Figure 3-7. As shown in the graph, the foams' specific heat was in line with the specific heat of carbon over this temperature range, and therefore, above 400°C, the specific heat of all foam samples was assumed to be that of carbon.

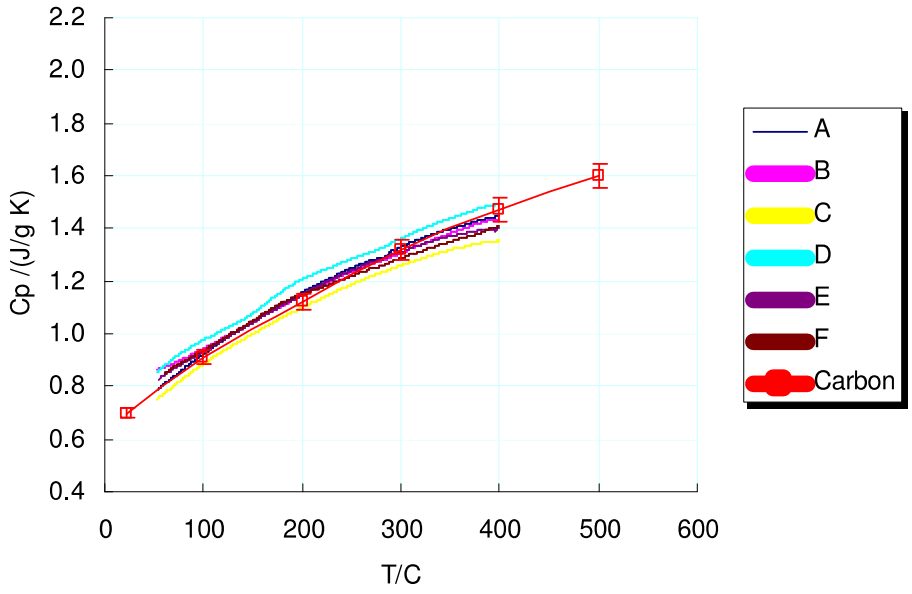

Figure 3-7 Specific heat of all the carbon foams related to the specific heat of carbon [53]. The carbon foams were shown to be represented by the specific heat of carbon so the specific heat of carbon was used to calculate the effective thermal conductivity using the thermal diffusivity (TD) methods.

3.3.1.1. ASTM E1461

The laser flash method, ASTM E1461, which was used for less porous foam samples, used short laser bursts to heat one side of the sample and an IR camera measured the

temperature on the back side thereby measuring the diffusivity of that impulse heat through the sample. A depiction of this set up from ASTM E1461 is Figure 3-8.

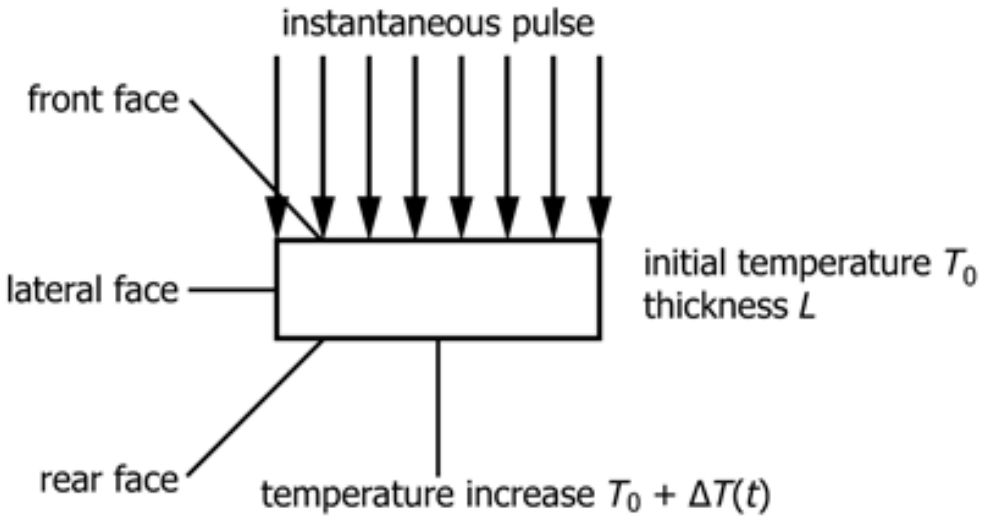

Figure 3-8 For ASTM E1461, laser flash diffusivity measurement, a pulse was applied on one side of the sample and a measurement of temperature was taken on the other face [55].

The ASTM E1461 test assumed an ideal case of thermal diffusivity. The model for the test assumed an adiabatic material that was initially at a constant temperature. As shown in Figure 3-8, a sample with an initial thickness, T_0, was exposed to an instantaneous pulse on one side and the rear surface is measured for a temperature increase due to this short pulse. This test set up was idealized to present one dimensional heat flow and therefore had a variety of assumptions built into the calculation, including homogeneity and isotropy of the material and no edge losses.

For homogeneity and isotropy, the test method noted that "this test method is applicable to the measurements performed on essentially fully dense (preferably, but low porosity would be acceptable), homogeneous, and isotropic solid materials that are opaque to the applied energy pulse." [55]. The candidate materials for this testing were

not fully dense, however four of the six were opaque to the applied energy pulse. This opacity was deemed acceptable for this test method because the energy transfer method met the intent of the test specification. However, for the two candidate foams, Ultramet 100 ppi 3% and ERG 100ppi 3%, which did not have the proper opacity, an alternative test method was used, the 3P method.

3.3.1.2. The 3P Method

The 3P method was developed by TPRL specifically to test porous materials at higher temperatures and was well suited for this project. The 3P method used a uniform heat flux on one side of the sample and then measured the surface temperature on the other side of the sample with thermocouples. Like the other samples tested at TPRL, testing of each porous sample was performed under vacuum at $p \leq 1.0 \text{ x } 10^{-2}$ torr and under argon at atmospheric pressure 760 torr separately [53]. This method also relied on specific heat values that were measured up to 400°C using ASTM E1269 and a sapphire reference material [53].

The test set up for the 3P method is shown in Figure 3-9. The basic design replicated the one-dimensional heat flow model from ASTM 1461 with metal plates to block the light heat source and provided a uniform heating impulse. The samples used were 5 cm in diameter and 1 cm in thickness. They were sandwiched between thin Saffil insulation and thin metal plates on each side. These plates presented a uniform heating surface for the samples and prevented the light from penetrating the porosity. The plates function as hot plates defining the temperature of one side of the sample. These plates differ from the facesheets on the PSP TPS as they have a lower emissivity, but this

was mitigated by the presence of Saffil insulation which had a similar emissivity to carbon fiber. This test set up was not attempting to replicate the sandwich panel. Instead, the test set up was using known materials to define the temperature with a uniform surface. As noted in the figure, temperature was measured using three thermocouples distributed in the sample at defined distances from the light source. The relative distance between the thermocouples in the sample factor into the measurement of diffusivity. Measurement time varied from 60 to 450 seconds depending on the sample thickness and the thermal diffusivity of the material [56].

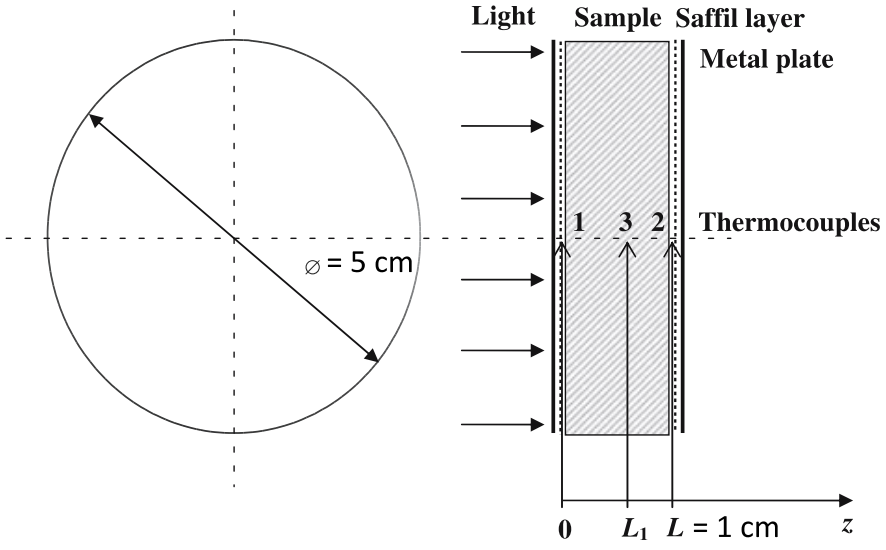

Figure 3-9 On the left is a top-down view of the sample. On the right is an edge-on view of the test set up. For 3P Method sample set up, thermocouples were placed at position 1, 2 and 3 in the sample and a light was applied to a metal plate on one side. This test set up was used on the high porosity materials that were not opaque to an energy pulse supplied by a bulb mounted in a parabolic reflector, adapted from [56].

The samples were mounted in a vacuum chamber with quartz windows for testing so that the heat source, a 600 W quartz-iodide tungsten element bulb mounted in an

aluminum parabolic reflector, could be outside the chamber [53]. The thermocouples were used to determine the temperature at points 1, 2 and 3 in the thickness of the sample. These temperatures are used with the damped heat wave algorithm (DHW) to calculate the temperature within the sample instead of the finite difference scheme calculated from the differential equation for a one-dimensional heat conduction problem. The DHW algorithm divided the finite homogeneous sample into equal thickness slices. These pieces were represented as perfect conductors with the same heat capacity and a thermal resistance of the thickness divided by the effective thermal conductivity of the sample. The damped heat wave was the propagation of the heat between these pieces due to the temperature difference between the pieces. The wave bounces back and forth between the boundaries, and the temperature of each piece changed after a full wave cycle. The least-squares method was used to solve the equation that results from this algorithm [56].

Given that the 3P method was not standard, TPRL validated its results by comparing results to other methods using known materials however this validation only was done to 200°C which is considerably lower than the temperatures of the PSP TPS [56]. This potential source of error was why there were multiple test methods used and these methods were compared.

3.4. Thermal Diffusivity Effective Thermal Conductivity of the Ultramet 100 ppi 3% Foam

Adding the data from the thermal diffusivity method to Figure 3-2 gives Figure 3-10 which displays all the coupon data for the Ultramet 3% 100 ppi testing. The thermal

diffusivity testing was done in both vacuum and in an argon cover gas. With the presence of the argon, the effective thermal conductivity is again Eq (3). These numbers were not directly comparable since three of the data points were taken in vacuum and one of them was taken with an Argon cover gas, but it was informative to understand the effective thermal conductivity and the potential effects of conduction through the argon gas.

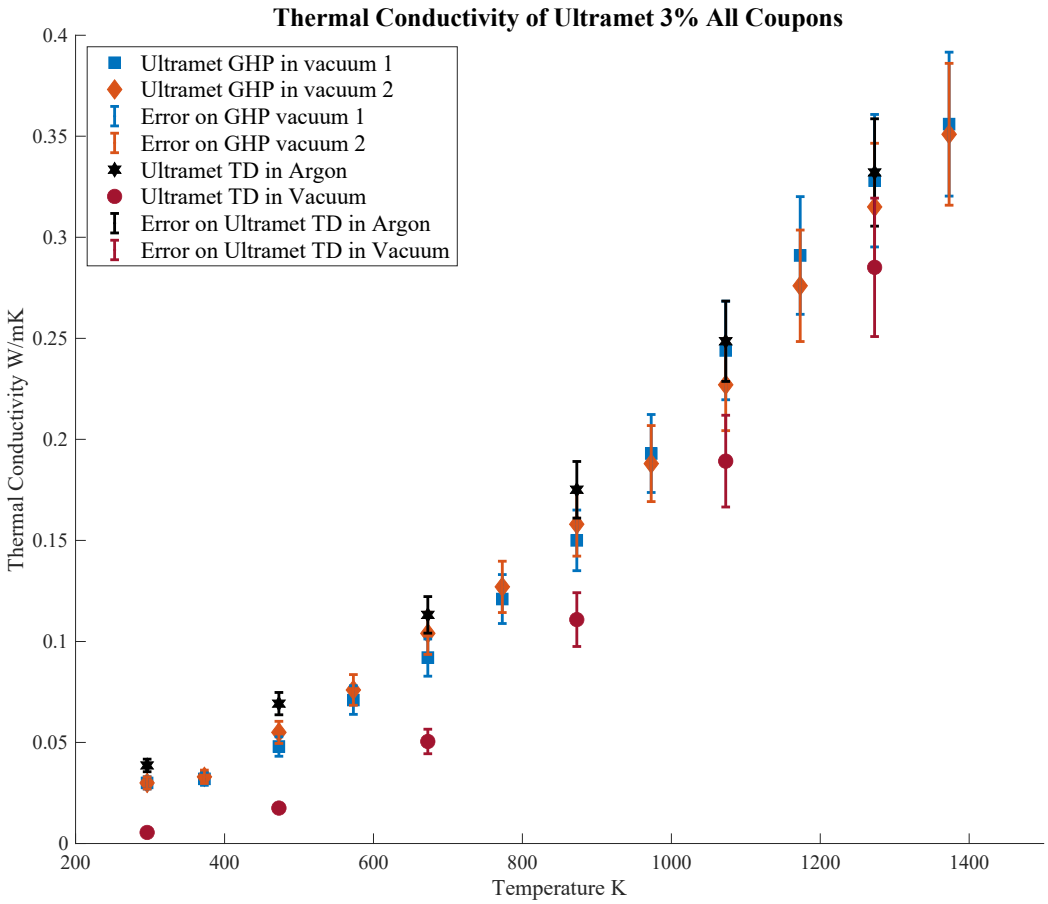

Figure 3-10 All coupon data for the Ultramet 100 ppi 3% foam including from guarded hot plate (GHP) method, the blue and orange markers, and thermal diffusivity (TD) methods, the red and black markers.

Figure 3-10 shows that the trends in the effective thermal conductivity are the same for all sets of data. As expected, the red, magenta and blue data points, which

were the vacuum data, fall below the black data points, which was the argon data. As predicted by Eq (3), the effective thermal conductivity in argon should be the addition of the effective thermal conductivity in vacuum plus the conductivity in argon that fills the pores. At higher temperatures, as shown in Figure 3-10, the data began to coalesce particularly when taking into account the error bars. The fact that the errors bars increased with temperature could be attributed to the difficulty associated with taking these measurements at temperature as well as the error bars being a percentage of the overall effective thermal conductivity which increases with temperature.

Looking at the red and black data points on the graph, which were taken using the 3P thermal diffusivity method, a few observations could be made. First, the red data points representing the vacuum effective thermal conductivity measured using the thermal diffusivity method of the Ultramet 100 ppi 3% foam, were below the calculated effective thermal conductivity of the solid per the Gibson and Ashby model. Recall from Figure 3-5 that the solid component of the Gibson and Ashby model, represented by a dashed line, equaled the data points for the Guarded Hot Plate method at low temperatures. The resultant thermal diffusivity measurement of effective thermal conductivity was well below this solid conductivity at room temperature and lower temperatures. Comparing this data to the Gibson and Ashby model, it indicated that the guarded hot plate method was more accurate at least at the lower temperatures since the solid component should play a dominate role in the effective thermal conductivity at these temperatures.

Despite the limitations of the 3P coupon test, this method was used to measure the same foam in both argon and in vacuum. Part of the Gibson and Ashby model is the thermal conductivity of the gas if it is present. As noted in Eq. (3), the component of effective thermal conductivity that comes from the gas is the thermal conductivity of that gas multiplied by the volume that is not taken up by the foam solid. Subtracting the data from the 3P coupon data taken in vacuum from that taken in argon gave the heat transfer through the argon as shown in Figure 3-11. The red line, the calculated component of the argon gas conduction for this foam, was compared to the blue dots, the difference between the 3P data for the Ultramet 100 ppi 3% foam in vacuum and in argon. The data points and the model calculation should be comparable but the fact that they diverged means that convection or a source of test set up error effected this direct comparison.

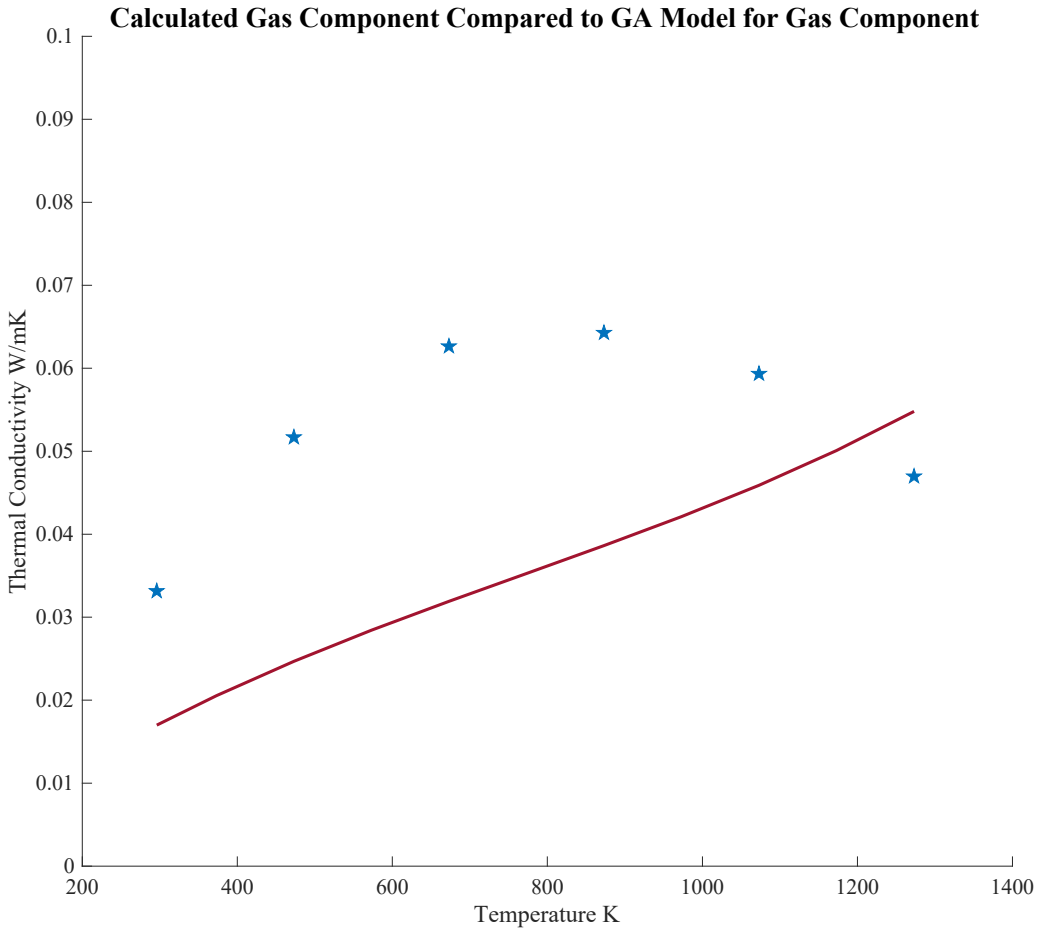

Figure 3-11 The argon component of the effective thermal conductivity calculated by subtracting the data taken in vacuum from the data taken in Argon. Blue dots are the in-vacuum data points subtracted from the argon data points for Ultramet 100 ppi 3% using the thermal diffusivity test method. The red line was the calculated component of the gas component, argon, of the effective thermal conductivity of the foam. These numbers should be comparable but diverged in shape and magnitude.

The coupon test data taken using the guarded hot plate and thermal diffusivity methods was compared to the Gibson and Ashby model for the effective thermal conductivity of foams. Around room temperature, the solid component of the conductivity represented the main component of the Ultramet 100 ppi 3% conductivity; however, the test data diverged from the data as the temperatures increased and the radiation component played a larger role in the effective thermal conductivity. The

Gibson and Ashby models for the radiative component and the gas conduction component did not directly match test data. The disparity could be explained by inaccuracies in the model or issues with the test set up. The next section discusses potential inaccuracies in the test set ups.

3.4.1. Discussion of Comparison of Test Methods

The difficulty of accurately measuring samples at high environmental temperatures affected the accuracy of all coupon testing types. For the flash diffusivity method, ASTM 1461, the accuracy of the temperature measurement using an IR camera at 1000°C depended on the accuracy and knowledge of the emissivity of the material at this temperature. The optical properties were used to directly calculate the temperature of the sample.

Thermocouple measurement methods incorporate other errors that also lead to inaccuracies in temperature values. Thermocouples have different accuracy ranges depending on the temperatures that are being measured. Measuring the temperature of foam can be difficult due to the lack of surface area. When attaching a thermocouple to foam, it can be difficult to know if the thermocouple is attached to a foam surface. Additionally, the thermocouple is often attached using adhesive. Adhesives that can survive these temperatures tend to be ceramics that are insulative and therefore affect the measurement.

In addition to the inaccuracies of the testing methods, the test environments have limitations. For these coupon measurements, testing was done in a variety of levels of vacuum and with an argon cover gas. None of these atmospheres represent the exact

environment of interest, the vacuum of space. All options have more convection and oxidation present than will be present in space. For argon, the presence of both convection and conduction in the gas needs to be accounted for, but the cover gas did protect the test specimens from oxidation to a certain degree. Without the cover gas, oxidation was more prevalent, and the coupons can change chemically and degrade which would affect the measurements.

All coupon samples are smaller than those that were used in the subscale testing. The combination of smaller-sized samples and square coupons means the edge effects on the guarded hot plate coupons is higher than in some of the other test results discussed. The guarded hot plate method must and does take edge effects into account in calculating the effective thermal conductivity, while methods like the 3P method negate edge effects by placing the measurement devices inside the coupons.

Since the ultimate goal of this testing was to determine the behavior of the foam in space at high temperature, the limitations discussed here mean that the precision and accuracy of the results from coupon testing may be affected. However, taken as a whole, all of these tests allowed us to develop an understanding of the thermal performance of the carbon foams. These methods are useful to compare and assess factors (e.g. density, relative density, foam structure, thickness, shape and size) that can affect the effective thermal conductivity of the candidate foams.

3.5. Discussion of Effective Thermal Conductivity: Ultramet 100 ppi 3% Foam

The preceding section used the Ultramet 100 ppi 3% foam as an example to look at the thermal coupon data in relation to the model developed by Gibson and Ashby. A

close look at this data reveals that the model has limitations, particularly at the high temperatures of interest to this application. The radiative component was shown to be more complex than the Gibson and Ashby model suggests and conduction through the gas was shown to be of a lower value than suggested by the model. The differences between the model and the coupon data cannot be fully explained as testing artifacts; limits in applying the Gibson and Ashby model to the carbon foams much also be considered. Interestingly, the coupon data converges within the error bounds at the higher temperatures. This convergence suggests that while the data diverges from the model predictions at elevated temperatures, the value of effective thermal conductivity for the foam at these temperatures is most likely being captured by the coupon testing. This fact shows the importance of the coupon testing, particularly at higher temperatures. The inconsistency between the test data and the Gibson and Ashby model at these temperatures is not surprising given that the model was developed for insulative foams used for refrigeration. For these refrigeration foams, conduction through the gas is the dominate component of effective thermal conductivity while here the dominate component is the radiative element. While there are limitations to this coupon testing and the model, the coupon data has been used to explore the effects of structure and density on the effective thermal conductivity of the foam which will be described in the following sections.

3.6. Discussion of the Influence of Density on Effective Thermal Conductivity

For this dissertation, the set of Grafoam foams had three different relative densities, 2%, 5%, and 10%, and had a mix of open and closed cells. These foams were made using

the same processing and therefore had the same basic materials and structure. The influence of relative density on effective thermal conductivity was investigated by examining the coupon results of the various foams. The individual foam coupon results are compiled in Appendix B. For clarity of comparison, Figure 3-12 focuses the vacuum coupon for Grafoam FPA-02, FPA-05, and FPA-10. As a reminder, the numbers represented in the names of the foams represent the relative density of each foam.

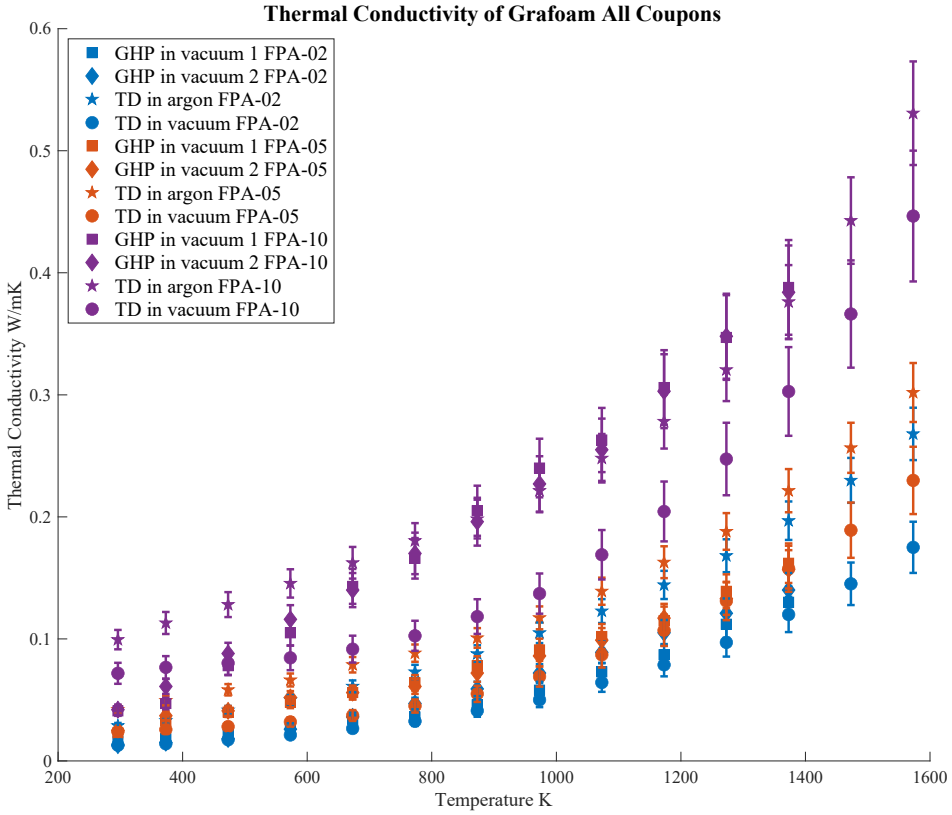

Figure 3-12 Vacuum data for all Grafoam coupons is shown. The Grafoam foams had the same structure and material but varying relative densities. The lowest relative density, FPA-02, are the blue data points, the medium density, FPA-05, are the orange data points, and the highest density, FPA-10, are the purple data points. The effective thermal conductivity increased with increasing relative density.

The general trend of the effective thermal conductivity rising with relative density held true for all coupons as shown in Figure 3-12. The influence of the radiative

component increases with increasing temperature and the relationship between the radiative component of the effective thermal conductivity and the relative density was more complex than suggested by the Gibson and Ashby model. However, as demonstrated by the data, closer to room temperature the solid component of the conductivity dominated. According to Gibson and Ashby, this solid component has a direct comparison to the relative density. Taking Eq. (9) and Eq. (10), the solid component of the thermal conductivity according the Gibson and Ashby model is:

$$\lambda_s{}^* = \frac{2}{3}\left(\frac{\rho^*}{\rho_s}\right)\lambda_s \tag{14}$$

where:

$\lambda_s^* = conduction\ through\ the\ solid\ component$ of the foam

$\rho^* = density\ of\ the\ foam$

$\rho_s = density\ of\ the\ solid$

$\lambda_s = conductivity\ of\ the\ solid$

Using the same approach as described earlier for Ultramet 100 ppi 3% foam, Figure 3-13 displays the vacuum data with the conduction through the solid, using the 2/3 efficiency factor suggested by Gibson and Ashby, shown with dashed lines.

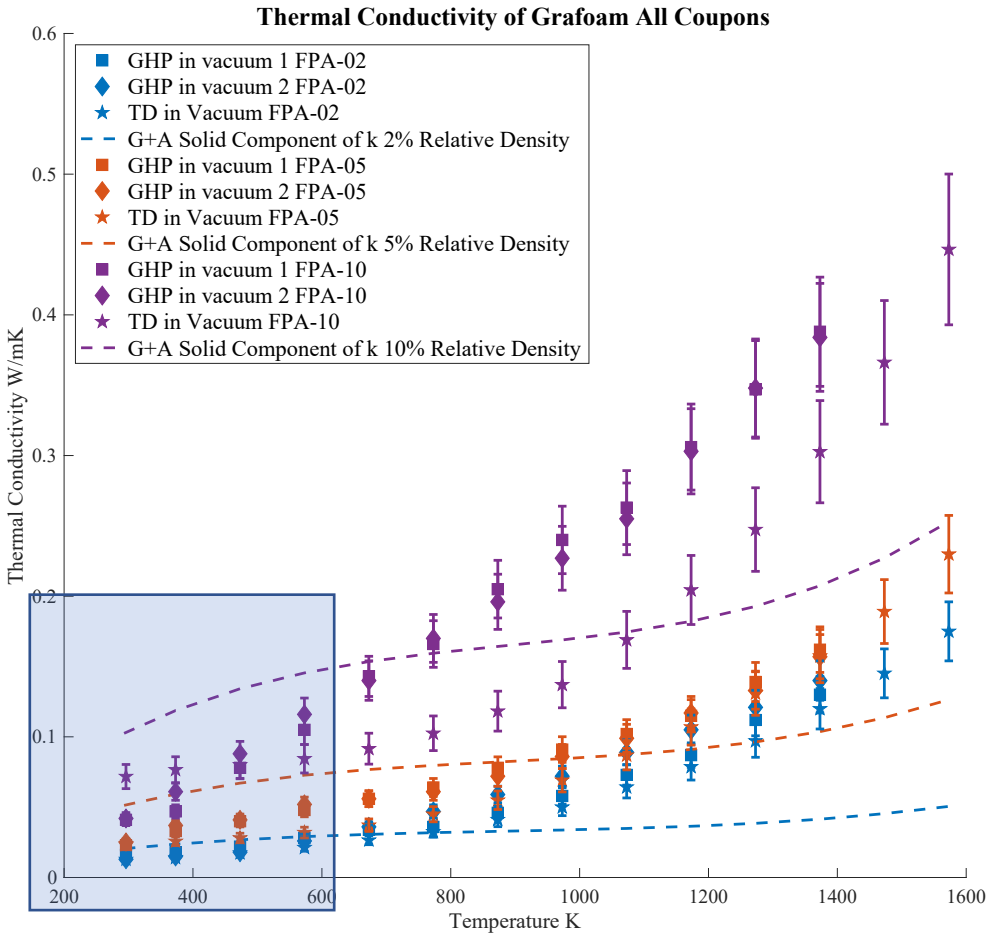

Figure 3-13 Summary of all vacuum Grafoam coupon data with dashed lines indicating the conductivity through the solid per the Gibson and Ashby model plotted. The dashed lines representing the Gibson and Ashby solid component exceeded the measured data points at lower temperatures. The shaded blue area is highlighted in the next figure.

The solid component calculated from the Gibson and Ashby model was larger than the test data suggesting that the Gibson and Ashby model had the wrong scaling component for this foam as shown in the values around room temperature in Figure 3-13. Figure 3-14 is focused in on the temperatures around room temperature to separate the solid component of the thermal conductivity from the radiative component

that dominated at higher temperatures. Figure 3-14 demonstrates that the 2/3 efficiency factor, suggested by Gibson and Ashby, was not appropriate for this set of foams since the model overestimates effective thermal conductivity. Figure 3-15 is a mirror of Figure 3-14 but using a variety of efficiency factors for calculating the solid component of the thermal conductivity.

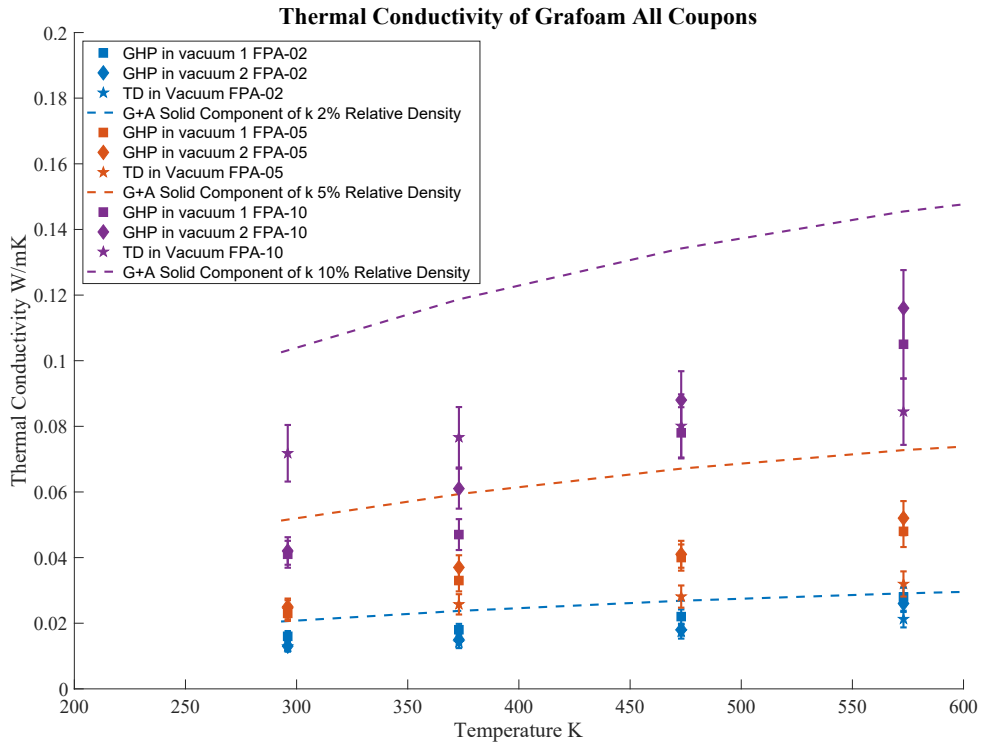

Figure 3-14 This figure is the data points and calculated model lines from Figure 3-13 from room temperature to 300°C. The dashed lines representing the Gibson and Ashby solid component exceeded the measured data points at lower temperatures which suggested that the efficiency factor of 2/3, which is part of the Gibson and Ashby solid component model, was not appropriate for this foam.

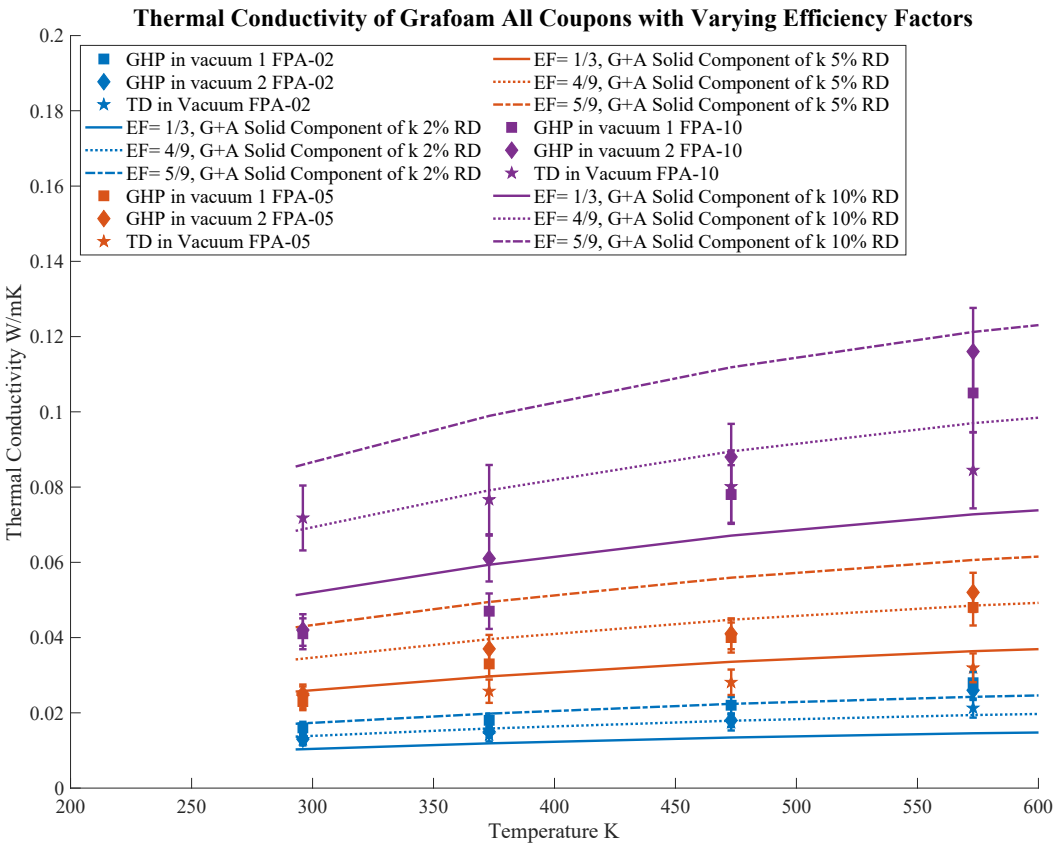

Figure 3-15 The Grafoam coupon data graphed with the Gibson and Ashby proposed solid component with varying efficiency factors. The solid line represents an efficiency factor of 1/3; the dotted line represents an efficiency factor of 4/9; and the dot/dashed line represents an efficiency factor of 5/9.

At room temperature, the solid component composed most of the effective thermal conductivity. By using a variety of efficiency factor as shown in Figure 3-15, the calculated Gibson and Ashby solid component fell within the coupon data for all of the foams. Based on these results, the relative density did appear to be an important component of the effective thermal conductivity as multiplied by the thermal conductivity of the solid. However, the efficiency factor on this solid component was lower than suggested by Gibson and Ashby. This difference was driven by the structure of the foam with a mixture of open and closed cells. This structure was divergent from

the idealized foam upon which Gibson and Ashby based their model and the foams studied in this dissertation offer an opportunity to understand the influence of structure on effective thermal conductivity which will be examined in the next section.

3.7. Discussion of the Influence of Structure on Effective Thermal Conductivity

The Calcarb Foam and the Grafoam FPA-10 were both 10% carbon relative density foam; however, Calcarb foam was a fibrous-packed board while the Grafoam FPA-10 was a periodic mixed open and closed cell foam. Comparing the coupon results from these two foams allowed one to isolate structure from relative density. Figure 3-16 is a effective thermal conductivity graph of the Grafoam FPA-10 and Calcarb coupons in vacuum and Figure 3-17 shows pictures of these foam structures.

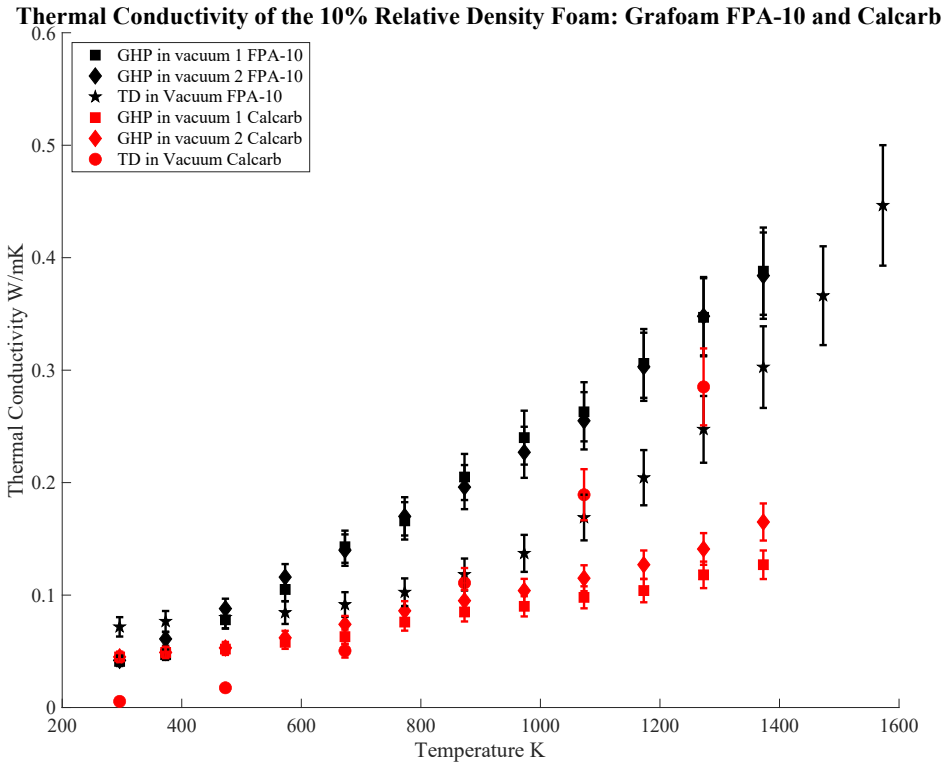

Figure 3-16 Coupon data for the Grafoam FPA-10 (in black) and the Calcarb (in red) in vacuum per the guarded hot plate (GHP) method and the thermal diffusivity (TD) methods are displayed. The carbon foams were the same relative density but had a different structure. The Calcarb had a lower effective thermal conductivity over temperature suggesting that the structure type influences effective thermal conductivity. Figure 3-17 is images of these structures.

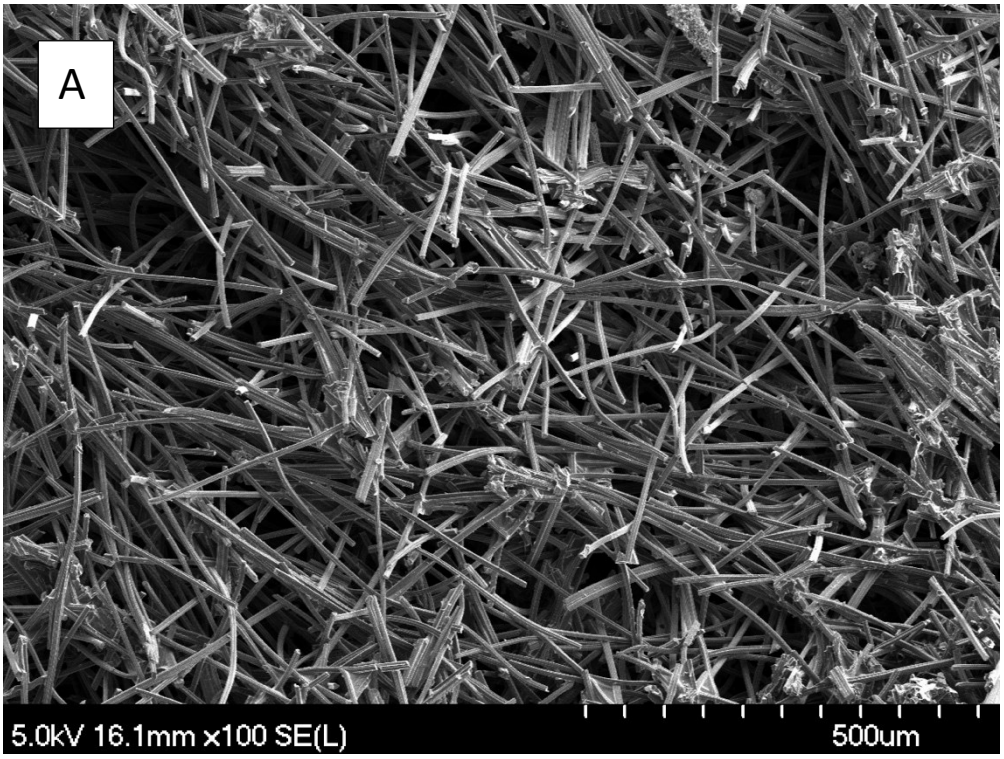
A
5.0kV 16.1mm x100 SE(L)
500um

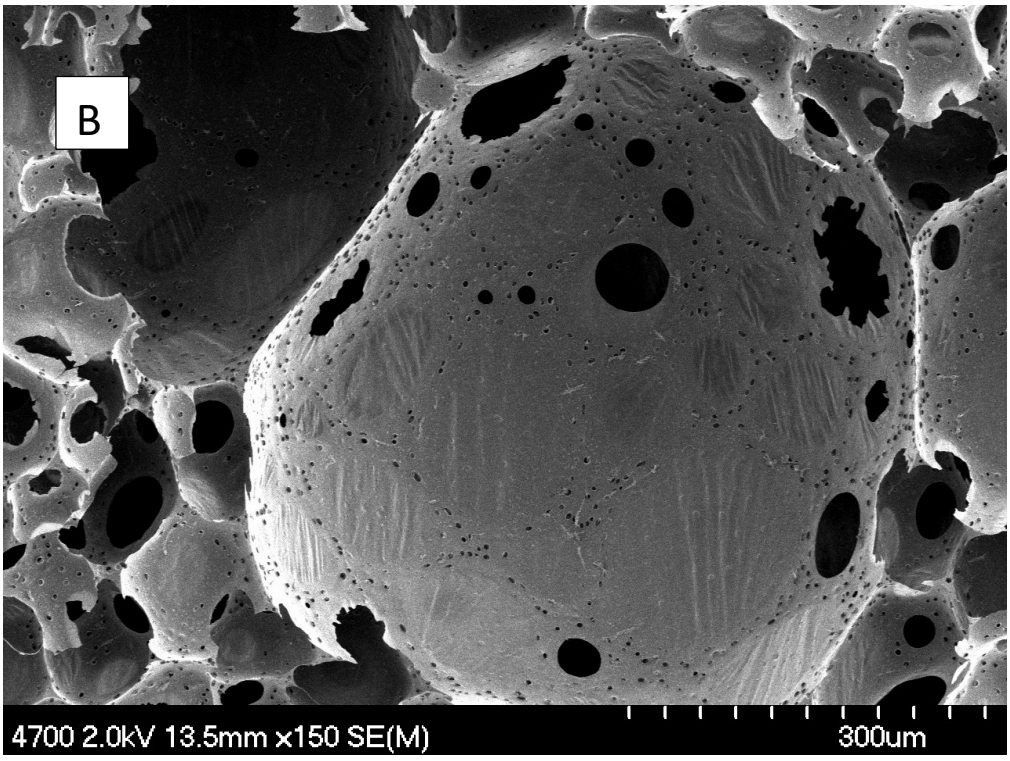
B
4700 2.0kV 13.5mm x150 SE(M)
300um

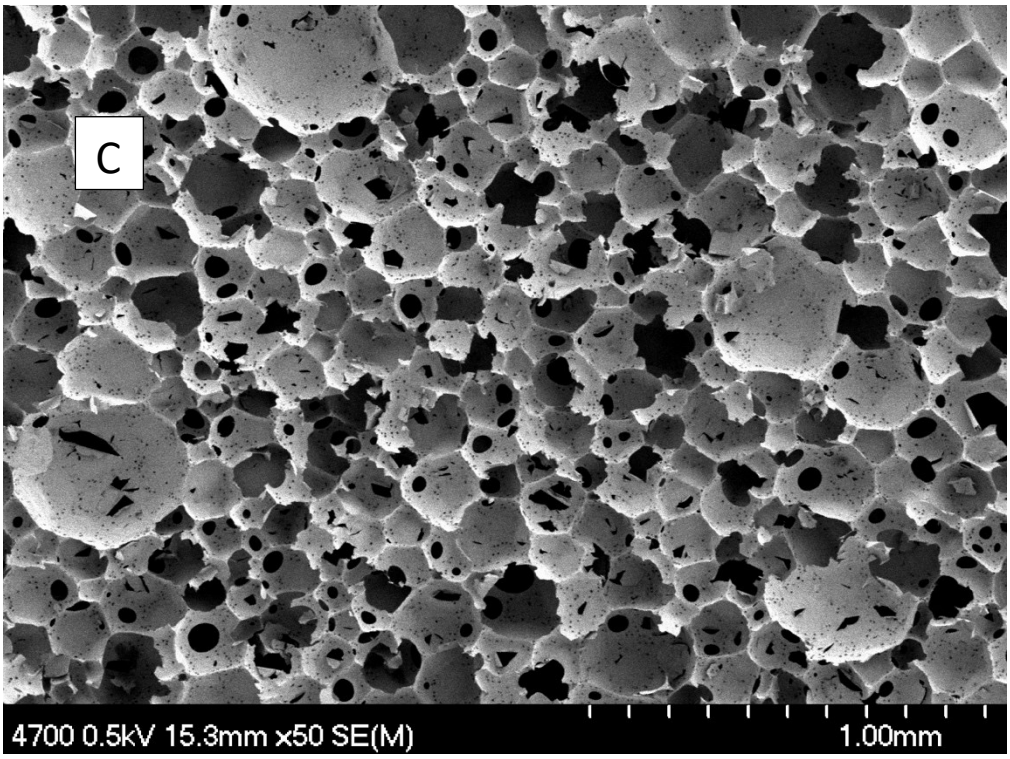

Figure 3-17 Images of the Calcarb and Grafoam structure (Courtesy of Ryan Deacon). A: Calcarb B: Grafoam C: Grafoam at a different scale.

The results from the testing were consistent at room temperature where the effective thermal conductivity was primarily the conduction of the solid. The effective thermal conductivity data of Calcarb using the thermal diffusivity method was an outlier around in this temperature range. The accuracy of the thermal diffusivity method translating to the effective thermal conductivity correctly was dependent on the homogeneity of the foam in all directions. The Calcarb, as a packed fiber board, was the foam that most diverged from this ideal so the lower value was most likely due to the nature of the test as opposed to the inherit material property. As the temperature increased, the foams diverged in behavior. The Calcarb data was consistently below the Grafoam FPA-10 at higher temperatures showing that the thermal transport through foams with the same density and base material diverged at higher temperatures based

on structure. This geometry difference drove differences in radiative surface thereby effecting the effective thermal conductivity at high temperatures.

Using the Gibson and Ashby model, it has been shown that the effective thermal conductivity behavior near room temperature was dominated by the thermal conductivity in the solid while the radiative component dominated at higher temperatures. This observation was consistent with the solid component of thermal conductivity being dependent only on the relative density and the thermal conductivity of the solid. The radiative component was more complicated and the behavior of divergence in effective thermal conductivity for two foams that are the same material and density suggested that structure of the material plays an important role in radiative transport.

3.8. Subscale Testing Methodology

The key limitations, such as size scale and flight like boundary conditions, of coupon level testing meant that further testing needed to be done to understand the behavior of the system at the expected operational temperatures. Testing materials on different scales illuminated the dichotomy between the limitations of the test themselves and the limitations of the material. Additionally, a large part of the success of making the PSP TPS was developing manufacturing techniques that could be used to build these subscale pieces. A critical component of figuring out these techniques was building pieces of various sizes and developing the manufacturing processes that were needed for full scale unit processing. By building pieces at multiple scales, the ability to manufacture, process and repair these pieces could be worked out and perfected.

While testing at maximum flight-like temperatures (1400°C) and at the full scale (2.4 meters) was explored, it was determined to be cost and time prohibitive. All available test facilities capable of accommodating the full-scale TPS were designed for transient testing to support designs and components intended for reentry. Therefore, all test facility options at this scale would have a significant amount of oxygen present, which result in non-optimal test conditions. Full-scale testing was explored as part of the larger development effort, particularly at Armstrong Flight Research Center (AFRC) and Johnson Space Center (JSC), but ultimately it was cost and time prohibitive to retrofit these facilities. Additionally, based on exploration testing, it was determined that oxidation would damage the articles such that they would be unusable as flight articles.

Given the limitations on full-scale testing, a major subscale test program was undertaken. Specifically, subscale thermal test methods were developed at JSC, Oak Ridge National Laboratory (ORNL), and Johns Hopkins University Applied Physics Laboratory (JHUAPL). The testing at ORNL represented a major part of this dissertation because this method was used to understand effective thermal conductivity of the carbon foam and was compared to the coupon level testing discussed above.

3.8.1. Oak Ridge Testing Effective Thermal Conductivity

The ORNL test facility was used for a few different thermal tests for PSP. Originally it was used to measure the optical properties of the alumina-based coating that was doped with boron nitride and developed for PSP. However, it also presented an opportunity to take subscale effective thermal conductivity measurements of the carbon foam. JHUAPL and ORNL collaborated to design the test set up with members of

both organizations on site at ORNL to perform testing. The test setup consisted of a specially designed vacuum box that was water cooled. This vacuum box was placed under the ORNL 300,000 W plasma lamp which could expose the unit for hours [57]. Thermocouples (TCs) and an infrared (IR) camera were used to measure the temperature at defined depths throughout the foam. Throughout testing, lamp power, which defined the heat flux on the sample, the vacuum level and the cover gas pressure, if present, were precisely controlled and systematically varied.

There were five phases of testing at ORNL on carbon foam, carbon felt, and the alumina coating. The rounds focused on carbon foam testing are highlighted in Table 6.

Table 6 ORNL test matrix

Test Round	**Measurements**	**Foam**	**Pressures**	**Temps**
First Round	TCs, IR camera	Ultramet 100 ppi 3% ERG 100 ppi 3%	$p \leq 1.0 \text{ x } 10^{-5}$ torr	200°C 500°C 1000°C 1500°C
Second Round	TCs	Ultramet 100 ppi 3%	$p \leq 1.0 \text{ x } 10^{-6}$ torr $p \leq 1.0 \text{ x } 10^{-3}$ torr $p \leq 0.5$ torr $p \leq 1.5$ torr	200°C 500°C 1000°C 1500°C

As shown in the table, Ultramet 100 ppi 3% foam and ERG 100 ppi 3% foam were tested at ORNL over multiple temperatures. The goal of the first round of testing was to provide a comparison to the effective thermal conductivity of the foam in the coupon testing. For the second round, testing was conducted at a variety of pressures for the Ultramet 100 ppi 3% foam, theorizing that this data could be used to determine the effects of pressure on the effective thermal conductivity results. The first and second round of testing used the same test set up but had slightly different instrumentation and sample sizes.

Figure 3-18 provides a picture of the test setup for both rounds of testing. The structure in the left side of the picture was the vacuum system for the vacuum box which was the black structure on the right side of the picture. The vacuum system had a roughing pump and a turbomolecular pump. The black vacuum box containing the sample was sealed by a 30.5 cm by 30.5 cm by 2.5 cm piece of quartz glass compressed against an O-ring, which has yet to be installed in the picture shown. The snaking silver tube between the vacuum system and the black box was part of the vacuum pump system. The black tubes coming from the black box were water-cooling. The water-cooling system was designed to keep the vacuum box and by extension the O-ring cool and prevent melting while the plasma lamp was on. The whole system was mounted on tracks so that the box could be moved into and out of the plasma lamp path. For set up, the box was out from under the plasma lamp as it is in this picture.

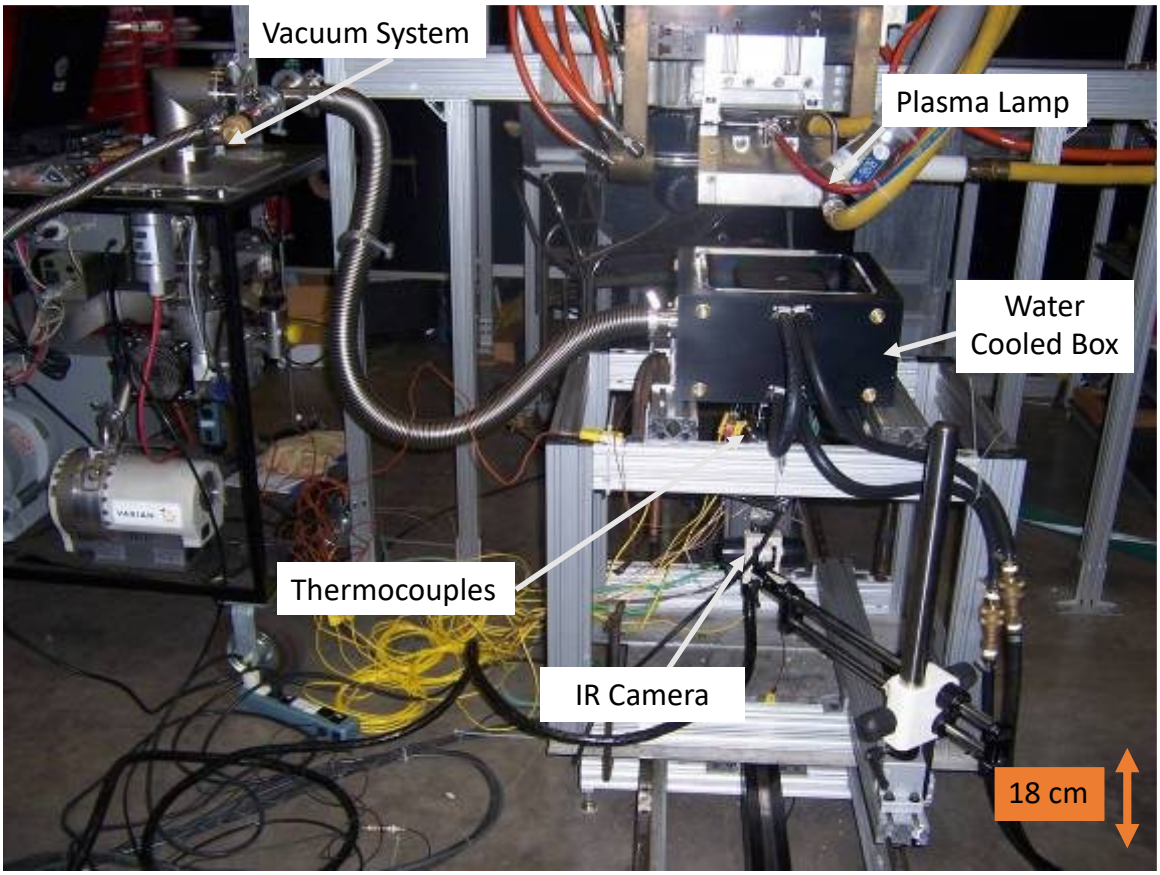

Figure 3-18 This test setup at Oak Ridge National Laboratory (ORNL) was used for carbon foam and coatings testing for Parker Solar Probe. This picture was taken during the first round of testing but is representative of all ORNL testing.

Finally, beneath the box was the instrumentation for thermal readings. The test instrumentation was slightly different between the test campaigns. This picture was from the first set of tests, in which temperature was measured through thermocouples and an IR camera. The IR camera was placed looking up at the middle of the sample. The yellow cables were thermocouple wires connected to the data acquisition system, which was in the upper left corner of the picture. A picture of the vacuum box in test configuration is shown in Figure 3-19.

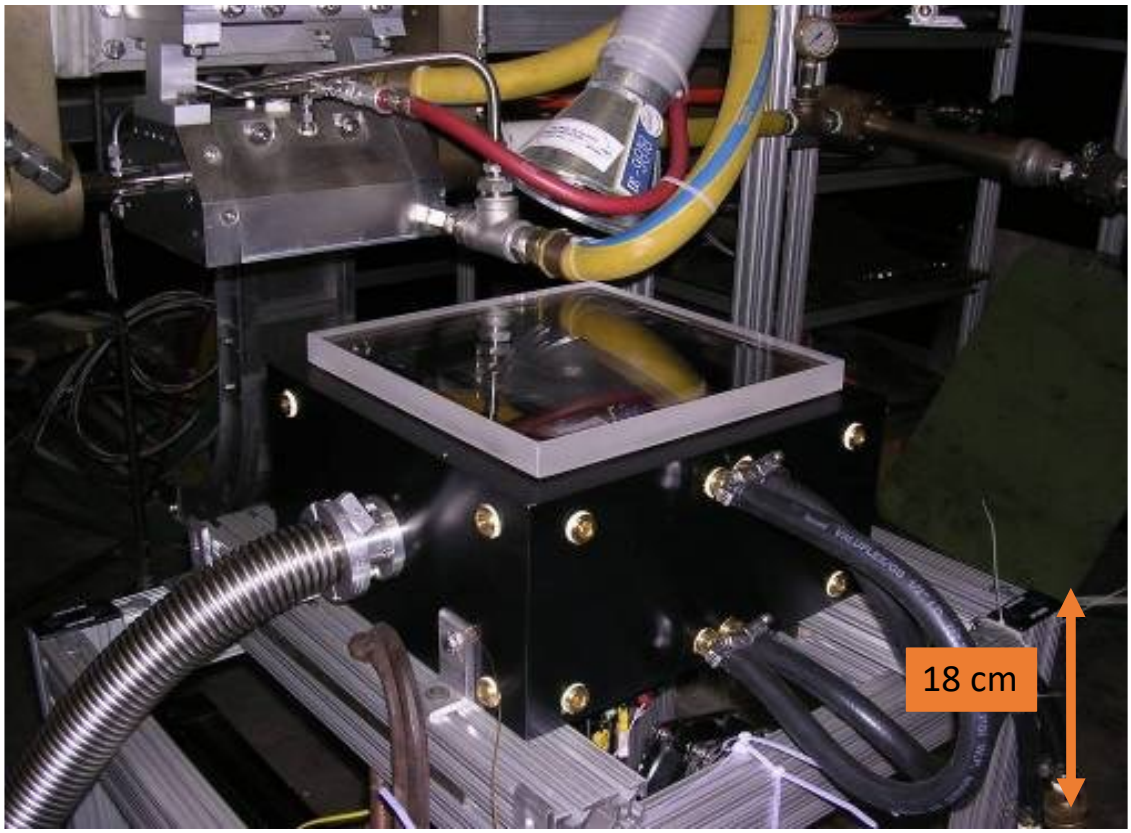

Figure 3-19 Vacuum box at Oak Ridge National Laboratory ready for testing

In this figure, the quartz was placed on top of the box and the box has been pumped down to $p \leq 1.0 \text{ x } 10^{-5}$ torr which compresses the O-ring that sits between the black box and the quartz. While this design was advantageous for test set up, the presence of the O-ring so close to the heat source, despite the O-ring sitting in a groove in the water-cooled box, created issues throughout the testing. The O-ring melted due to heating early in the test campaign. When the O-ring melted, it deposited remnants of itself on the quartz window. These portions of the quartz heated up significantly due to local imperfections. This phenomenon caused heat to be trapped in these areas. Brought to the extreme, this local heating might have caused the quartz to shatter, so improvements including an air knife around the O-Ring and insulation around the edge

of the box were used to minimized and reduced these incidents, and a protocol for shutting off the lamp and backfilling with argon prevented any safety issues.

It was possible to see through some of the samples due to their high porosity and therefore a thermocouple in the first inch of the sample would have a direct view of the lamp, affecting the measurements. When the lamp was shining on the thermocouple directly, it was heated up since it was exposed to a direct heat source. Since both the Ultramet and ERG foams had 97% porosity, this effect could be seen at multiple depths of these foams. In order to eliminate such errors, a piece of carbon-carbon was placed on top of the sample in order to block the direct lamp source.

Testing was performed by pumping down the vacuum chamber to a desired pressure level and then turning on the plasma lamp. The samples were desiccated and baked out beforehand, but the vacuum level still raised when the lamp turned on. The vacuum level was then stabilized at the desired value as measured, and then the temperature was held until the temperature of the back surface reached steady state. The time to reach steady state depended on the test temperature. The thermocouple data from each round of testing were used to develop models of the test setup and the effective thermal conductivity of each sample at various temperatures was calculated from this modeling.

3.8.1.1. Oak Ridge Testing Effective Thermal Conductivity: First Round

The samples, which were 15.2 cm by 15.2 cm by up to 11.4 cm thick, were placed in the middle of the vacuum box and the thermocouples were placed at different

heights in the foam. Figure 3-20 shows one of the carbon foam samples with a carbon facesheet (left side) and the thermocouples as they could be placed but with the sample removed (right side). For the first round of testing, the IR camera was looking at the middle of the back of the sample. Therefore, the thermocouples were input from the bottom at an angle so that they could be reading the middle of the sample close to the plasma lamp. Figure 3-21 is a picture of the thermocouple and IR camera set up for the first round of testing.

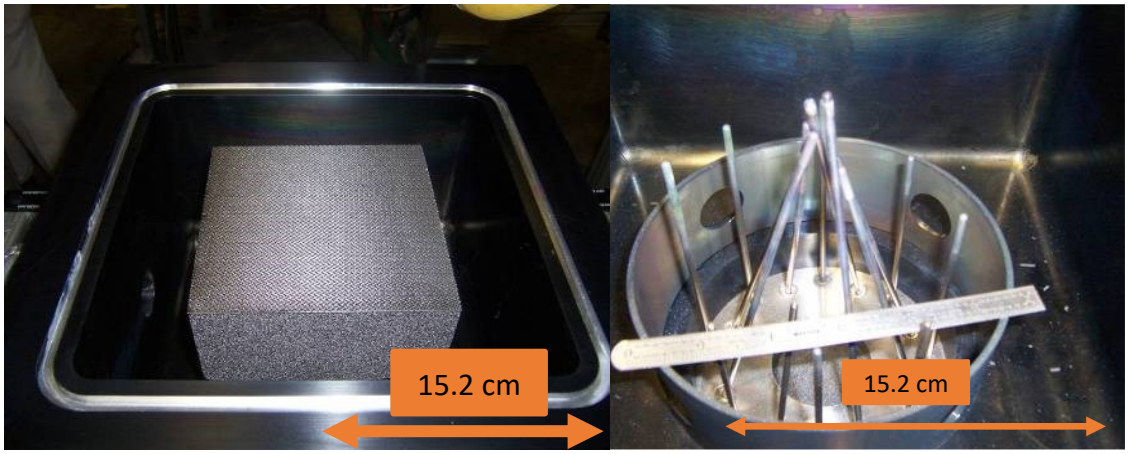

Figure 3-20 Left, carbon foam sample with carbon facesheet covering front surface; right, thermocouples as placed into the sample with sample removed for first round of ORNL testing. The cylindrical pedestal around the thermocouples is the sample support.

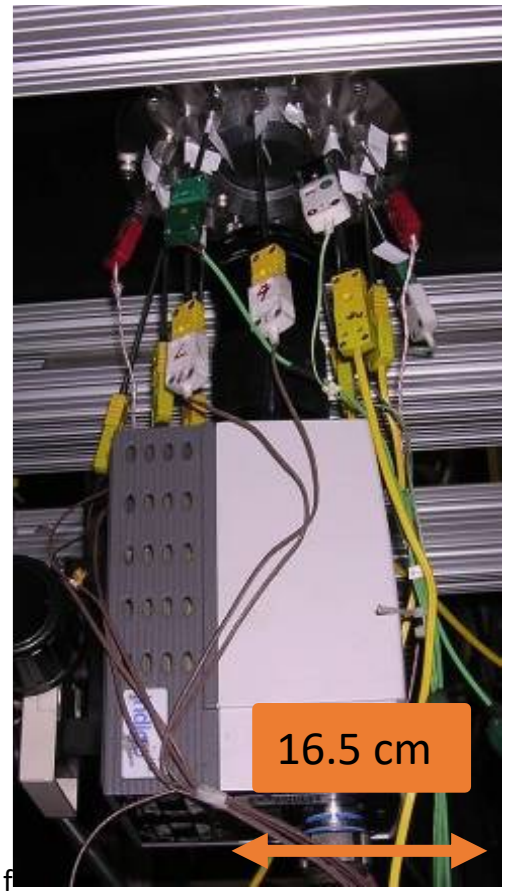

Figure 3-21 Thermocouple and IR camera placement beneath the vacuum box for the first round of ORNL thermal testing

During this first test set up, Ultramet 100 ppi 3% foam and ERG 100 ppi 3% foam were tested to measure the steady-state temperature of the various thermocouples and the back surface with the IR camera when the front of the coupon was exposed to 200°C, 500°C, 1000°C and 1500°C. These temperatures were controlled through the power settings on the plasma lamp and a vacuum of 10^{-5}torr was consistently achieved. The first round of testing was successful and the test set up proved valuable, and so we returned to ORNL for further testing a few years later. The goal of this second round of testing was to look further at the carbon foam and test the impact of carbon felt on the effective thermal conductivity results.

3.8.1.2. Oak Ridge Testing Effective Thermal Conductivity: Second Round

Several improvements were made for the second round at ORNL. The IR camera used during the first round demonstrated that the back surface was fairly uniform during testing; however, there were limitations to getting temperature data accurately from the IR camera and the thermocouples proved to be more reliable. Therefore, in the second round of testing, the IR camera was removed, and thermocouples were used exclusively to measure temperature. Without the IR camera, the thermocouple placement was greatly simplified. The testing schematic for the second round of testing is diagrammed in Figure 3-22. As shown in the bottom right corner, the thermocouples are inserted vertically on a smaller diameter than the first round of testing. The thermocouples for the second round of testing were placed such that a polynomial curve of temperature to thickness could be derived from the test data. The full thickness of the flight heat shield was used for this testing, so the samples were 15.2 cm by 15.2 cm by 11.4 cm. Figure 3-23 shows the placement of the six thermocouples that were used for the second round of testing.

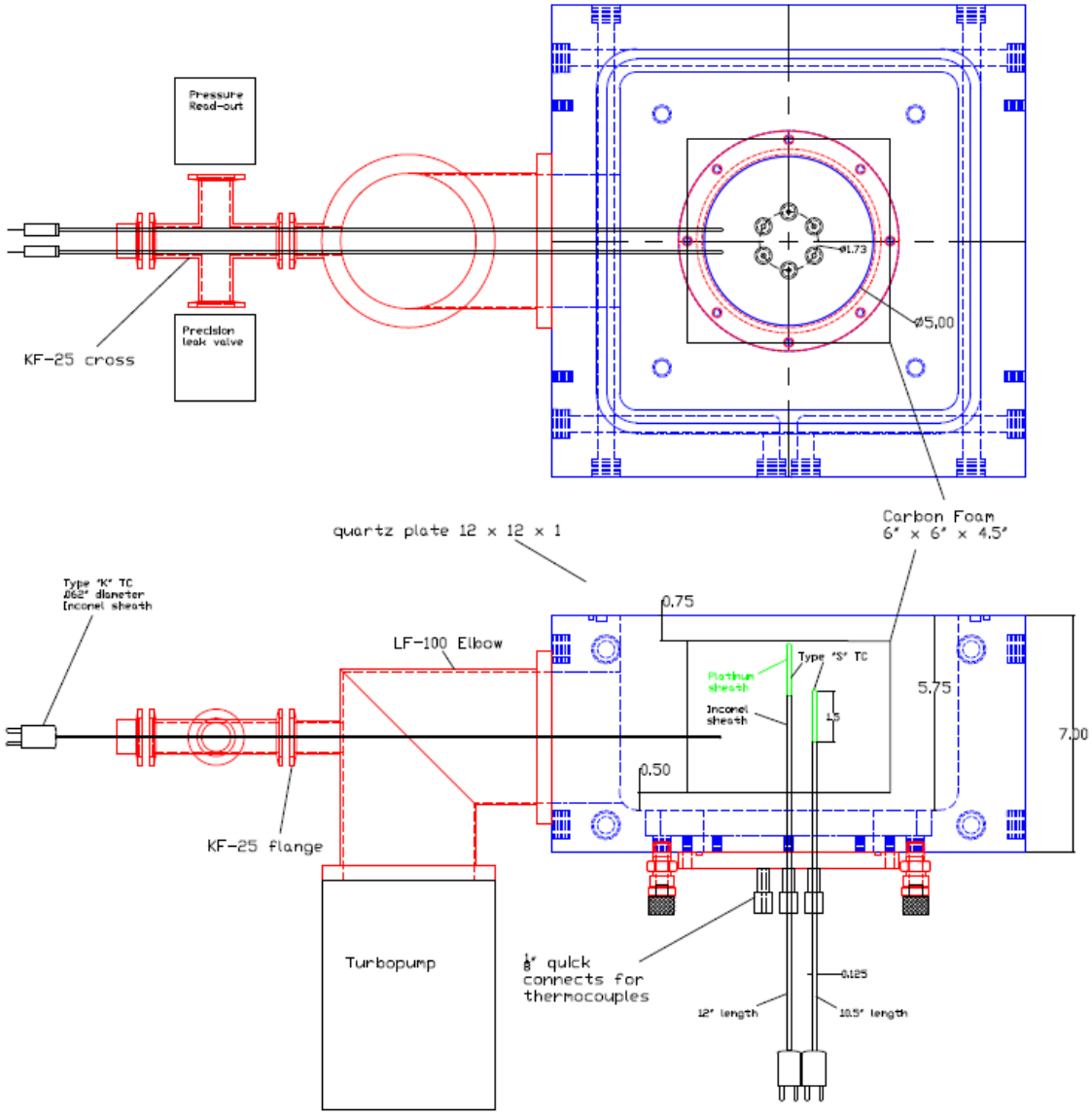

Figure 3-22 Schematic of the second round of testing at ORNL (Courtesy of ORNL)

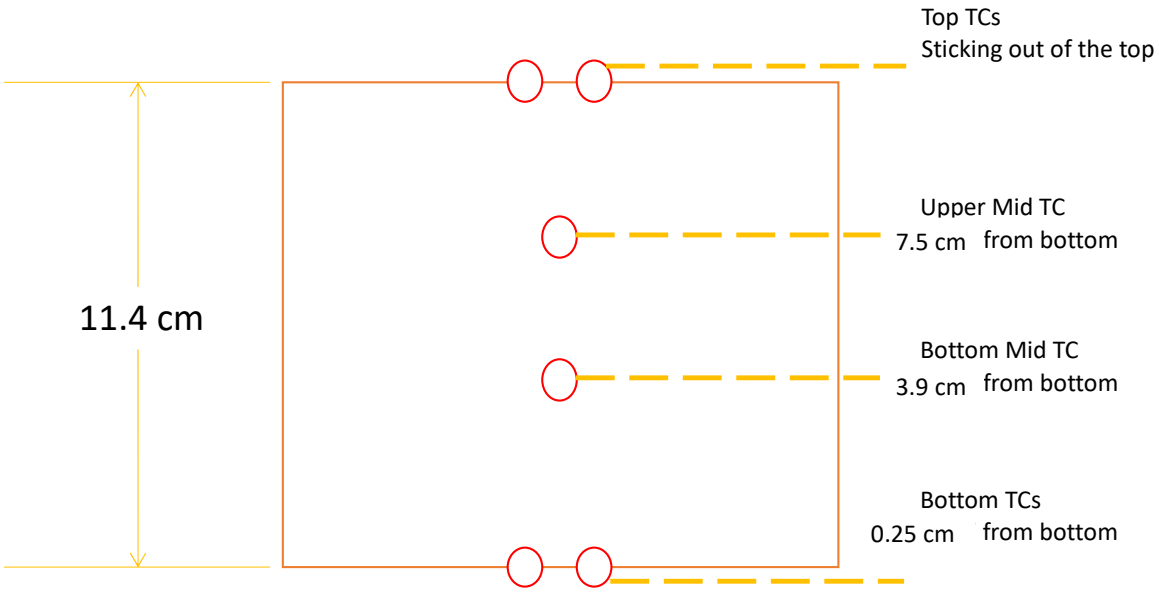

Figure 3-23 Thermocouple placement for second round of ORNL Testing

Additionally, since the test setup allowed for controlled pressure, the test setup offered an opportunity to confirm the hypothesis about the effects of the pressure on the results. Testing was performed at 10^{-6} torr, 10^{-3} torr, 0.5 torr and 1.5 torr. Additional testing was also conducted on the test set up to determine the repeatability of the lamp and uniformity of the lamp output over the surface. This test was also provided an opportunity used to measure the conductivity of the carbon felt and its effects on the design of the heat shield and to study manufacturing variations between blocks of foam manufactured by the same manufacture. This extra testing is not discussed in detail in this dissertation but is mentioned to provide context.

3.8.2. Limitations of Testing

The test conditions were such that it was difficult to achieve one dimensional heat flow in the ORNL test set up. The sample was small relative to other subscale samples.

The vacuum box was water cooled but didn't have a uniform temperature throughout the duration of the tests; the temperatures that were measured on the water-cooled box ranged from 12°C to 21°C. Comparing the data from tests that experienced a variation in water-cooling, the changing water temperature only correlated to a 1% variation in the effective thermal conductivity, therefore this variation wasn't a major effect. The lamp itself was also non-uniform as shown in Figure 3-24.

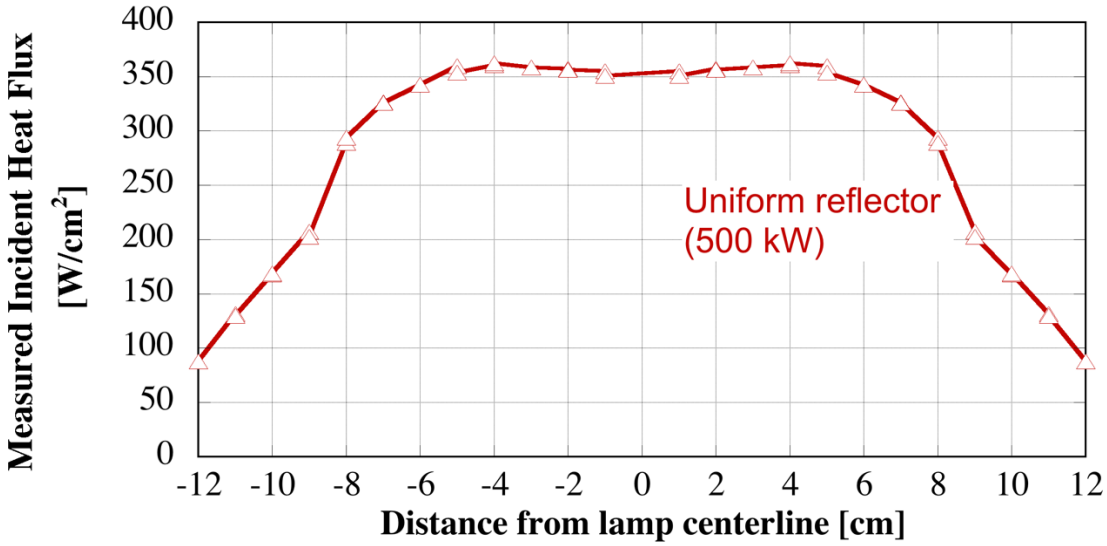

Figure 3-24 Lamp uniformity information as provided by ORNL

This profile, which was provided by ORNL, was used in the modeling of for the effective thermal conductivity. Therefore, the effects of this variation are captured in the results. The presence of the carbon-carbon on the front surface of the sample helped to present a uniform temperature by providing even heat input, particularly since the subscale articles were tested in steady-state.

3.9. Subscale Experimental Results Collected at ORNL

The subscale unit testing provided effective thermal conductivity data for samples that were the same thickness as the full-scale heat shield. This data proved invaluable to

understanding the thermal behavior of the foam at temperature since the results deviated from the coupon results. For this dissertation, the three subscale coupons of Ultramet 100 ppi 3% foam tested in a 10^{-5} torr vacuum was compared to the vacuum coupon data discussed in the previous section. An example of the data from the ORNL subscale testing is shown in Figure 3-25.

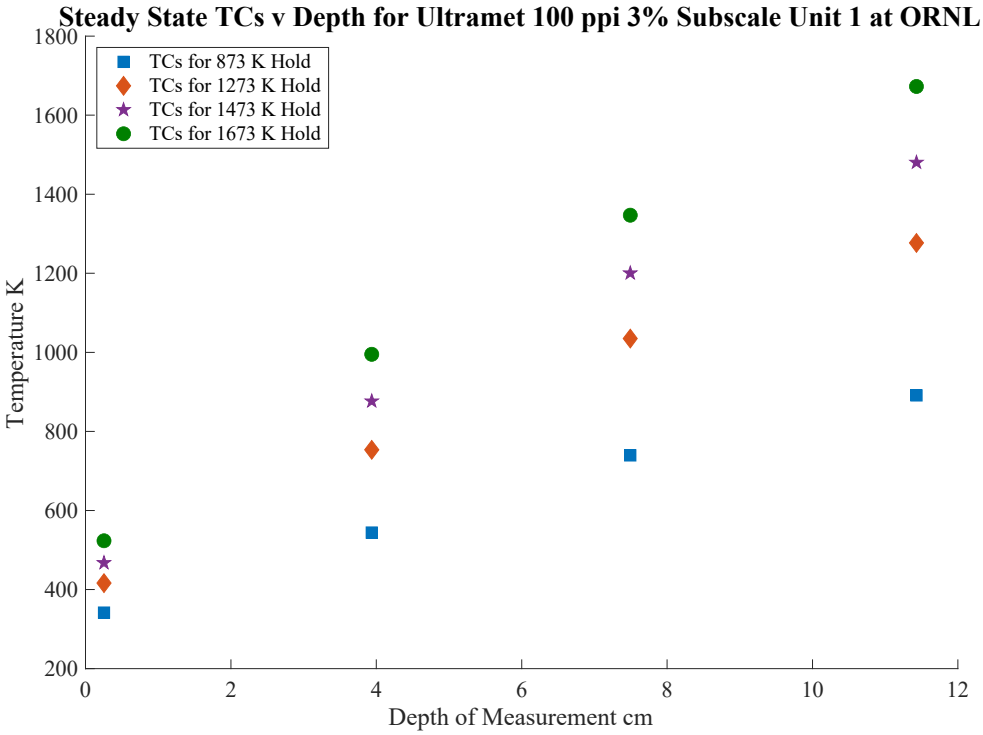

Figure 3-25 Example of test data from ORNL for subscale unit 1 of Ultramet 100 ppi 3% foam. The surface closest to the lamp heat source was at 11.43 cm (right) while the surface of the foam furthest from the heat source was near 0 cm (left). The four data sets represented lamp power steady-state holds that set the maximum temperature for at least an hour so that temperature data through the sample could be collected.

This data set was for one subscale coupon that was 11.43 cm thick, tested in vacuum. The lamp was taken to four different power settings resulting in four hold temperatures (600°C, 1000°C, 1200°C and 1400°C) and held for at least an hour once the coldest thermocouple, the one farthest from the lamp, reached steady state as defined

as within +/- 3 °C over an hour. Three Ultramet 100 ppi 3% foam subscale units were tested in this manner.

Using this temperature data, Elizabeth Heisler built a thermal model that built the box around the foam and applied the proper optical properties to the components of the ORNL test set up using Thermal Desktop®. This model was used to calculate the effective thermal conductivity through the sample as a function of temperature for each test setting. Figure 3-26 is a picture of the Thermal Desktop® Model.

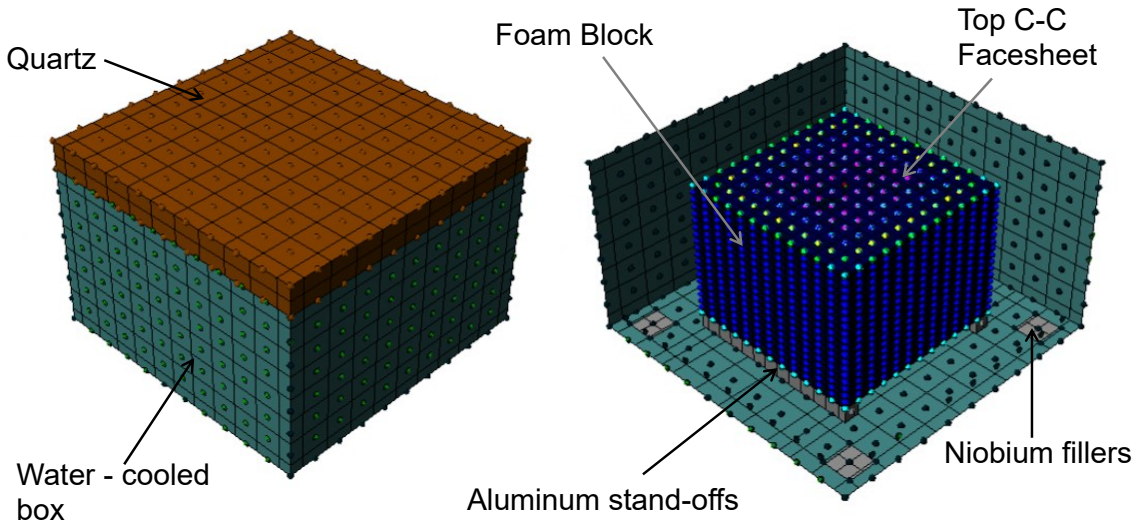

Figure 3-26 Picture of the Thermal Desktop® model from ORNL (Courtesy of Elizabeth Heisler)

The effective thermal conductivity for each of the Ultramet 100 ppi 3% subscale units tested were measured over a temperature range of 100°C to 1400°C. Figure 3-27 is a graph of the calculated effective thermal conductivity for the Ultramet 3% 100 ppi foam for subscale unit 1.

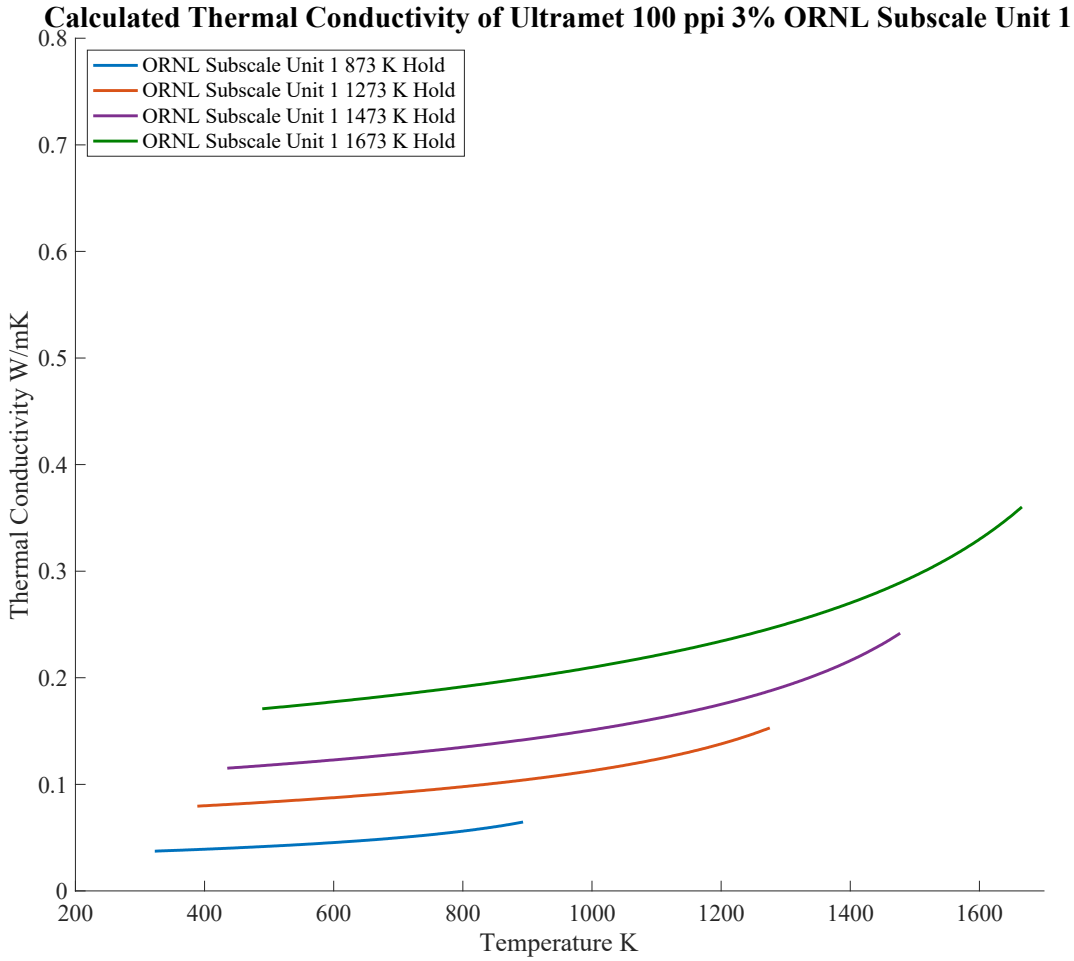

Figure 3-27 Calculated effective thermal conductivity for ORNL Subscale Unit 1. These thermal conductivities were calculated using the data from Figure 3-25 and curve fitting the effective thermal conductivity for steady-state hold.

Upon examining the data from this subscale unit, it is notable that the shape of the calculated effective thermal conductivity line is similar but the effective thermal conductivity is higher for holds set at higher temperatures. For example, the blue line, which was a steady-state front side temperature hold at 873 K, was the lowest calculated effective thermal conductivity while the green line, which was a steady-state front side temperature hold at 1673 K, was the highest calculated effective thermal conductivity. At 600 K, there are four different measurement values of effective

thermal conductivity ranging from 0.05 W/mK to 0.19 W/mK. While this could be the potential error in the test, the effective thermal conductivity lines appeared to have the same slope but different magnitudes suggesting that this phenomenon was a testing artifact driven by the assumption of the radiation of the back of the subscale unit to the water-cooled test box. This heat transfer was most likely less than the idealized assumption of the model since the coupon was on a pedestal and did not have an idealized view to the box. This non-idealized view would result in higher temperatures on this backside of the subscale unit than a perfectly radiative surface. For the purposes of comparing the data from the subscale testing to the coupon data, these differences were treated as the error on the calculated effective thermal conductivity from subscale unit testing. Figure 3-28 displays the vacuum effective thermal conductivity for Ultramet 100 ppi 3% compared with the calculated effective thermal conductivity for the ORNL subscale unit 3 tested in vacuum.

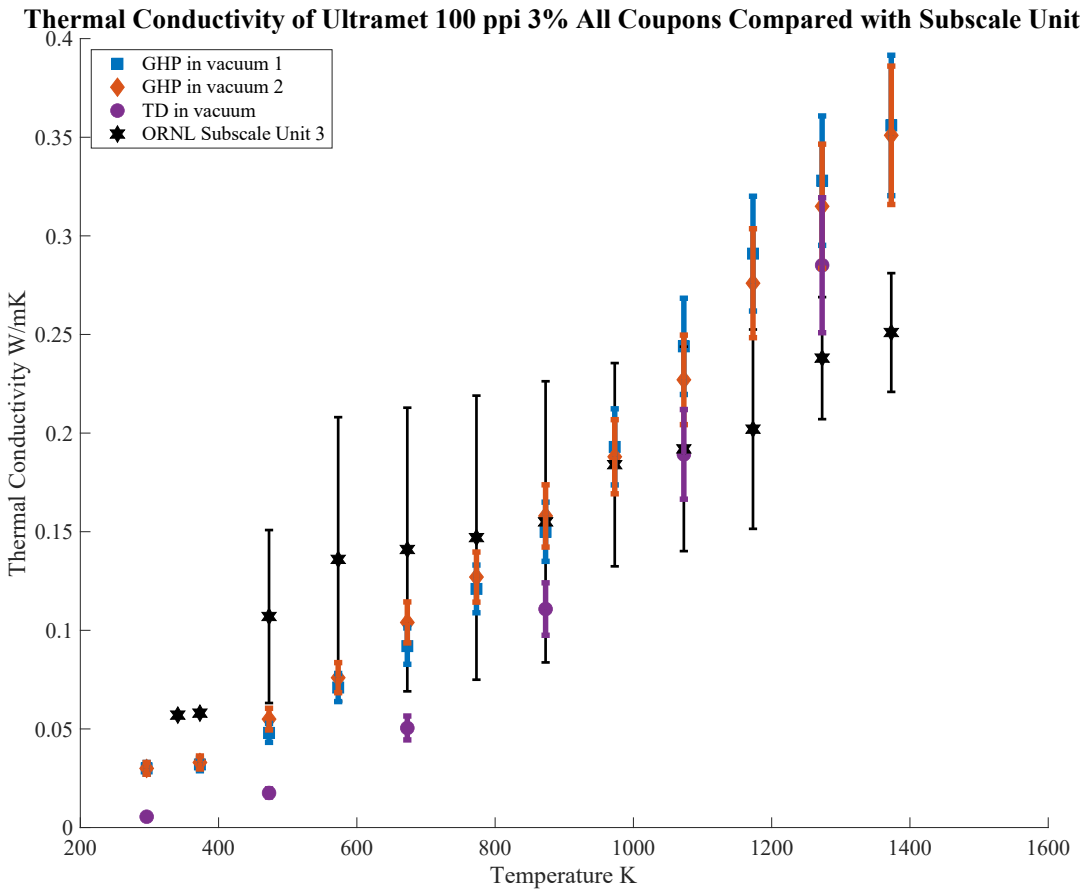

Figure 3-28 Ultramet effective thermal conductivity coupon data compared with calculated ORNL effective thermal conductivity. The black hexagons are the ORNL data and the blue, orange and purple data points are the in vacuum coupon data for comparison.

In the figure, the black data points representing the ORNL calculated results was overlaid with the coupon test data for Ultramet 100 ppi 3% foam. The data represented in the graph is from subscale unit 3. The graph of effective thermal conductivity for all the subscale units is in Appendix B. The subscale data and the coupon data were similar in magnitude but follow different trends, see for example Figure 3-28, where the coupon data steadily rose but the subscale unit test data followed an S curve. It is interesting that the subscale effective thermal conductivity measured at high temperatures was trending lower than the results suggested by the coupon data. The

subscale results indicated that the thin coupons overestimate the effective thermal conductivity at elevated temperatures. This finding could be related to the radiative component of thermal conductivity that is dominant at these higher temperatures. As the name suggests, Ultramet 100 ppi 3% foam has a relative density of 3%. As such, it is logical that the thickness would play a role in the effective thermal conductivity for thin pieces. The number of radiative surfaces inside the foam increased with increasing thickness of the tested unit and, due to the openness of the foam, the path of energy within the foam depended on thickness. At the higher temperatures, the thicker samples, representative of the actual full-scale heat shield, were assumed to provide the correct value and used to calculate a more accurate effective thermal conductivity.

For the design of the TPS, none of these numbers were used precisely. In the design, all the thermal conductivities results were compared, and bounding numbers were developed based on the full set of test data. These bounding thermal conductivities were ultimately used in the design. This approach provided a factor of safety and assured that the PSP TPS would meet all the thermal requirements. Nevertheless, comparing the coupon and subscale effective thermal conductivity measurements provided valuable insight into the fact that the dominant heat transfer mode for carbon foam switched from conduction through solid ligaments at low temperatures to radiation at elevated temperatures. Moreover, the coupon tests were determined to be more accurate than the subscale tests at low temperatures but to slightly overpredict the heat transfer at elevated temperatures. With this understanding

of effective thermal conductivity in carbon foam, its influence on the overall TPS system can be developed.

3.10. Full Scale Testing

The focus of this dissertation was the effective thermal conductivity of the carbon foam and the role of multiscale testing in determining the behavior of the full-scale system. Ideally this approach would have been validated by testing a full scale TPS in a flight-like hot environment. This flight-like environment would involve simulating the intensity of the Sun at 475 times its effect on Earth and in the vacuum of space. Existing facilities that can reach these temperatures cannot simulate the vacuum of space. Experiments at NASA's AFRC and NASA's JSC were conducted to explore the feasibility of testing a full-scale unit. Given that the performance of the PSP TPS needed to be understood in steady state testing, the tests needed to be performed over long periods of time, on the order of hours. In addition to the difficulty of performing these long duration tests, the test articles experienced noticeable oxidation even with minimal presence of oxygen when using a cover gas. This oxidization and the convection that was present for this testing meant that it was nearly impossible to separate out test artifacts from expected behavior. Additionally, degradation of the test article was a concern. For expensive full-scale flight units, it was unacceptable to have any degradation. For these reasons, full-scale high temperature testing was deemed unfeasible given the cost and schedule constraints.

Full-scale cold testing was performed to demonstrate capabilities of the system in the cold range of the thermal cycle requirements. Figure 3-29 shows the PSP TPS being

prepared for thermal vacuum testing at Goddard Space Flight Center (GSFC). The TPS system was designed to operate from -100°C to 1300°C and many of the materials were optimized to perform at the high temperatures. This GSFC testing proved that the system survived the strain resulting from the variations in coefficient of expansion (CTE) of the various materials in the sandwich panel at cold temperatures by the unit staying intact through thermal cycling. This cold thermal testing is not covered in detail in this dissertation since the scope of this document is the testing of the carbon foam. This testing is one of the many tests that were part of the larger test program.

Figure 3-29 The PSP TPS is prepared for cold thermal vacuum testing as part of its qualification testing at GSFC. Photo by Ed Whitman, JHUAPL. [58]

3.11. Discussion and Summary of the Thermal Results

Significant research has been conducted on the effective thermal conductivity of foams around room temperatures and the delineation between conduction, convection

and radiation [20, 25, 59]. In the last decade, there has been an increased interest in the thermal properties of porous materials at higher temperatures and these studies have shown that it is difficult to characterize the effective thermal conductivity because testing is difficult at temperature [26-28, 60-62]. There is still limited data and modeling at the temperatures of interest to PSP at 1600 K. This dissertation presents a data set for carbon foam up to 1600 K.

For these types of applications, the critical components of effective thermal conductivity are the solid component and the radiative component. Tseng et al studied SiC foams and showed that the solid conductivity was the main component around room temperature, radiation started to effect the effective thermal conductivity at 500 K and the radiative component became dominate above 1000 K [61]. In this dissertation, the Ultramet 100 ppi 3% foam effective thermal conductivity was shown to be mostly solid conductivity around room temperature and the radiative component became equal to the solid component around 900 K. The solid and radiative components were broken out from each other using modeling and studied separately.

The solid component, which was dominate around room temperature, was shown to be affected by structure. The Ultramet 100 ppi 3% foam data around room temperature matched well with the 2/3 efficiency factor suggested by Gibson and Ashby [23], however the Grafoam mixed density foams were shown to be correlated to an efficiency factor between 1/3 and 4/9. Glicksman and Schuetz and Choi et al. suggested that the efficiency factor would be effected by the structure and material of the foam [25, 52]. These authors noted that the efficiency factor could be influenced by void fraction in the

foam as well as the fraction of solid of the struts. The Ultramet 100 ppi 3% is an open celled foam that more closely matches the Gibson and Ashby ideal while the Grafoam is a mixed open and closed cell foam thereby deviating from the ideal and the 2/3 efficiency factor. Fundamentally, the solid component of the thermal conductivity is driven by this efficiency factory multiplied by the conductivity of the solid. For example, for carbon foams the degree of graphitization is a critical component in the effective thermal conductivity of the material. As Khairul Alam and Maruyama noted, the effective thermal conductivity of carbon foams can range from 1 to 2000 W/mK depending on the crystallographic definition of the material [59]. For the PSP TPS, amorphous carbon foams were targeted due to the desire for low thermal conductivities in the application. When designing open celled foams for use around room temperature in vacuum, optimization should be done around the solid conductivity of the underlying material.

As the use temperature increases above room temperature, the radiative component is more critical. In addition to Tseng et al, Sans et al also has studied open celled ceramic foams however all have been limited in temperature range [28, 61]. Sans et al performed testing to validate modeling up to 1073 K on ceramic foams. Similarly, Tseng et al modeled up to 2300 K and performed testing up to 1400 K using the Laser Hardened Material Evaluation Laboratory (LHMEL) at Wright-Patterson Air Force Base. Li and Wang built models up to 750 K to examine the effective thermal conductivity of ceramic foams at high temperatures [26]. The carbon foam under study in this work followed the same trends as all these studies on ceramic foams, radiation increasingly

dominating the effective thermal conductivity as the temperature increases. The radiative component of thermal conductivity is more complex and less studied than the solid component but this work provided some insight into the behavior.

Coupon data in this dissertation was used to understand the influence on structure in effective thermal conductivity. Calcarb and Grafoam FPA-10, which have the same relative density but different structures, were compared in order to examine the influence of foam architecture. These same density foams had diverging effective thermal conductivity data at higher temperatures suggesting that structure influences the radiative component of thermal conductivity that ultimately dominates at high temperatures. This result aligns with Coquard et al who showed that structure influenced the radiative component of thermal conductivity in ceramic foams up to 1100 K [60]. Additionally, Tseng et al demonstrated that pore size had an effect on the extinction coefficient [62]. The results from this dissertation demonstrating experimentally that there was an effect of structure on carbon foam effective thermal conductivity at high temperatures is grounded in results from the literature on ceramic foams.

The coupon data for Ultramet 100 ppi 3% foam was used to show that the Rossland approximation overestimated the effective thermal conductivity at 1400 K. Further the subscale testing on the Ultramet 100 ppi 3% foam indicated that the effective thermal conductivity measured at the coupon level overestimated the effective thermal conductivity of the foam at temperatures above 1100 K which indicates that the thickness of the material is important to the radiative heat transfer. Sans et al studied

the effect of optical thickness, as defined by the extinction coefficient times the thickness of the sample, on effective thermal conductivity [28]. Since the mean free path of a photon is related to the extinction coefficient, the radiative component of the thermal conductivity is influenced by thickness and structure of the material. Sans et al studied structured and random ceramic foams delineating them by the optical thickness parameter; they showed that the lowest overall conductivity at 1073 K was measured on the random structured highest pores per inch foam [28]. The subscale results in this dissertation showed the importance of thickness on the effective thermal conductivity results particularly at high temperatures where radiation was the dominant component of the effective thermal conductivity.

While the PSP TPS foam selection was driven by manufacturing constraints, mass of the overall foam and structural performance, the results of the effective thermal conductivity study can be used to understand how foam could be manipulated for improved thermal properties. Knowing the roles of the components of the effective thermal conductivity on the performance of foams at temperature, foams can be optimized for structure, density, and reflectivity. Based on the findings of this research, ideally foam could be optimized where the main structure of the foam is a material with low effective thermal conductivity and then this foam can be coated with a material to optimize the reflectivity properties thereby minimizing the radiative component. Low-density small pore per inch foams are ideal to minimize the solid conductivity and they are also most dominated by radiation at high temperatures [25, 62]. Li and Wang modeled alumina foams and showed that for identical structures the foam material with

the higher reflectivity has a lower radiative conductivity [26]. These observations taken together mean that the most optimal foam for these high temperature applications could be designed with a low-density, low-conductivity material and then coated to increase reflectivity.

Effective thermal conductivity testing was an important element of understanding and predicting the behavior of the heat shield at the Sun. Testing of carbon foam coupons and subscale panels was difficult in the environments and temperatures of interest and testing on full-scale articles in the proper environment was not feasible. However, testing was performed at multiple scales and compared and contrasted to understand the true behavior of the carbon foam. Each of these tests had their own limitations, but together they formed a clear picture of the effective thermal conductivity of the foam and how it was influenced by a variety of factors. Coupon and subscale testing was used to measure the effective thermal conductivity of the carbon foam so it could be used in the full-scale thermal model, and the full-scale thermal model was used to analytically provide the expected performance of the PSP TPS during its exposure at perihelion of the Sun. While PSP has yet to make its closest pass to the Sun, the spacecraft has successfully completed six close approaches to the Sun at three different solar distances. All temperature sensors on the spacecraft indicate that the PSP TPS is performing as expected at temperature. The work outlined in this chapter for determining the effective thermal conductivity of the carbon foam formed the basis of this mission success. However, thermal performance is only one component of the necessary material properties needed to design the PSP TPS. The carbon foam structural

properties needed to be developed to prove the design could survive launch and the thermal-structural stresses at the Sun; these properties will be discussed in the next chapter.

CHAPTER 4. Structural Properties

As with the thermal testing, the structural testing methodology involved multiple scales of testing with each approach investigating a different aspect of the carbon foam material. Coupon testing was used to understand the material properties of the foam, explore the effects of anisotropy and test the hypotheses of the Gibson and Ashby models. Ultimately, the coupon data was developed into a material properties dataset which were used in full-scale finite element (FE) modeling. These FE models were used to enable quantitative design and optimization of the heat shield and show that the heat shield would successfully withstand launch loading and the thermal extremes from perihelion to the cold temperatures of aphelion.

Coupon data was used to ascertain basic material properties that were used in modeling, however the data had limitations in verifying the failure mechanisms and load paths that are active at the full scale. Subscale level testing was used to bridge this gap. These subscale units were taken to failure with controlled boundary conditions to attain an understanding of how failure would happen at full-scale. Most subscale testing that was performed as part of the PSP TPS development effort was on sandwich panels that included bondlines and the carbon-carbon facesheets thereby investigating the behavior of the system. For the purposes of this dissertation, the focus was on the carbon foam, as such, the fracture toughness testing of the carbon foam is discussed as a representative subscale test.

For full scale testing, the test was not taken to failure since margins of safety were used in the design of the full-scale article so that this testing was pass/fail with an

expectation that the unit would pass. Full scale testing was designed to demonstrate that the article could survive the expected loading imparted mostly from the launch environment. Full-scale testing was only a component of the overall test program because it is not a good scale to understand the mechanisms of failures. When failure occurs on a full-scale test article, the origin can be complex and difficult to isolate. Additionally, full-scale articles are expensive and time consuming to manufacture, store and handle. In the case of the PSP TPS, all full-scale units passed all testing.

The approach of integrating coupon testing, subscale testing and full-scale testing was utilized to successfully develop the PSP TPS. This chapter outlines and reviews the way this approach was employed to ensure that the carbon foam would survive launch loading as well as thermal loading, which was driven by warping caused by coefficient of thermal expansion (CTE) differences between the materials.

4.1. Structural Properties Experimental Procedures

It was necessary to characterize the structural behavior of the carbon foam in order to design and qualify the PSP TPS. For structural testing, unlike high temperature thermal testing, it was possible to test a full-scale unit in the relevant launch loading conditions. In fact, four full-scale units underwent a full structural qualification program as part of the PSP TPS development. Concurrent with this full-scale testing hundreds of coupon and subscale tests were also performed. This coordinated effort examined the materials in the PSP TPS in tension, compression, shear, biaxial loading, fatigue, adhesion, fracture, hydrostatic testing, process improvement testing, and batch

qualification testing. The design of experiment (DOE) for this testing included all the materials that made up the PSP TPS. As with thermal testing, this dissertation is focused on the basic properties of carbon foam at the coupon level and a demonstrative subscale test: fracture toughness testing. The coupon and the fracture toughness tests were used to define the structural properties and established an understanding of the behavior of the foam at multiple scales. Full-scale testing was critical for qualification but has limitations as the mechanistic understanding of the materials cannot be teased out easily, which was why multiple scale testing was important even if full-scale testing is possible.

One of the many challenges of testing carbon foam was ensuring that the testing was happening at a meaningful scale for the material. If the specimens employed for the test were too small compared to the material's intrinsic length scales, the scale over which variations occur, then the test results would only represent the local behavior or properties of the material, which can be very different than the more general or global properties. If the coupon was too large, then the test could be difficult to control and it could be difficult to get the proper loading condition.

One way to address this problem is to rely on ASTM standard tests. These tests are designed to exhibit the behavior of a material at a proper length scale. For example, in the shear test, ASTM C273, the coupon size called out is a ratio of the thickness of the material, the length of the material and the width of the material. Subsequently, the coupon size was driven by the size scale of interest. However, this approach also had its

downfalls. For example, the test data might not be universally applicable if it is focused on a particular test set up or thickness.

Additionally, these low-density foams are sensitive to loading conditions so it was often difficult to employ standard methods. If the loading axis or loading surfaces had anything irregular, it might have driven a false positive or a false negative. The boundary conditions of the test set up could then have a significant effect on the results of the testing. These low-density carbon foams were sensitive to point loading. Therefore, the way the load was applied in the test set up, compared to the way the load will be applied in the real application was extremely important. Even when following ASTM standard test methods, care had to be taken to apply the loading in a way that not only mimics the loading conditions in practice but also avoids loading cases that could produce false negative results.

In this application where the foam is serving as the core of a sandwich panel, the foam is loaded through the facesheets which act as load spreaders. The bondline type and attachment was critical, and that was where the foam often failed during testing. Such experiments surveyed the effect of boundary conditions on the foam but are not a good representation of the intrinsic behavior or properties of the foam alone. Good test practices state that the material under test should not fail at the boundaries because then you are testing the boundary conditions and their applicability to the test not the material itself. However, when testing foam in a sandwich panel and getting a failure at the bondline, this is an applicable failure mode. In fact, it is how these types of structures actually fail. So, this type of failure in testing can be representative and valid

for the sandwich panel while not being representative or valid for the core. This statement is an important distinction because of the way the data is being used. If the data that comes from the testing is being used to describe the full system, then it is a valid failure mode. If it is being used to describe only the foam or only the bondline, then it is inappropriate. The challenges associated with developing valid tests for these materials meant that each test type underwent extensive investigation and trials to determine the right approach. The following sections outline the ultimate test approaches that were used for structural testing of the carbon foam.

4.2. Coupon Testing Methodology

A variety of coupon tests were performed on the carbon foams of interest. For the purposes of this dissertation, coupon testing in tension, compression and shear will be the focus. The thermal testing surveyed a range of foams to determine their applicability to the PSP TPS. From this process, the Ultramet 100 ppi 3% and ERG 100 ppi 3% were down selected due to their overall mass, manufacturability and thermal performance. These foams were the emphasis for structural testing. The coupon test results were used to understand the effects of anisotropy, comparing this anisotropy against the Gibson and Ashby hypotheses [23], and analyzing the effects of this anisotropy at the subscale level. JHUAPL contracted Touchstone Research Laboratory in Tridelphia, WV to perform these coupon tests due to their experience in testing low-density foams. The carbon foams were loaded in tension, compression and shear as discussed below.

Each block of material was machined so that samples were taken from the three primary directions so that the anisotropy of the block could be analyzed. Figure 4-1 is

the cut plan for one of the batches of Ultramet 100 ppi 3% foam: Batch 6; these cut plans allowed us to keep track of the location of each of the samples. Testing was also performed on off axis coupons but is not included in this dissertation. A variety of batches and foam types were tested as part of the PSP TPS qualification program to understand manufacturing variability and ensure suitability of each block of foam that was used in the full-scale articles. Over 500 samples were tested in tension, over 500 samples were tested in compression and over 500 samples were tested in shear. The bulk of this testing was used to determine the potential variability of the carbon foam materials and to verify that each batch of foam met material requirements. For the purposes of this dissertation, Batch 8 Ultramet 100 ppi 3% and Batch 6 ERG 100 ppi 3% are discussed as representative data. Batches, as they were received, were delineated by foam blocks that were processed together and numbered. For each direction and test type of interest, 5-10 specimens were tested. Specimens were machined into cylinders of varying sizes for testing. Table 7 shows sample dimensions used for coupon testing. The compression and tension samples were 5.1 cm round by 5.1 cm long cylinders while the shear samples were 2.5 cm by 12.7 cm long. Cylindrical samples were easy to machine on a CNC mill with a 12.7 cm long 0.64 cm diameter carbide end mill [63] and the shape meant that there were no sharp edges that could be stress concentrations during testing. Dogboning the samples to force failure in the middle of the sample was found to be unnecessary as the cylindrical samples failed consistently in the middle of the samples.

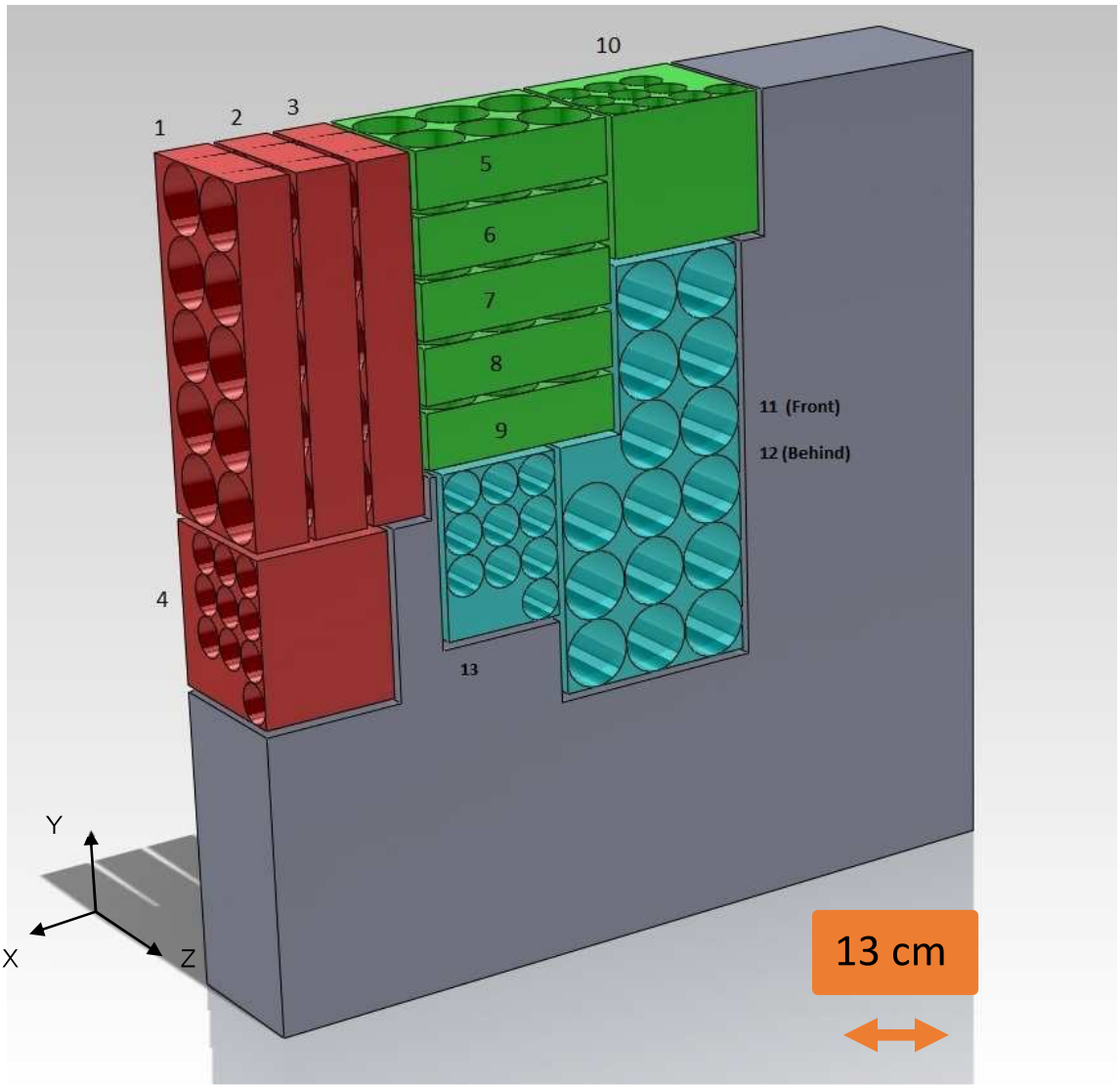

Figure 4-1 The cut plan for Batch 6 Ultramet 100 ppi foam. Coupons of various sizes represent different test types which are described below. Coupons are cut in all three primary directions of the block [64]

Table 7 Specimen size for coupon level experiments

Specimen Type	Shape	Specimen Size
Tension	Cylindrical	5.1 cm (diameter) by 5.1 cm (length)
Compression	Cylindrical	5.1 cm (diameter) by 5.1 cm (length)
Shear	Cylindrical	2.54 cm (diameter) by 12.7 cm (length)

When testing the foam in tension or compression, Locktite epoxy was used to reinforce the ends of the specimen to generate appropriate failures in the middle of the specimens and avoid interaction with the test fixtures. For tension, epoxy was filled evenly into the foam loading edges to ensure a good surface area contact. The specimens were dipped in a layer of epoxy and then allowed to dry. While there was some wicking into the foam, the epoxy only filled a few cells on each side therefore remained in less than 3% of the overall length of the sample. Then the coupons were machined flat using the epoxy as the main loading surface. These flat surfaces were bonded to the fixturing using Locktite-5-minute quick set epoxy. A similar technique was used to reinforce the ends of the compression coupons however, aluminum sheets were added to the samples directly after the epoxy was applied to ensure perpendicularity of the specimens. As standard process, coupons were loaded, and the failure mechanism was examined. If the failure could be traced to these bonding surfaces or interfaces, then the test was deemed invalid.

4.2.1. Tension

Tension was performed on 15 to 30 samples per batch using ASTM C297, "Standard Test Method for Flatwise Tensile Strength of Sandwich Constructions,"[65]. The objective of the testing was to determine the ultimate strength and elastic modulus of each sample. As such, the stress and displacement were monitored during the testing using an extensometer. Figure 4-2 is the tensile test set up for the carbon foam. The tensile specimens were loaded in United SFM-20 electromechanical load frame which had a 20,000 lbf capacity and the strain was measured using a 2.54 cm gage length MTS

634.12E54 extensometer. The initial test speed was 0.127 cm/min with a 10Hz data acquisition rate [64].

Figure 4-2 Flatwise tensile testing of carbon foam at Touchstone Research Laboratory [66]

Each sample was observed for proper failure; failure of the sample needed to occur away from the edges of the sample to be a valid failure. As with the thermal testing, structural testing of the foam was hampered by its delicate nature. The foam was difficult to handle without breaking and was very sensitive to point loading. This delicateness meant that loading and handling needed to be carefully planned. Putting the epoxy over the full surface of the top and bottom surface of the foam helped distribute the loading. Additionally, the extensometer needed to be carefully placed on the sample to ensure that it did not create a stress concentration in the foam. The extensometer had sharp edges, so yellow vinyl tape was used on the foam to prevent the extensometer edges from damaging the foam, as shown in Figure 4-2.

The ASTM C297 provides guidelines that the core specimens should not be less than 6.45 cm^2 in area and that it should test at least 60 cells. Both guidelines were met with the approximately 5.1 cm diameter samples and 40 pore per cm foam. Larger samples than required were chosen for this testing for easy of production and handling. The larger samples also allowed for wicking of the epoxy into the ends without having a large effect on the overall length. The goal of this testing was to get tensile failure in the foam since specimens did not have the carbon-carbon facesheets and were instead was carbon foam bonded to aluminum with the locktite epoxy. This approach allowed for isolation of the carbon foam tensile properties from the rest of the sandwich panel. The other constituents of the PSP TPS were assessed elsewhere.

The only notable deviation from ASTM C297 was to use the extensometers for strain measurement by attaching them to the foam. Early testing attempted to use

other strain measurement methods, specifically the crosshead displacement or digital image correlation (DIC) to determine the displacement. The crosshead displacement was known to have errors in determining displacement due to the joints between the grips and the crosshead. Carbon foam was uniquely difficult to perform DIC on as it is black and shiny. While under load, the displacement caused the ligands on the edges of the foam to twist. Movement and twisting of a ligand did not equate directly to strain in the overall specimen and would create artifacts in the strain measurements. Speckling with baby powder was attempted but did not eliminate the artifacts from the moving ligands. These issues meant that these were not practical methods of getting displacement measurements. The extensometer proved to be consistent and accurate the vinyl tape was used to prevent digging of the sharp edge into the foam but was only on the outside of the specimen and therefore did not affect the internal behavior.

In all over 500 tensile tests were conducted on over 30 batches of 6 different carbon foams, the raw data for the tension tests of one batch of ERG 100 ppi 3% foam is shown in Figure 4-3. This foam was manufactured in rectangular prisms approximately 75 cm by 75 cm by 13 cm. The longer in-plane directions of the manufactured foam were labeled lateral and the thinner direction was labeled through-thickness. The through-thickness direction corresponds to the primary heat flow direction. The primary mechanical loads for the flight article included compression, tension, shear, and bending from launch and thermal loading; therefore, the full anisotropic mechanical response

was needed to design to avoid failure. The lateral and through-thickness direction map to the orientation of the foam in subscale articles and the full-scale heat shield.

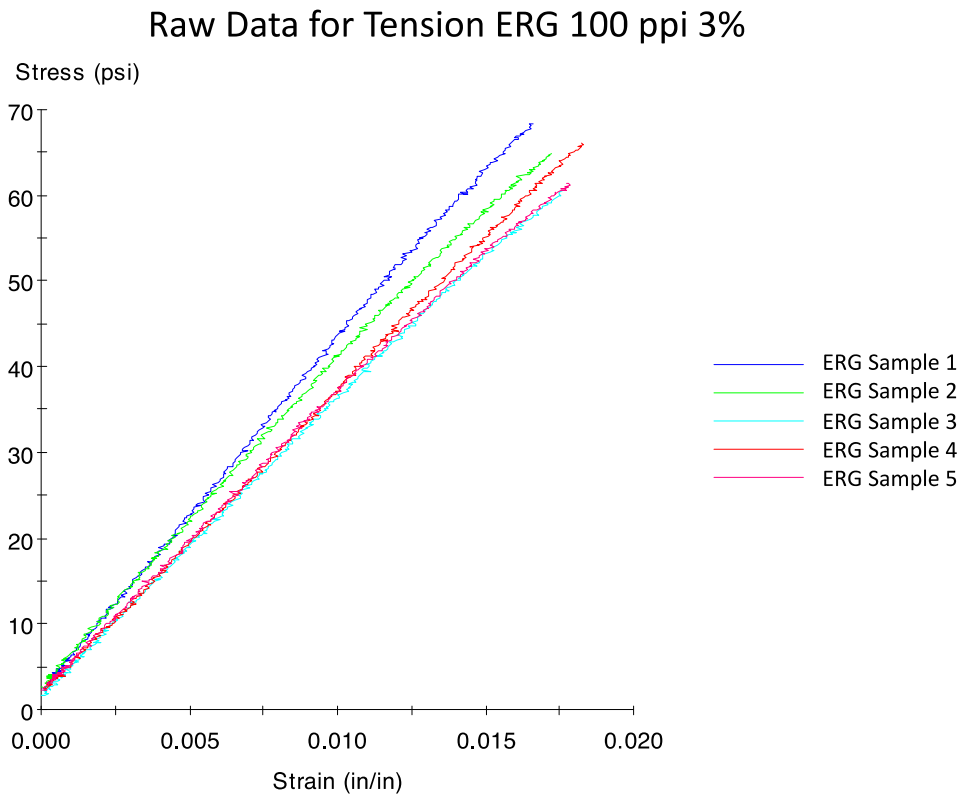

Figure 4-3 Raw data from the ERG tension test in the through thickness direction [64]

Force and displacement over time were measured outputs from the testing. The desired calculations from these inputs were ultimate strength and modulus. The tensile modulus was calculated from the slope of the stress-strain data. For this brittle material, the modulus calculation is fairly straightforward. The equation for ultimate tensile strength of the material is [65]:

$$F_z^{ftu} = \frac{P_{max}}{A} \tag{15}$$

where:

$F_z^{ftu} = Ultimate\ Tensile\ Strength\ in\ z\ of\ the\ core$

$P_{max} = Maximum\ Load\ prior\ to\ Failure$

$A = Cross\ sectional\ area\ of\ the\ specimen$

As shown in Figure 4-3, the ERG 100 ppi 3% foam had classic brittle behavior, demonstrating linear-elastic behavior until fracture in tension. The extensive testing that was conducted in all three dimensions provided the properties that were used for the FEM modeling and used to explore the anisotropy of the material. For this dissertation, five samples of ERG 100 ppi 3% foam were tested in each direction. The results are summarized in Table 8, Figure 4-4 and Figure 4-5. The bars represent the mean value with the error bars indicating the standard deviation of each measurement. The two lateral directions were different and the difference in modulus and strength switches from the first and second lateral direction.

Table 8 Tensile experimental results for a batch of ERG 100 ppi 3%

	Tensile ERG 100 ppi 3%			
	Strength (kPa)	Std Dev	Modulus (MPa)	Std Dev
First Lateral Direction	497	50	44	5
Second Lateral Direction	618	28	42	4
Through Thickness Direction	443	22	26	2

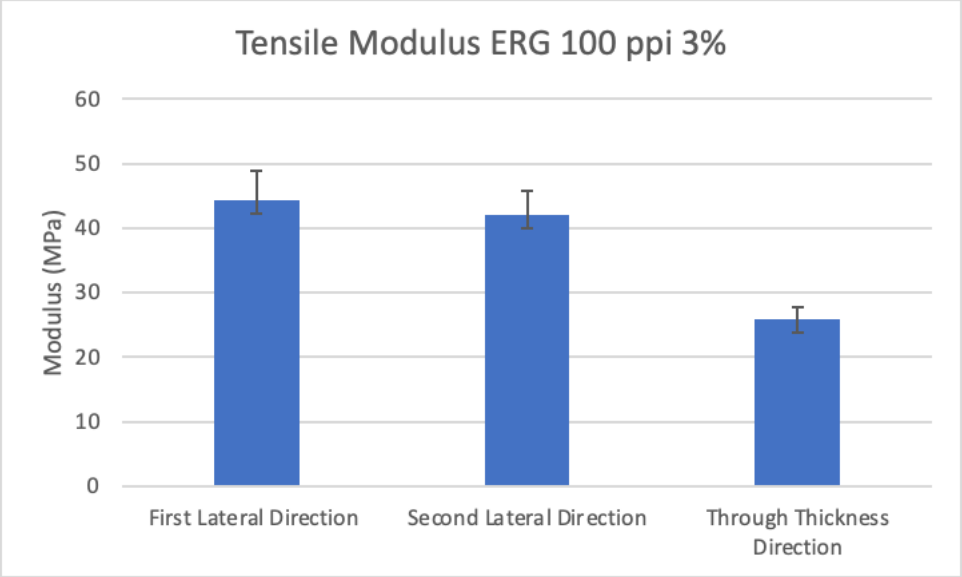

Figure 4-4 Tensile modulus of ERG 100 ppi 3%; the bars represent the mean value with the error bars indicating the standard deviation of each measurement

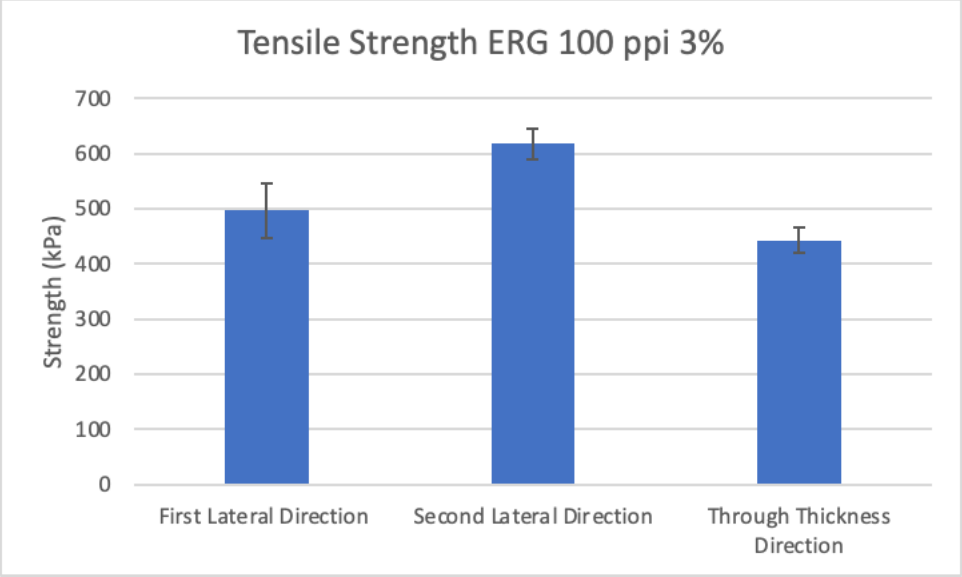

Figure 4-5 Tensile strength of ERG 100 ppi 3%; the bars represent the mean value with the error bars indicating the standard deviation of each measurement

4.2.2. Compression

Like the tension testing, the compression testing was performed at Touchstone Research Laboratory in Tridelphia, WV. The compression testing was performed using ASTM C365-11a, “Standard Method for Flatwise Compressive Properties of Sandwich Cores,” [67] The objective of the tests was to understand the ultimate strength and modulus in compression of the foams of interest in multiple loading directions. Figure 4-6 is the compression test set up for carbon foam.

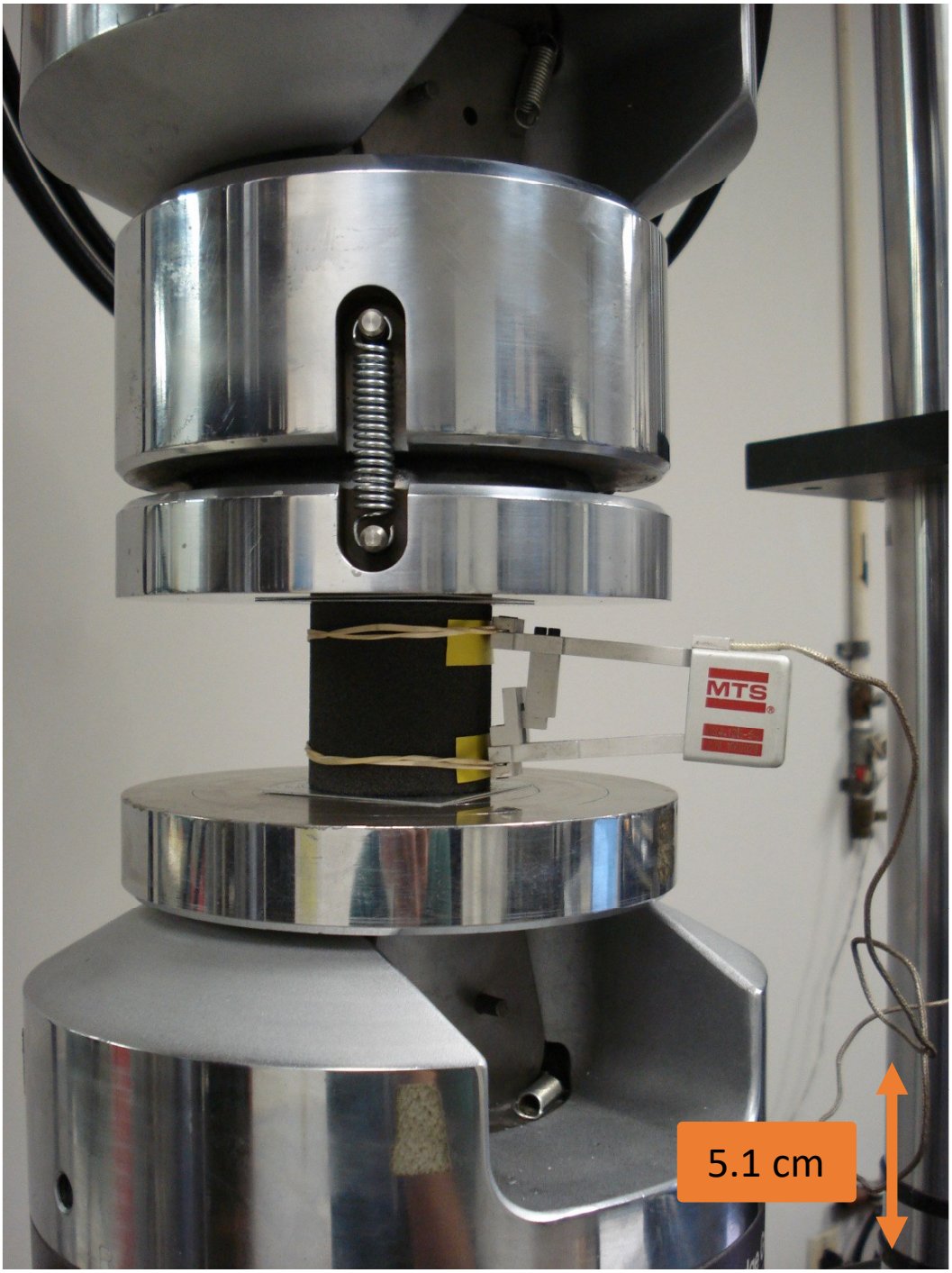

Figure 4-6 Compression testing of carbon foam [66]

Like the tensile coupons, this testing was performed on a United SFM-20 Electro-mechanical load frame with a 20,000 lbf capacity with spherical platens to adjust for any misalignment. Samples, like the tension coupons, were round and approximately 5.1 cm

in diameter and 5.1 cm long. The displacement of the sample was measured using a 2.54 cm gage length MTS 634.12E54 extensometer [64]. The samples were then placed between the platens and compressed with aluminum sheets. The initial test speed was 0.127 cm/min and the data acquisition rate was 10 Hz.

Like tension, ASTM C365 has requirements that the surface area must be at least 6.45 cm^2 area for the sample and a minimum of 60 cells. Since cell is equivalent to pores for this material and the specimen area was approximately $6.45\ cm^2$, the 40 pores per cm foam ensures that there are more than 60 cells or pores. Self-aligning platens were used to ensure that the loading was unidirectional through the compression tests. The only deviation from the test method was the use of an extensometer to measure displacement during testing. It is noted in the standard that bonded resistance strain gauges are usually not appropriate for this type of testing because their presence can add local stiffening to the sample. In order to bond strain gauges, adhesive would be infused into the foam over a large area of the sample. Given the attachment method, the strain gauge would likely be measuring the adhesive instead of the foam. The presence of extensometers were highly localized to the place that the knife edges touch the foam so did not have the same effect. However, the knife edges dug into the foam so to prevent this, vinyl tape was used on the foam where the extensometers were placed like in the tension tests. This vinyl tape is not infused into the foam and so only has a very local effect of keeping the extensometers in place and did not have an effect on the overall results. The foams tested were brittle in nature and Figure 4-7 shows an example of the stress/strain behavior.

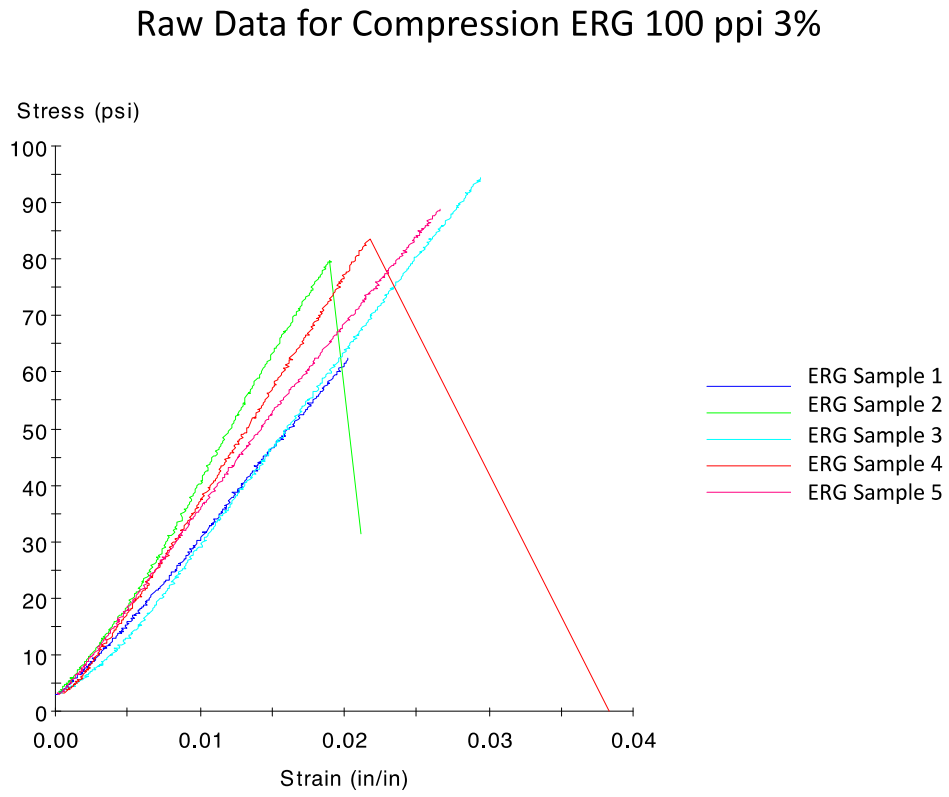

Figure 4-7 Raw data compression of ERG in the Second Lateral Direction [64]. The sudden drops in load indicated failure. Only some of the samples showed this drop in load in the raw data due to the settings for data acquisition system. This foam did not show densification during compressive loading.

The calculation of the ultimate strength and the modulus were straightforward. The compressive modulus is the slope of the loading curve and the ultimate compression strength is:

$$F_z^{fcu} = \frac{P_{max}}{A} \tag{16}$$

where:

$F_z^{fcu} = Ultimate\ Compressive\ Strength\ in\ z\ of\ the\ core$

$P_{max} = Maximum\ Force\ prior\ to\ Failure$

$A = Cross\ sectional\ area\ of\ the\ specimen$

The compressive ultimate strength and modulus were calculated for the carbon foam materials using these methods and the results for various foams and directions are discussed below. The compression testing data in the second lateral direction, a sample of which is shown in Figure 4-7, matches the linear-elastic until fracture behavior tensile results. Adding to the data from the tensile testing, Figure 4-8 and Figure 4-9 compare the modulus and strength of the ERG100 ppi 3% foam for this batch and are shown in Table 9.

Table 9 Comparison of tensile and compressive experiments for ERG 100 ppi 3% foam

	Strength (kPa)				Modulus (Mpa)			
	Tensile	Compression	Ten Std Dev	Com Std Dev	Tensile	Compression	Ten Std Dev	Com Std Dev
First Lateral Direction	497	582	50	83	44	34	5	7
Second Lateral Direction	618	564	28	84	42	26	4	4
Through Thickness Direction	443	545	22	81	26	19	2	3

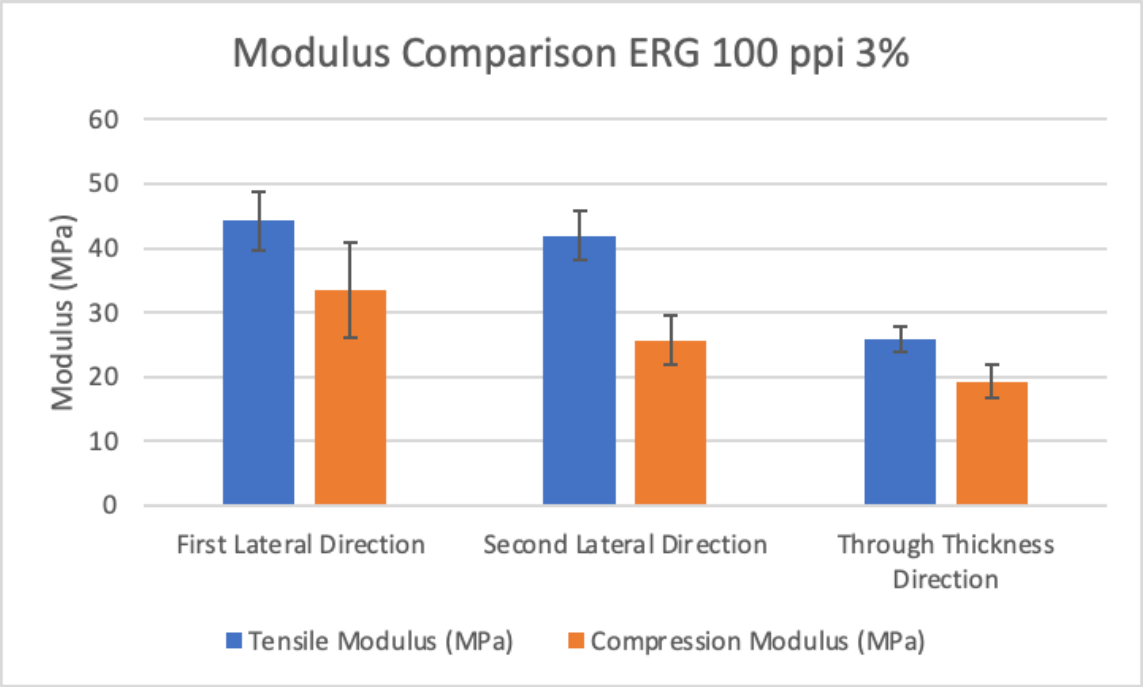

Figure 4-8 Comparison of modulus for ERG 100 ppi 3% in Tension and Compression; the bars represent the mean value with the error bars indicating the standard deviation of each measurement

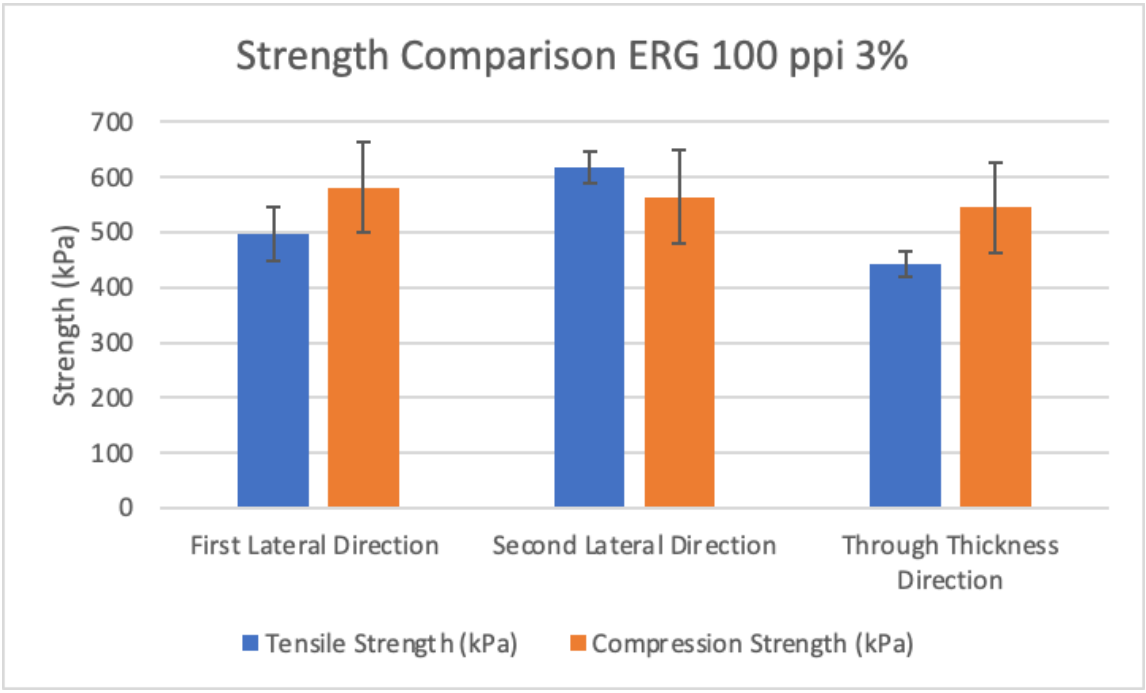

Figure 4-9 Comparison of strength for ERG 100 ppi 3% for Tension and Compression; the bars represent the mean value with the error bars indicating the standard deviation of each measurement

A disparity between the tensile and compressive results was expected as there were different failure mechanisms for the tension and compression loading. As Gibson and Ashby [23] note, in tension brittle foams fail by the propagation of the largest defect, often involving ligament breaking and “crack” propagation. Under compression, failure is manifested through brittle wall buckling and crushing [23]. Gibson and Ashby also note that brittle crushing in compression leads to densification, however densification was not seen in this foam. All the foams under study in this dissertation had low relative density of less than 10%. When these foams failed in compression, there was not enough material to densify and affect the results since the foam particles would break and fall through the specimen since it was porous. The volume of the sample was reduced but this material collected at the bottom of the specimen due to gravity. Figure 4-10 shows examples of broken foam pieces due to testing. Due to the porosity of the material, there was a fracture surface similar to what was seen in the tensile testing and no densification was seen in the stress/strain plots.

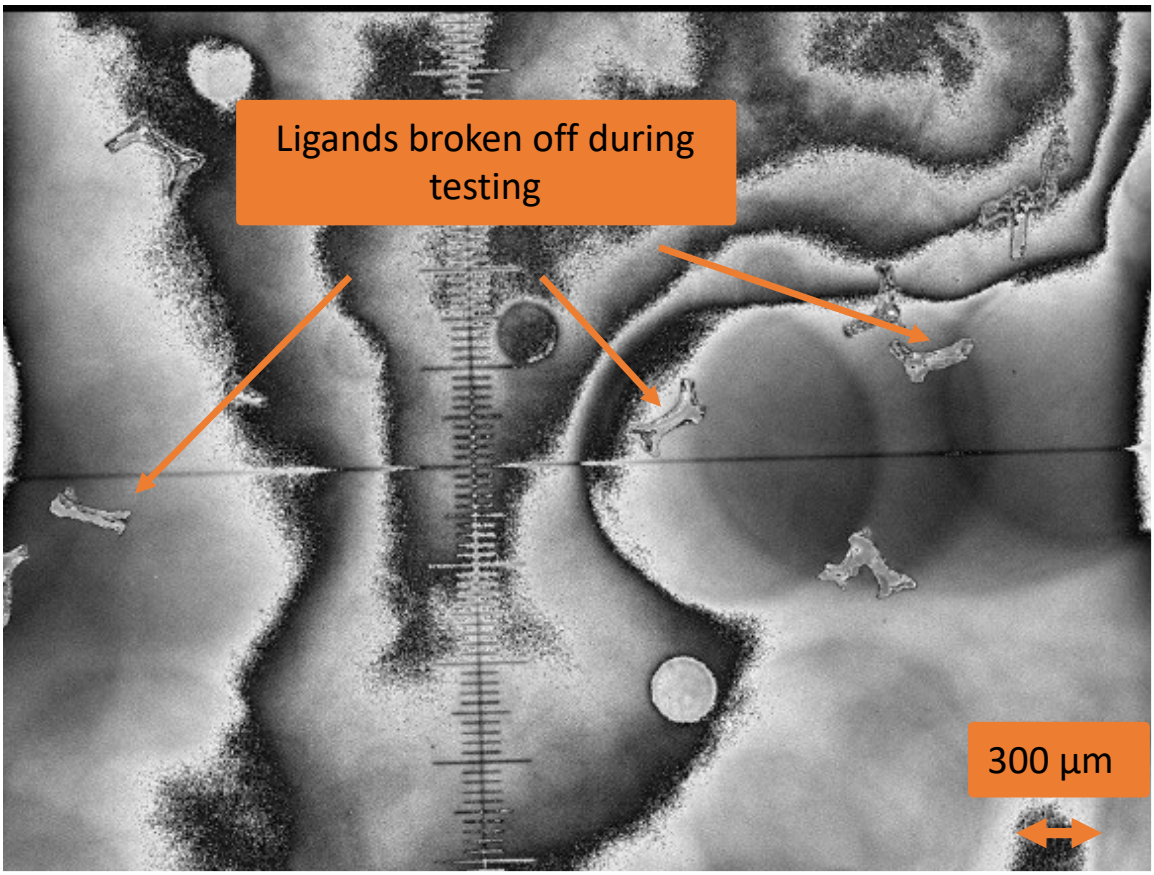

Figure 4-10 Ligands of foam that were broken off during testing. This picture was taken after a planned failure of a coupon in vibration testing.

4.2.3. Shear

Shear testing of the carbon foam was particularly difficult due to the delicacy of the foam. Traditional lap shear tests were tried in the early stages of the test program and found that proper failures, with a nice shear path between the ends, were difficult to obtain. Traditional lap shear tests can be difficult because the loading is off the primary axis of failure. This feature causes issues with more robust, dense samples that are exacerbated with foams. Additionally, the adhesive used to bond the thin samples to the test fixture soaks into the foam densifying it locally and thereby influencing the outcome of the test. After trying single lap shear and double lap shear tests, these

methods were abandoned and other test methods were considered. Touchstone Research Laboratory (TRL) had developed a torsional shear test for testing foams with similar density that they had developed in-house. The carbon foams for PSP were tested in this torsional shear manner with the objective of determining the peak stress and modulus of the foams in shear in the three primary axes. Figure 4-11 shows the torsional shear test setup which is on a custom-built TRL torsion tester.

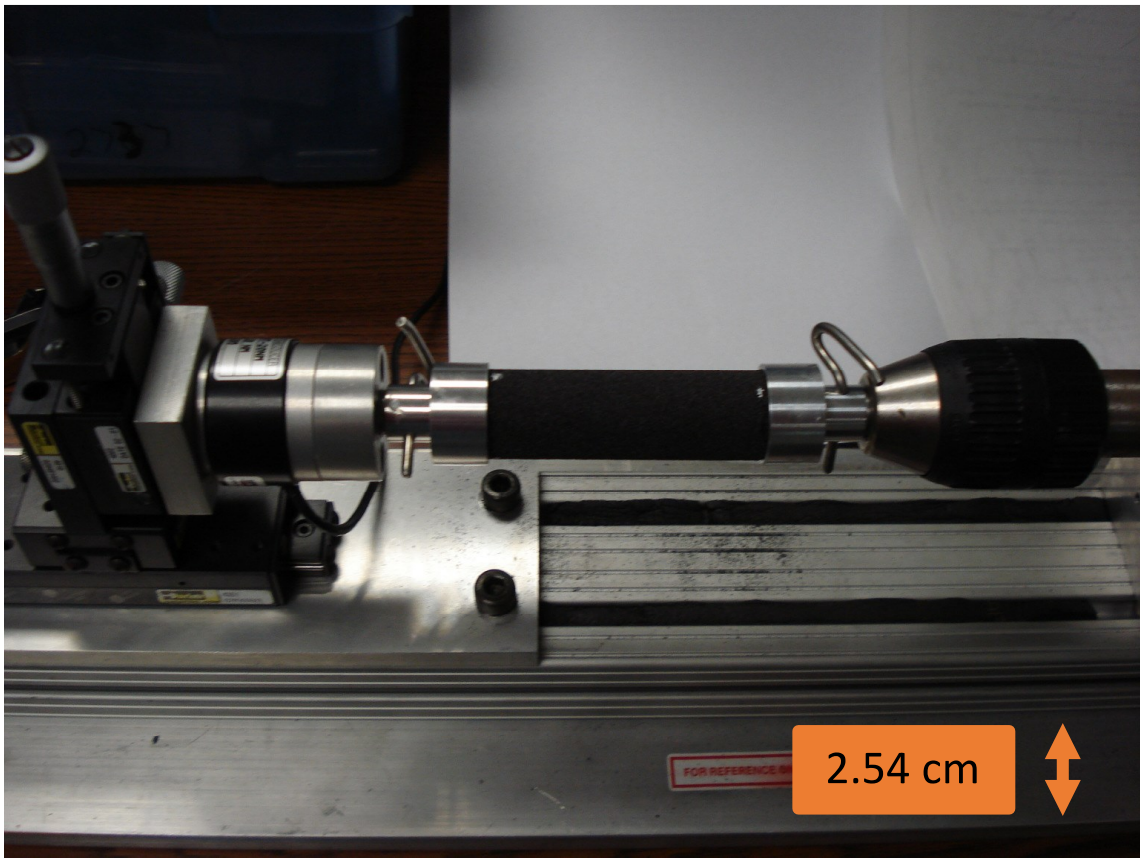

Figure 4-11 Shear testing of carbon foam at TRL [63]

The torsion samples were machined using the CNC to be 2.54 cm round and 12.7 cm long. The samples were bonded to the torsion testing tabs using the Locktite quick set epoxy. The torsion tester had an MRT-20NM torque cell that was used to measure the torque being applied to the sample. An Autonics E40H rotary encoder was used to

measure displacement. The initial test speed was 0.1 RPM and 10 specimens were tested for each material [64]. Figure 4-12 illustrates a picture of the foam that was used to develop this test, a mixed open/closed cell foam, compared to a picture of Ultramet 100 ppi 3% foam.

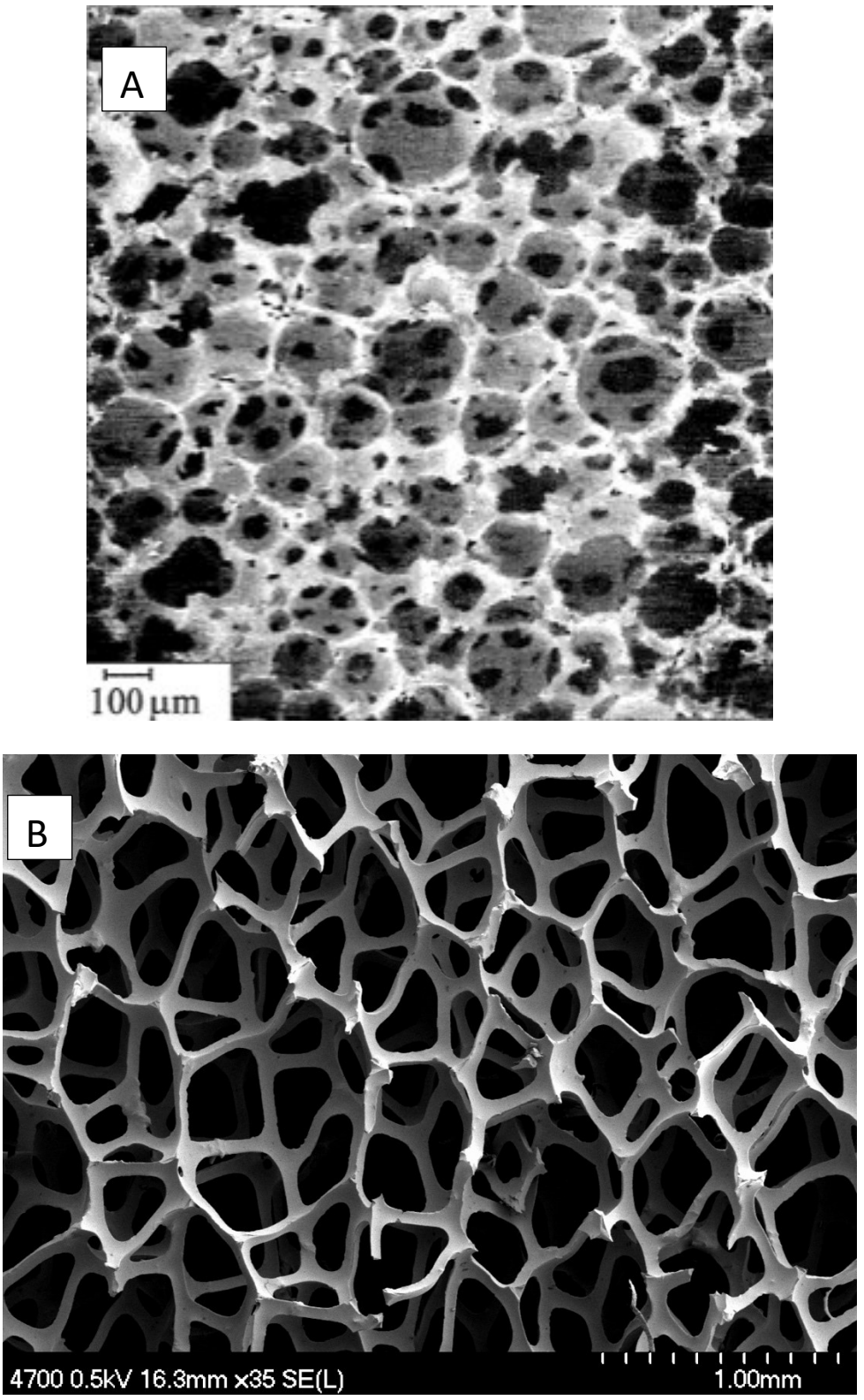

Figure 4-12 A: Picture of the graphic foam that was used to develop the torsional shear test [68], B: Picture of Ultramet 100 ppi 3% foam under study here (Courtesy of Ryan Deacon)

Roy and Camping, when describing this test set up, noted that traditional lap shear both double and single, labeled single and double rail shear in their paper, were attempted but the presence of the needed adhesive in the thin samples required for this testing introduced stress concentrations resulting in lower strengths and inconsistent results [68]. Early foam testing at JHUAPL attempted double lap shear testing of the carbon foam and the same issues made these early attempts unsuccessful. Roy and Camping also attempted to use Iosipescu shear testing, which requires relatively small samples to be outfitted with a V notch and then loaded with rolling pins. Given the point loading and small sample size, it was deemed inappropriate for the PSP carbon foam.

The thin rod test specimen was in the middle of the test set up with grip rods on either end allowing for torsional loading over a larger surface area, which is beneficial for the delicate carbon foam. The modulus was determined from the rotational displacement. As shown in Figure 4-13, the max shear loading and max shear strain occurs on the surface of the shaft and can be calculated for small displacements.

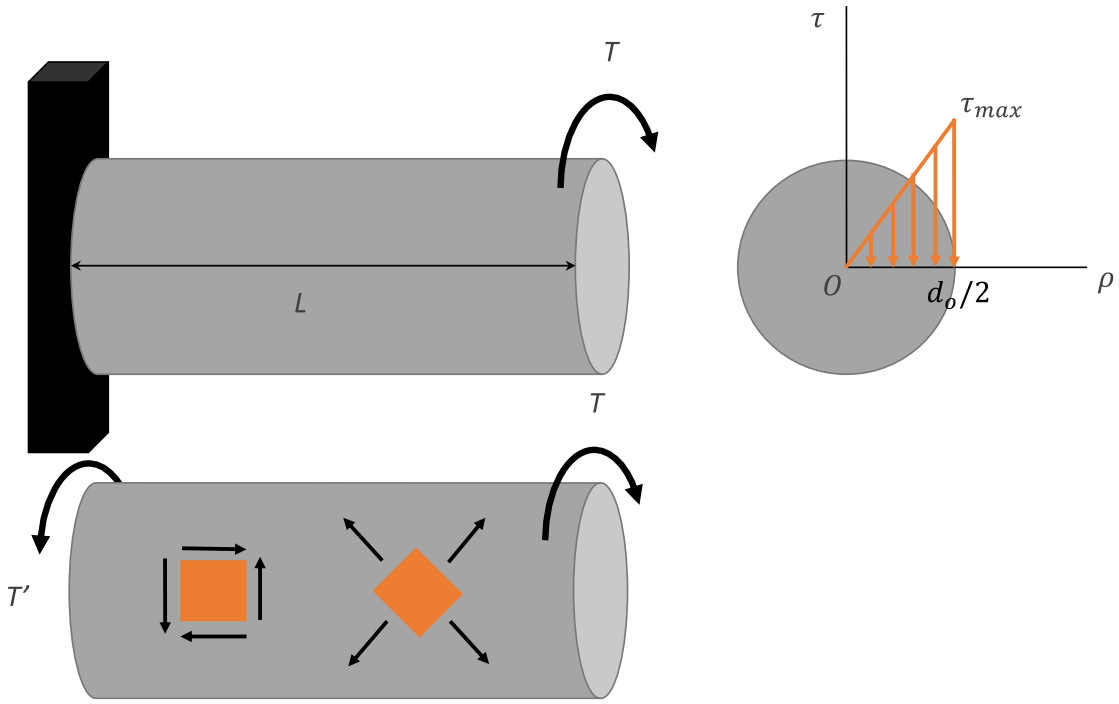

Figure 4-13 The free body diagrams for the torsional shear test adapted from [69]

The equation for shear modulus and shear strain were calculated from the displacements and change in torque which are noted in Eq. (17), Eq. (18) [68] and the maximum shear strength was calculated using Eq (19).

$$G = \frac{1}{J}\left(\frac{dT}{d\phi}\right)L \tag{17}$$

$G = Shear\ Modulus\ of\ the\ Material\ Under\ Test$

$T = applied\ torque$

$\phi = Rotation\ at\ the\ end\ of\ the\ material$

$J = Torsional\ Rigidity\ for\ a\ circular\ cross\ section = \pi\frac{d_o^4}{32}$

$d_o = outer\ diameter\ of\ the\ specimen$

$L = specimen\ gauge\ length$

$$\gamma_{max} = \frac{d_o}{2}\left(\frac{\phi}{L}\right) \tag{18}$$

$\gamma_{max} = maximum\ shear\ strain$

$d_o = outer\ diameter\ of\ the\ specimen$

$L = specimen\ gauge\ length$

$\phi = Rotation\ at\ the\ end\ of\ the\ material$

$$\tau_{max} = \frac{T d_o}{2J} \tag{19}$$

$\tau_{max} = maximum\ shear\ strain$

$T = applied\ torque$

$d_o = outer\ diameter\ of\ the\ specimen$

$J = Torsional\ Rigidity\ for\ a\ circular\ cross\ section = \pi\frac{d_o^4}{32}$

In addition to tensile and compression testing, shear testing was performed on the ERG 100 ppi 3% foam, a brittle material that was weaker in tension than in shear. Given these expectations, it was anticipated the failure in pure torsion would be along the line of maximum tension on the outer surface of the rod, which was at a 45° angle from the test axis. These samples failed in this appropriate and expected manner, an example is

shown in Figure 4-14. The shear test results for strength and modulus for the ERG 100 ppi 3% are summarized in Table 10, Figure 4-15 and Figure 4-16.

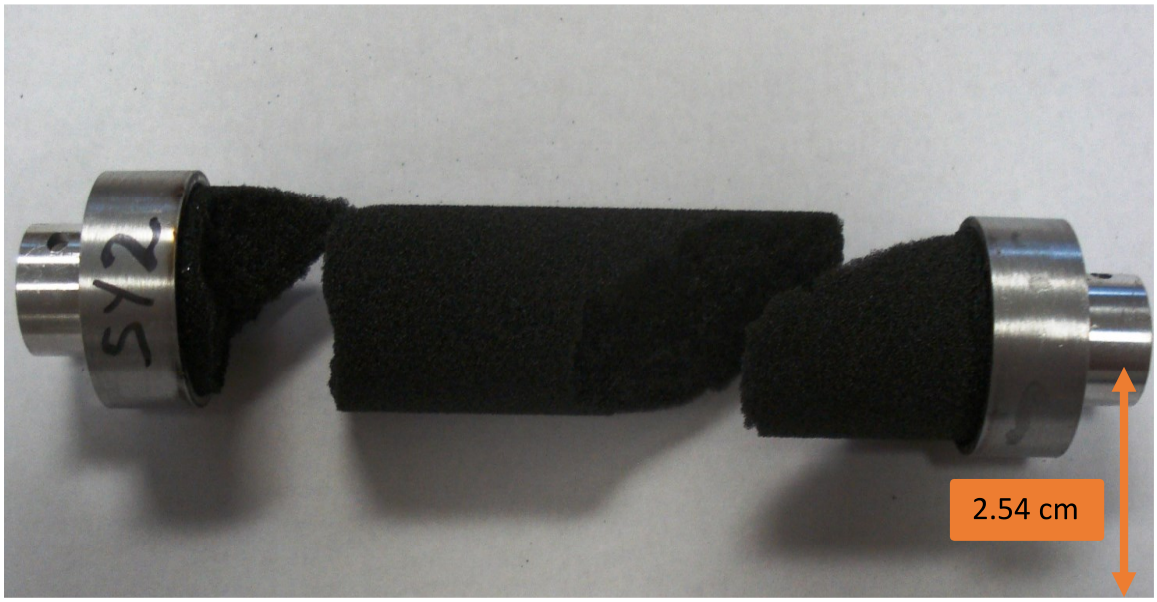

Figure 4-14 Example of the torsional shear failure, adapted from [70]

Table 10 Shear experimental results for one batch of ERG 100 ppi 3% foam

	Strength (kPa)	Std Dev	Modulus (MPa)	Std Dev
First Lateral Direction	429	25	15	1
Second Lateral Direction	433	25	14	1
Through Thickness Direction	388	30	12	1

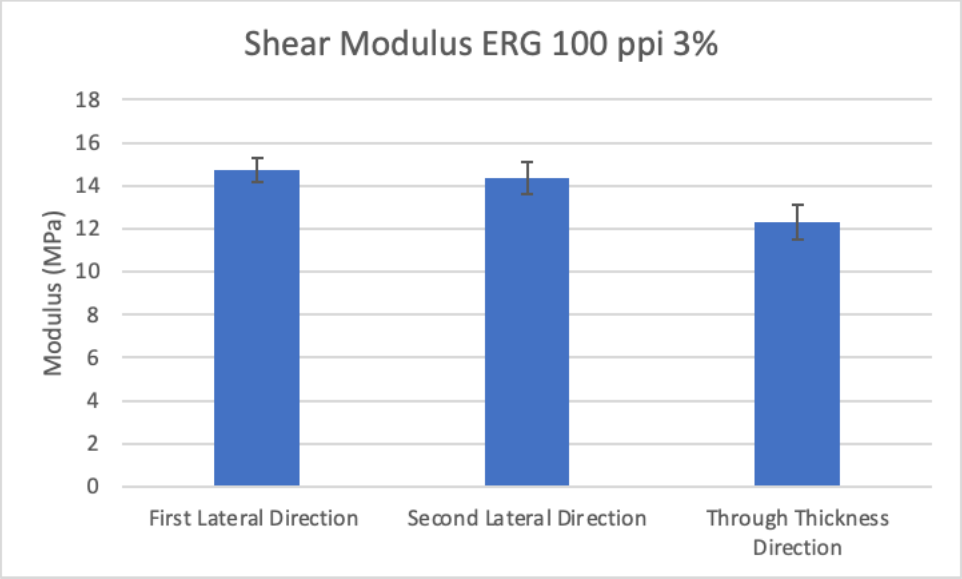

Figure 4-15 Shear modulus for the ERG 100 ppi 3%; the bars represent the mean value with the error bars indicating the standard deviation of each measurement

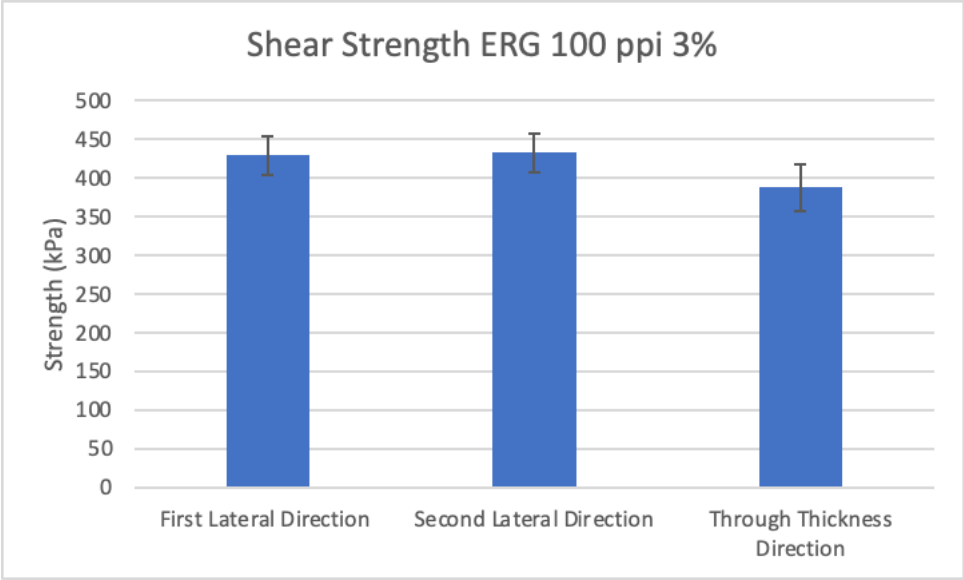

Figure 4-16 Shear strength of ERG 100 ppi 3%; the bars represent the mean value with the error bars indicating the standard deviation of each measurement

Assuming isotropy, which obviously has limitations for this material, a calculation of the tension load from this pure torsion loading can be calculated using Mohr's circle. Figure 4-13 shows the stress state throughout the round bar. The maximum shear stress is on the outer surface of the rod and Mohr's circle was used to compare this maximum

shear load to the tensile strength seen in the tensile coupon tests. Figure 4-17 depicts the expected shear load given failure in tension along the 45° angle from the test axis using Mohr's circle. Taking the lowest value that was recorded for compression in any direction (421 kPa) and recorded for tension in any direction (418 kPa), the calculated expected shear is 420 kPa. This number is consistent with the shear results shown in Table 10.

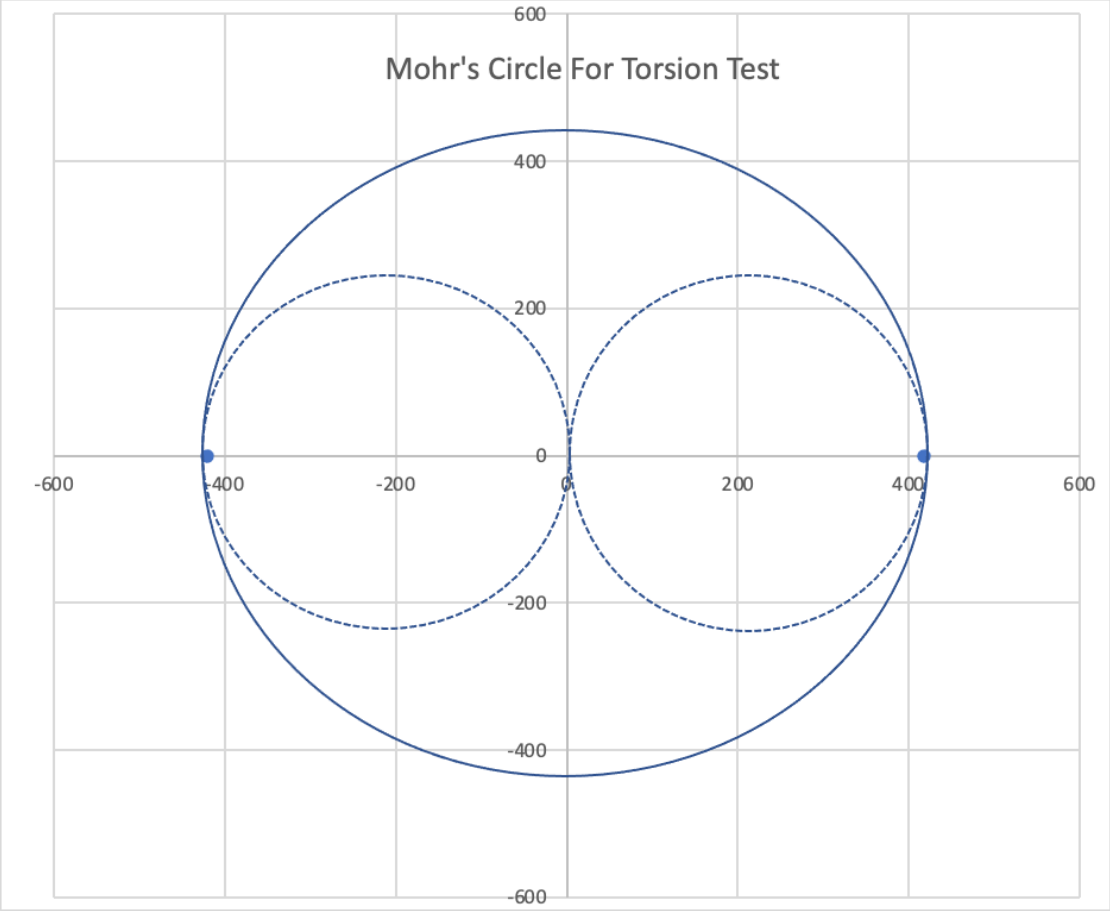

Figure 4-17 A Mohr's circle for the Torsion Test

4.2.4. Limitations of Testing

All the coupon level structural testing had similar limitations of testing. The foams are brittle, low density and low modulus. These factors mean that the foam is sensitive to point loading which was a loading condition often found in test setups for traditional testing approaches. These limitations meant that the standard test approaches needed to be modified or abandoned in favor of more appropriate testing approaches. If these limitations were not understood, testing could show extreme variation and low strength results establishing an inaccurate picture of the behavior of the foam. Despite the limitations, coupon testing provided a basis for observing and understanding the mechanics of the carbon foam. This detailed understanding was difficult to parse out at a higher level.

4.3. Discussion of Anisotropy

Gibson and Ashby [23] differentiated between structural anisotropy, driven by the geometric structure of the foam, and material anisotropy, driven by differences in material within the struts; they postulated that structural anisotropy was the key component in understanding material behavior of foams. All the foams studied for this dissertation displayed anisotropy in tension and compression in the primary directions, however the structural geometric anisotropy was not visually apparent in the foams as shown in Figure 4-22. Ultramet 100 ppi 3% data was used to explore the validity of the anisotropic Gibson and Ashby equations. Data from a representative batch of Ultramet 100 ppi 3%, where all the coupons were taken from the same block of foam, is

summarized in Figure 4-18 through Figure 4-21 and Table 11 and Table 12. The error bars show the standard deviation for each data set.

Table 11 Compression and tension experimental data for one batch of Ultramet 100 ppi 3%

	Strength (kPa)				Modulus (Mpa)			
	Tensile	Compression	Ten Std Dev	Com Std Dev	Tensile	Compression	Ten Std Dev	Com Std Dev
First Lateral Direction	516	367	68	75	62	44	2	5
Second Lateral Direction	597	553	34	92	78	55	12	7
Through Thickness Direction	371	313	29	47	24	9	3	1

Table 12 Shear experimental data for one batch of Ultramet 100 ppi 3%

	Strength (kPa)	Std Dev	Modulus (MPa)	Std Dev
First Lateral Direction	361	33	13	1
Second Lateral Direction	375	23	12	1
Through Thickness Direction	323	19	11	1

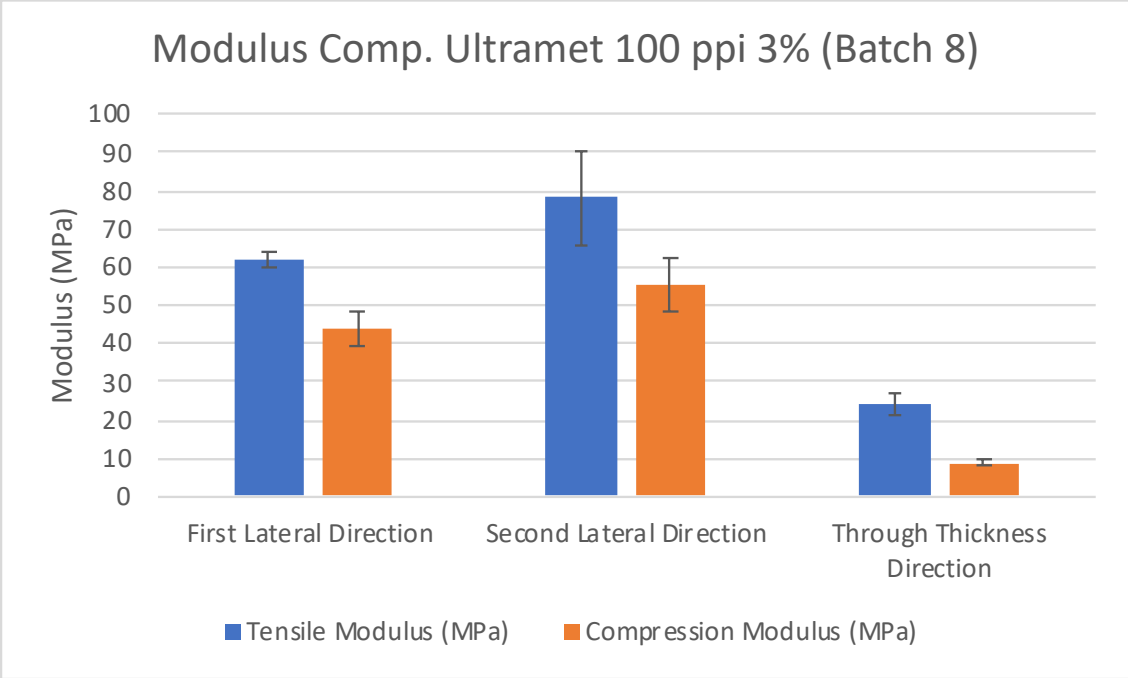

Figure 4-18 Comparing the tensile and compressive modulus of Ultramet 100 ppi 3% foam in three primary axes; the bars represent the mean value with the error bars indicating the standard deviation of each measurement.

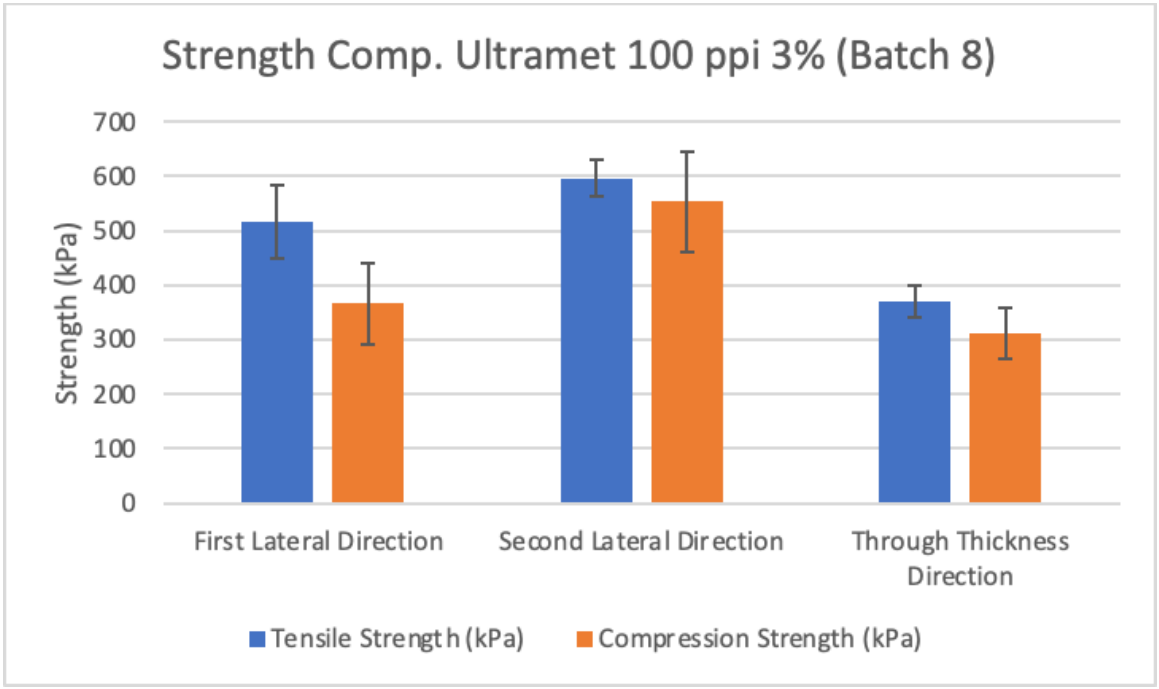

Figure 4-19 Comparing the tensile and compressive strength of Ultramet 100 ppi 3% foam in three primary axes; the bars represent the mean value with the error bars indicating the standard deviation of each measurement.

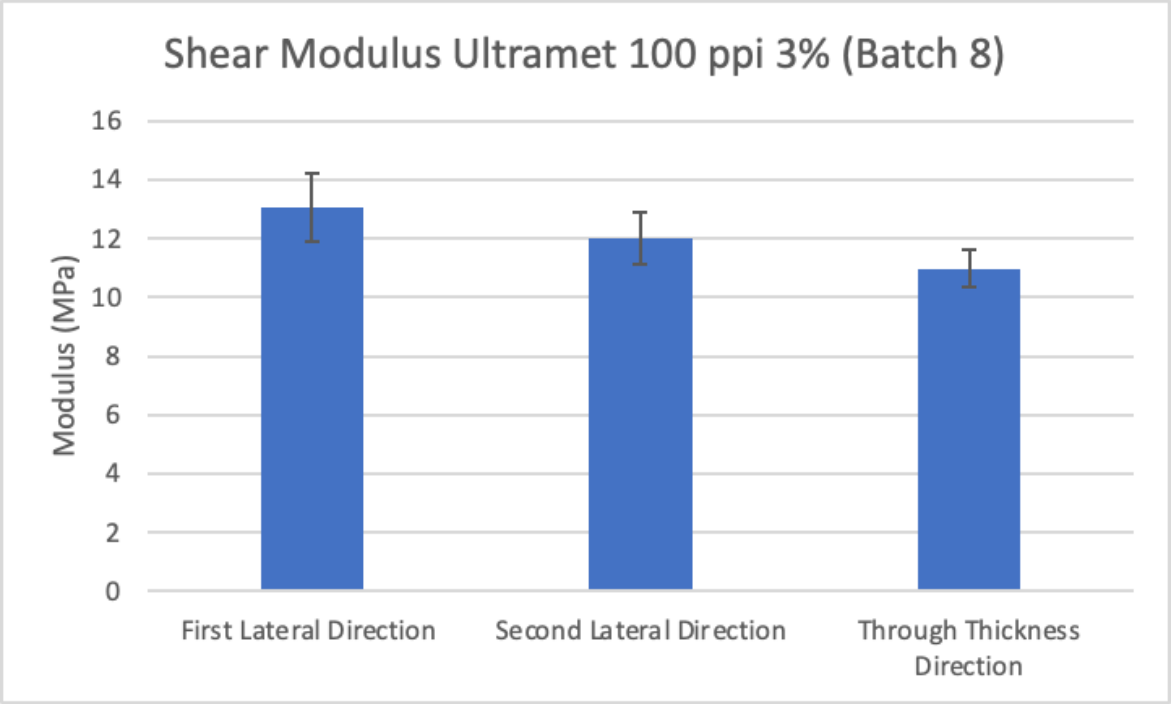

Figure 4-20 Comparing shear modulus of Ultramet 100 ppi 3% foam in three primary axes; the bars represent the mean value with the error bars indicating the standard deviation of each measurement

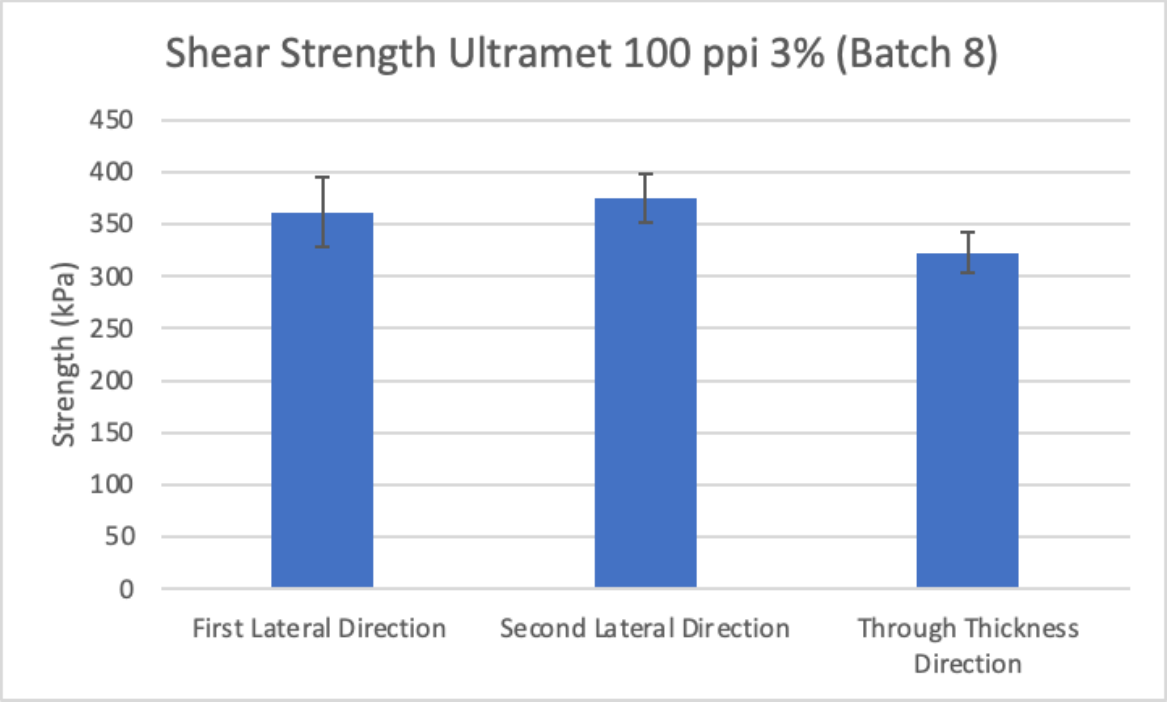

Figure 4-21 Comparing shear strength of Ultramet 100 ppi 3% foam in three primary axes; the bars represent the mean value with the error bars indicating the standard deviation of each measurement

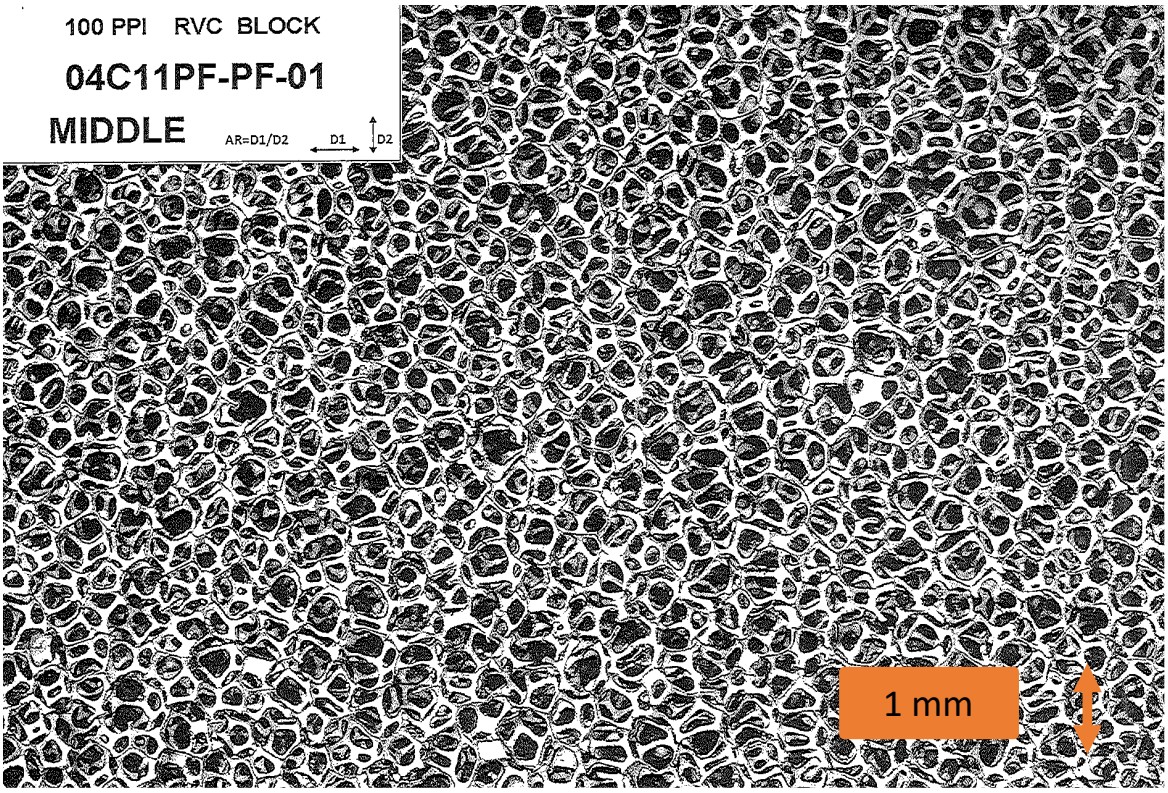

Figure 4-22 Ultramet 100 ppi 3% batch variability sample from Batch 8

To examine the structural anisotropy, each batch of foam was measured by taking a slice of foam in each direction and the range of the ratio between the lengths of the cell walls, *R*, was catalogued. One of these foam slices for the Ultramet 100 ppi 3% Batch 8 is shown in Figure 4-22. The Ultramet 100 ppi 3% foam for this batch had a measured range of $0.85 \leq R \leq 1.2$ and there was a range of $0.7 \leq R \leq 1.2$ for all batches. As displayed in Figure 4-22, this structural anisotropy was not consistent throughout the foam. These ratios were treated as a range of values and the Gibson and Ashby anisotropy was calculated. Eq (6) and (7) relate the structural anisotropy derived from measured differences in length in the cell geometry to elastic and shear moduli. This structural asymmetry is represented by *R,* the ratio between the height and length of a

cell. Table 13 tabulates possible ratios of elastic and shear moduli based on *R* and compares those values with the test data.

$$\frac{E_3^*}{E_1^*} = \frac{2R^2}{\left(1 + \left(\frac{1}{R}\right)^3\right)} \tag{7}$$

$$\frac{G_{31}^*}{G_{12}^*} = \frac{2}{(1+R)} \tag{8}$$

Table 13 Gibson and Ashby anisotropy equations compared to test data for Ultramet 100 ppi 3%

		Possible R Values					
Gibson and Ashby Eq	**Exp. Data**	**0.7**	**0.8**	**0.9**	**1**	**1.1**	**1.2**
$\frac{E_3^*}{E_1^*}$	0.58	0.25	0.43	0.68	1.00	1.38	1.82
$\frac{G_{31}^*}{G_{12}^*}$	0.86	1.18	1.11	1.05	1.00	0.95	0.91

The shear modulus was more tolerant of the structural cell anisotropy than the Young's modulus as predicted by the Gibson and Ashby equations and seen in the test data. Based on the Ultramet 100 ppi 3% data, the experiment data calculated a $\frac{G_{31}^*}{G_{12}^*} = 0.86$; however, the G+A model predicted possible values between 0.91-1.18 for the

shear modulus ratio due to structural anisotropy. Therefore, the Gibson and Ashby anisotropic model did not match the test data suggesting that the anisotropy in material properties was not purely driven by structural geometric anisotropy for this foam. This inconsistency could have been due to material anisotropy in the foam struts and the fact that the foam was not a perfectly idealized mathematical periodic structure which both are driven by the real-world effects from manufacturing. Consequently, modeling with limited test data could not be solely used to understand the material properties of the foam; instead, an extensive test program in multiple directions and loading conditions was undertaken.

4.4. Subscale Testing Program

Structural testing on the subscale and full-scale level occurred throughout the PSP program and was developed to validate the behavior of the system under more complex loading conditions. Subscale testing developed for the PSP TPS included hydrostatic testing of the carbon foam, large scale four-point beam testing of the TPS sandwich panel, beam fatigue testing of the TPS sandwich panel and beam fracture testing of the carbon foam. These tests were designed to understand the behavior of the foam and the whole TPS system on a variety of scales. The hydrostatic testing and beam fatigue testing are not investigated in detail as part of this dissertation but they are described briefly below to provide context to the whole foam test program. Figure 4-23 through Figure 4-25 show the hydrostatic test setup and sandwich fatigue test set ups.

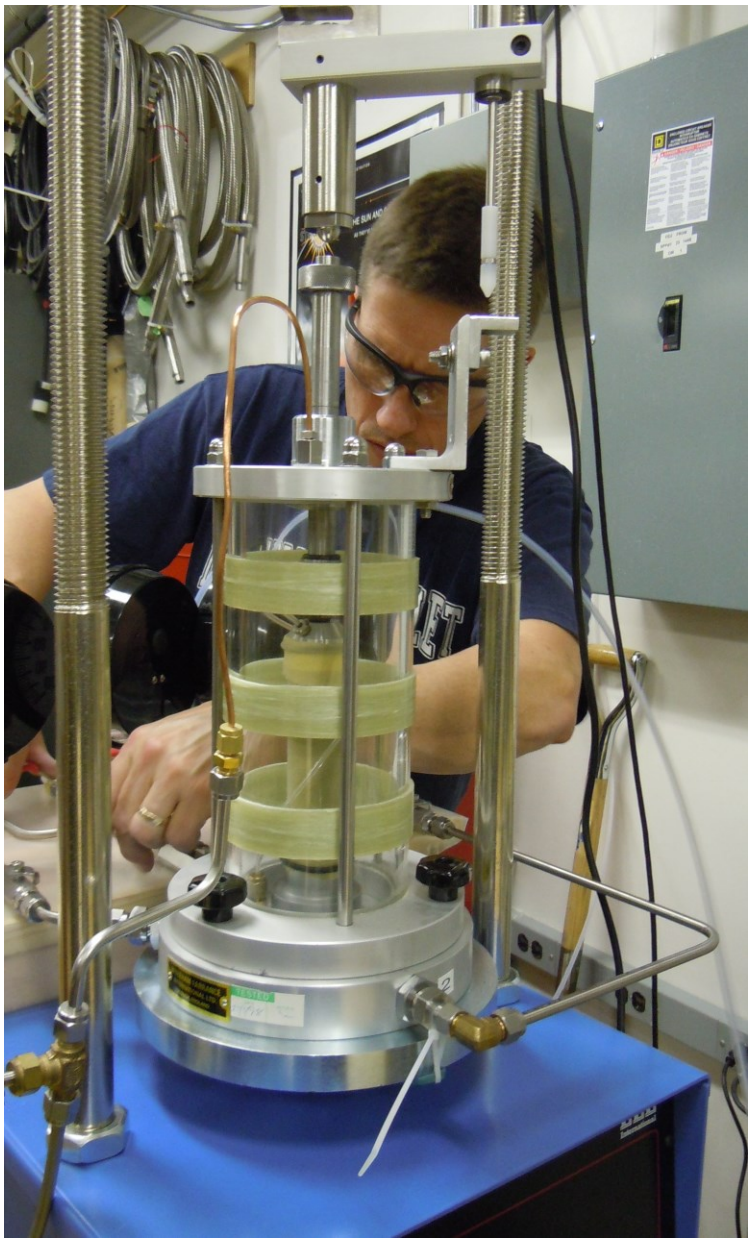

Figure 4-23 Hydrostatic test set up at JHUAPL which was used to hydrostatically load the foam with water and then apply a compressive force in the perpendicular direction.

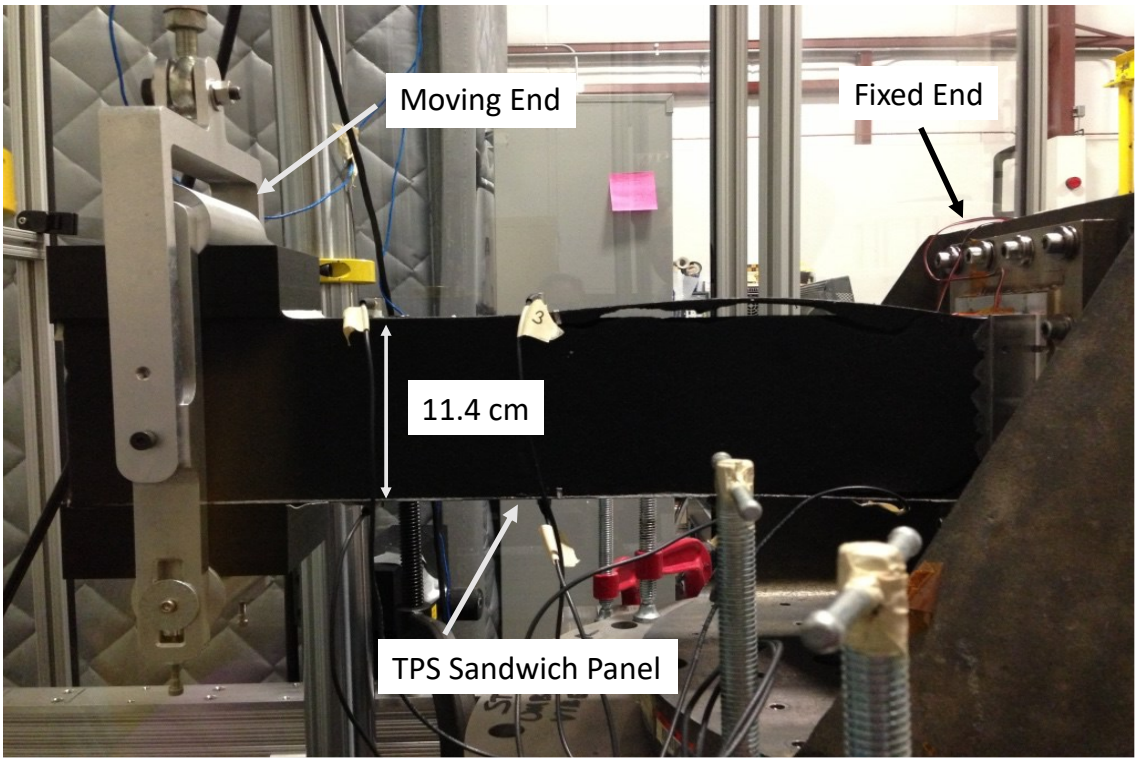

Figure 4-24 Fatigue test set up at JHUAPL is shown. A TPS sandwich panel was loaded dynamically with a small displacement to determine fatigue life.

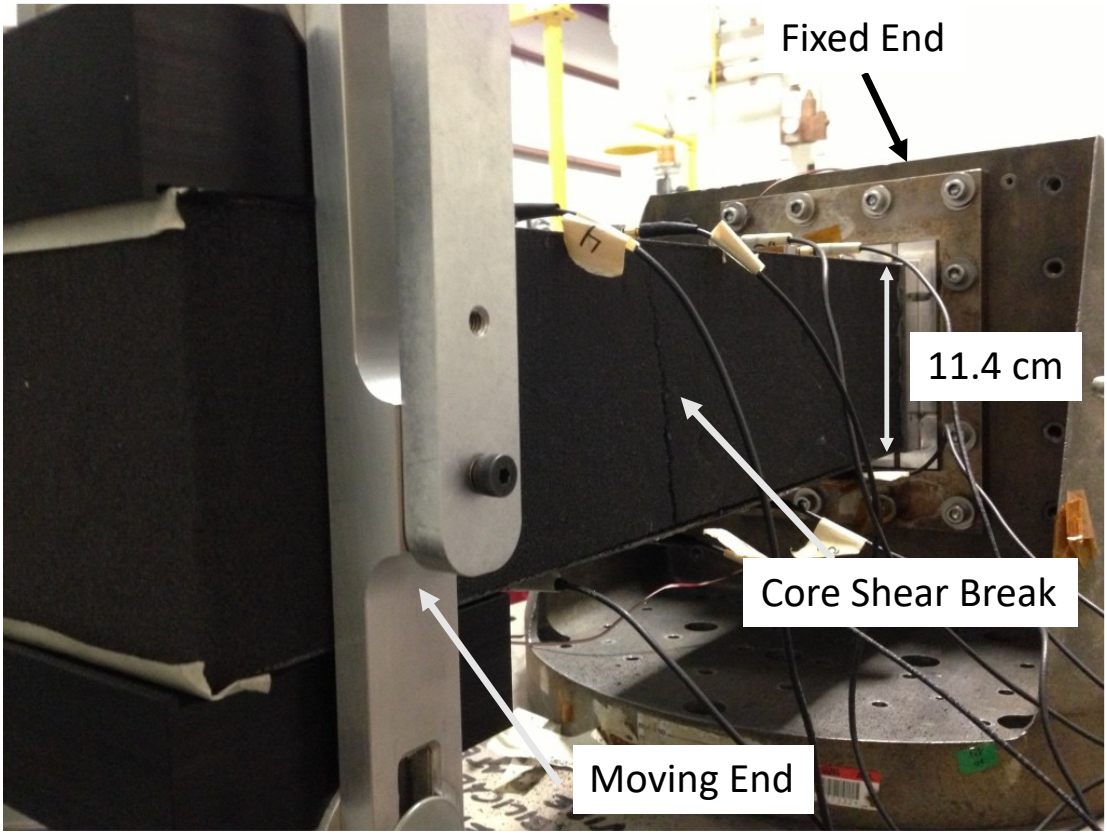

Figure 4-25 Valid failure in fatigue testing is shown with core shear failure clearly displayed.

The hydrostatic testing, developed at JHUAPL, was designed to understand the behavior of the foam under multi-axial loading. Paired with biaxial coupon testing, which was not discussed in this dissertation and was performed at TRL, the brittle foam failure loads under multiaxial loading were understood. The biaxial coupon testing and the hydrostatic testing were performed on specimens on the order of 15 cm long. Additionally, fatigue beam tests were developed at JHUAPL to understand the behavior of the sandwich panel during fatigue driven by flexure of the heat shield from thermal and dynamic launch loading. The fatigue test setup on a dynamic Instron is shown in Figure 4-24.

The fatigue test set up went through multiple iterations. The objective of the test was to understand the fatigue life of a bonded foam sandwich panel with facesheets. As shown in Figure 4-24, the test article was a slice of the full-scale heat shield with the proper foam thickness of 11.4 cm. The fatigue test set up has a fixed end (right) and the moving end is moved up and down with a roller and spreader bar distributing the applied load to the end of the beam. It was difficult to get valid failures during this test due to the stress concentration on the fixed end of the beam. Figure 4-25 shows a beam with a valid core shear break in the foam after being loaded in this shear testing. In general, subscale testing was used to bridge the gap between coupon testing and full-scale testing to understand the behavior of the foam. As a detailed example for this dissertation, the fracture toughness testing will be discussed in detail in the next section.

4.5. Fracture Toughness Test Set up

The subscale testing that will be examined in detail in this dissertation is fracture toughness testing. These fracture toughness tests were contracted by JHUAPL to TRL. Two versions of fracture toughness were performed: notched and unnotched. The unnotched version will be discussed below. Both tests were conducted on 53.3 cm by 5 cm by 10.2 cm samples Ultramet 100 ppi 3% carbon foam that were placed in the three-point bend setup as shown in Figure 4-26.

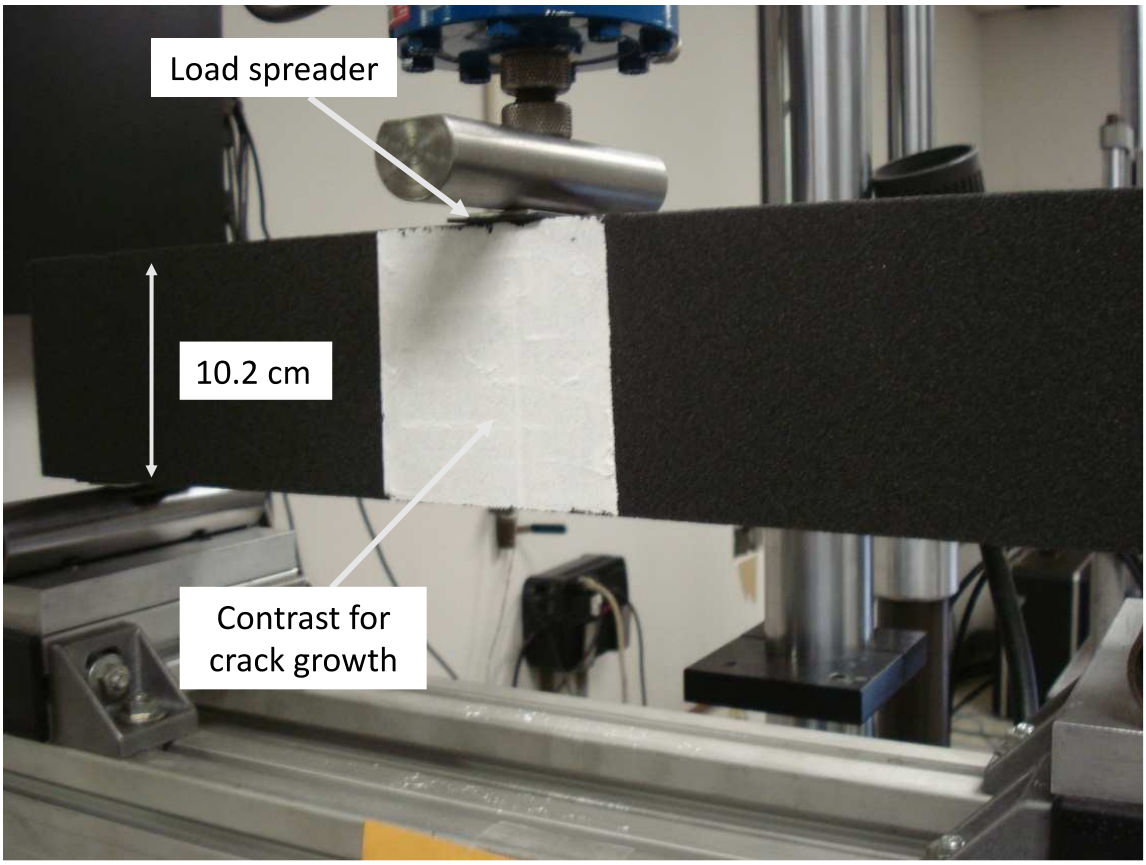

Figure 4-26 Three-point bend setup for a solid beam [71]

For this test, the support span was 45.7 cm. The tests were performed on an MTS 312.21 loading frame using a custom built three-point bend loading frame per ASTM E399, Standard Test Method for Linear-Elastic Plane-Strain Fracture Toughness K_{Ic} for Metallic Materials. Testing was performed at a speed of 0.127 cm/min. As shown in the figure, a piece of 0.15 cm aluminum sheet approximately 2 cm in length was placed below the loading rod to spread the load on the foam. The foam was brittle and sensitive to point loading so this load spreader was necessary for a valid failure. Additionally, white paint was used to highlight the area for the progressive crack.

4.6. Fracture Toughness Results and Discussion

The test was effectively a three-point bend test for the Ultramet 100 ppi 3% foam, the results of which could be compared to the coupon test data. Figure 4-27 shows the moment diagram for the three-point bend test. Using the maximum moment and the section modulus, a maximum normal stress in the beam can be calculated using Eq (20) through Eq. (22). Using these equations, the maximum predicted stress was calculated and compared to the three-point bend test results. Table 14 displays these calculations.

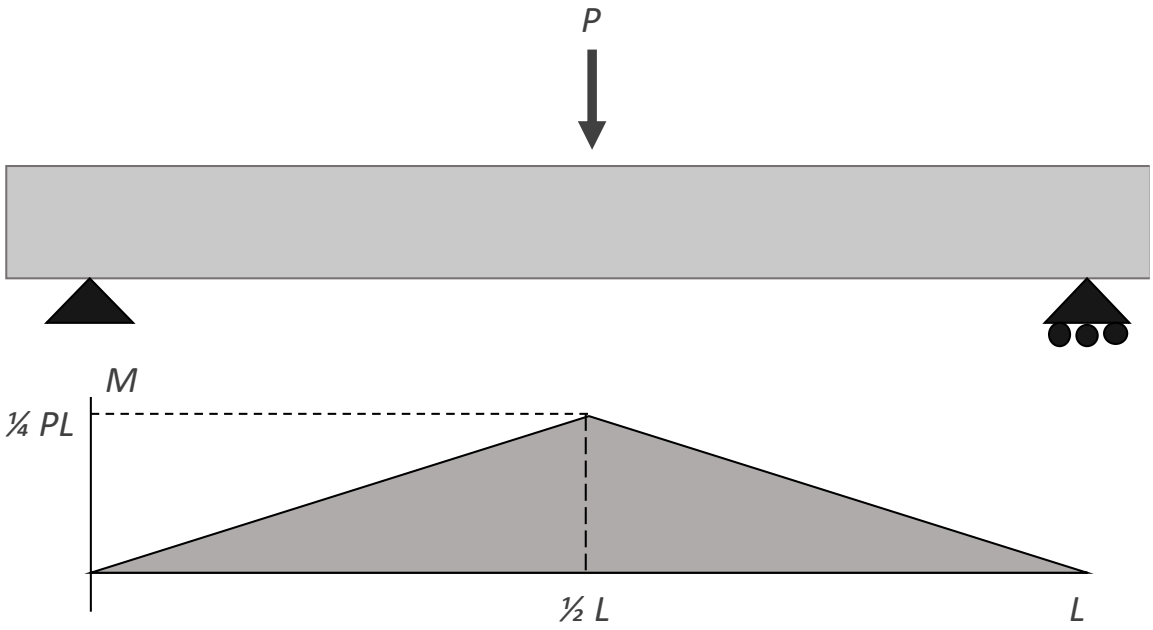

Figure 4-27 Three-point bend test moment diagram. Adapted from [69]

$$|M| = \frac{1}{4}PL \tag{20}$$

Where:

$M = Maximum\ moment$

$P = Maximum\ Load$

$L = Span\ Length$

$$S = \frac{1}{6}bh^2 \quad (21)$$

Where:

$S = Section\ modulus$

$b = width\ of\ the\ beam$

$h = height\ of\ the\ beam$

$$\sigma = \frac{|M|}{S} \quad \textbf{(22)}$$

Table 14 Three-point bend test results calculations

	Load (N) ***(Test data)*** ***[64]***	**Max Moment (Nm)** ***(Calculated)***	**Section Modulus (m^3)** ***(Test Unit Property)***	**Max Normal Stress (kPa)** ***(Calculated)***
	503	57	8.74E-05	657
	437	50	8.74E-05	572
	419	48	8.74E-05	548
Mean	453			592
Std Dev	44			58
CoV	0.10			0.10

The calculated maximum normal stress was compared with the strength of the material as measured with coupon tests. The appropriate data for comparison, the tensile strength of the foam in the lateral direction, can be found in Table 11. The data from this three-point bend test was consistent with the coupon data. The three-point data was on the higher end of the data range and the covariance was smaller than the coupon data. The volume of high stress in the bend test was more localized due to the nature of the loading profile compared to the loading profile in the tensile coupon tests. This smaller volume translated to a smaller volume for the distribution of failure starters in the three-point bend test versus the coupon testing; therefore, even though the subscale unit was a larger sample, it acted as a smaller volume for brittle failure.

4.7. Summary of Full-Scale Testing

Unlike the thermal testing, full-scale structural testing of the PSP heat shield was possible. In general, these full-scale tests mimicked launch loads and the objectives of these tests were to prove that the structurally integral insulation heat shield design would survive these loads. One such test was the full-scale compression test. This test was originally developed to simulate the load imparted by spacecraft separation from the launch vehicle thereby validating the design against the requirement to show that the system could withstand a 30 g-force compressive load without failing. This gravitational force equivalent is a unit of force per unit mass. As such, the goal was to load the TPS evenly with a 30 g compressive force which equated to 1407.5 kg statically. After exploring options such as using water or sand, printer paper was ultimately chosen to provide the distributed load as shown in Figure 4-28.

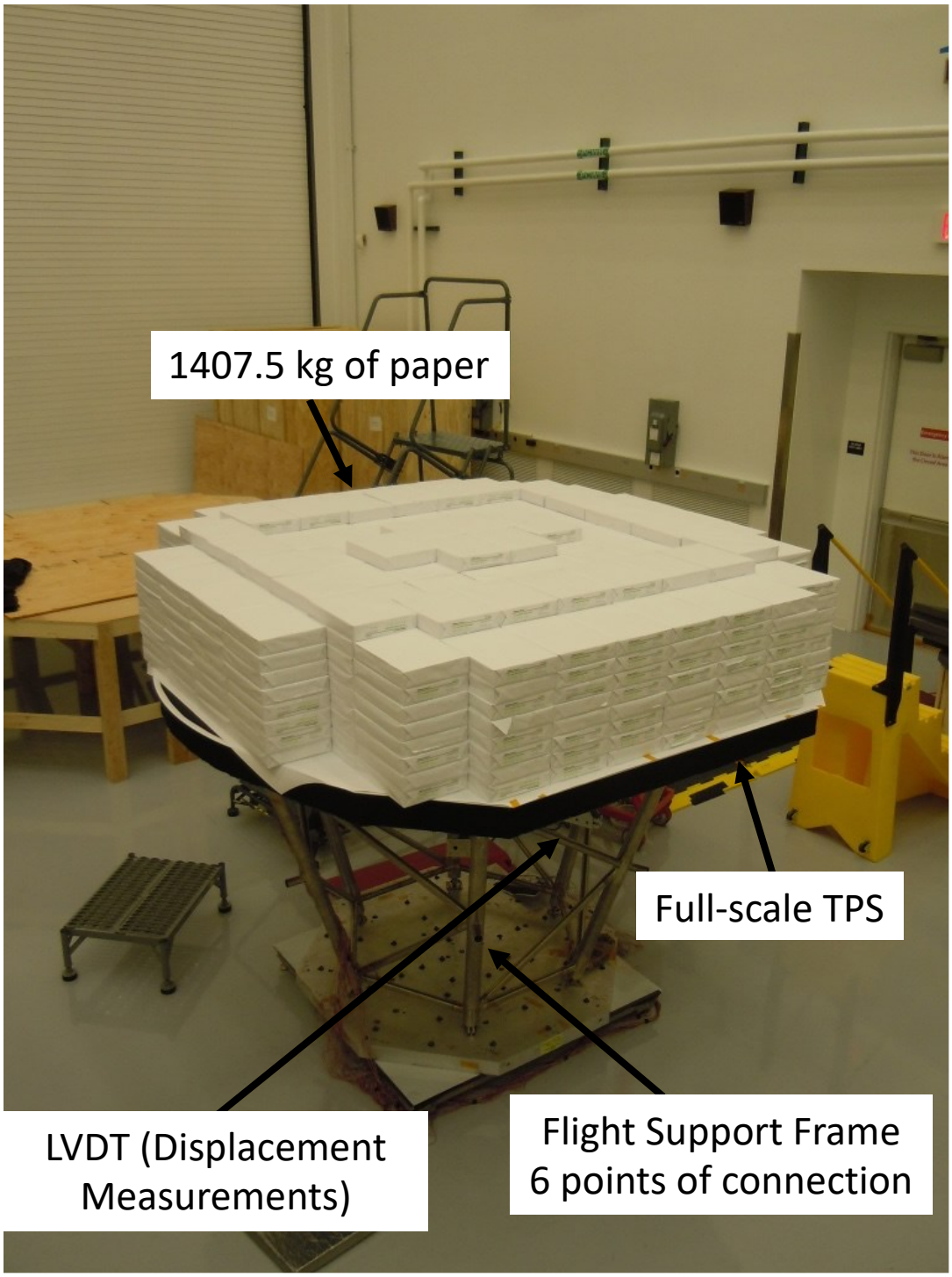

Figure 4-28 Compression (30 g) loading test at JHUAPL

For this test, 1407.5 kg of paper was placed evenly on top of the full-scale TPS. The heat shield was connected to the spacecraft at six points through a titanium truss

structure shown in the figure. The titanium truss structure that the heat shield was sitting on is the configuration used on the spacecraft. There was a spherical bearing at each of the 6 points which allows for thermal expansion when the system gets close to the Sun. For the full-scale testing under discussion here, the heat shield was placed in this flight-like configuration and loaded from the top.

Originally, water was thought to be the easiest way to achieve uniform loading. However, water was determined to be messy and difficult to execute. Therefore, the concept of using paper as a loading medium was adopted. Paper presented a nice option because each ream of paper was a well-defined weight and could be laid out in small chunks to slowly build up the overall mass. A protective piece of rubber the size of the full-scale unit was placed on top of the TPS coating. Then the paper was distributed around the TPS in layers to ensure that it was uniformly loaded. During this testing, a Linear Variable Differential Transformer (LVDT) placed in the middle of the full-scale unit was used to measure the displacement of the heat shield under loading. This displacement was monitored as the paper was being loaded and held under static loading.

This testing loaded the full-scale unit in a 30 g static load test to show survivability of the unit to this type of loading. Moreover, the displacement data could be compared to coupon level tests to understand the scale factors present in the behavior of the foam. The main limitation of this testing is the exact placement of the LDVT. While it was measured to be in the middle of the test set up, on this scale the precision of that measurement is limited.

4.8. Full-Scale Testing Results and Discussion

The ultimate validation of the structural design was the successful completion of full-scale vibration and acoustic testing on four TPS units. The coupon and subscale testing were used to develop the material properties used in the full-scale modeling of the PSP TPS. In order to ensure mission success, these strength values were prepared into limit values for the material properties. These numbers were a fraction of the raw strength values and dependent upon the number of samples tested and the variability of the data. The safety factors were determined based on the covariance of the data and probability of failure [72]. Subsequently, the stresses in the model were compared to the limit values, which were lower than the mean strength values from testing. Additionally, factors of safety were used to ensure the loading expected from the launch and thermal environments throughout the mission were well below the capabilities of the material. This approach meant that full-scale testing was conducted as a pass/fail verification of the design and modeling effort. The design was conservative and there was no expectation of failure.

Four full scale TPS units underwent vibration and acoustic testing to simulate the loads that the structure would experience during launch. Figure 4-29 is a picture of the vibration test on the first full scale unit in the Z axis of the spacecraft. This vibration testing was performed distinctly on the spacecraft three primary axes and the acoustic testing was performed separately at Goddard Space Flight Center (GSFC). The units were instrumented with accelerometers and this data was reviewed throughout testing. The

consistency of this data through the test campaign verified the integrity of the full scale units and verified that the flight unit was ready for launch [9, 72].

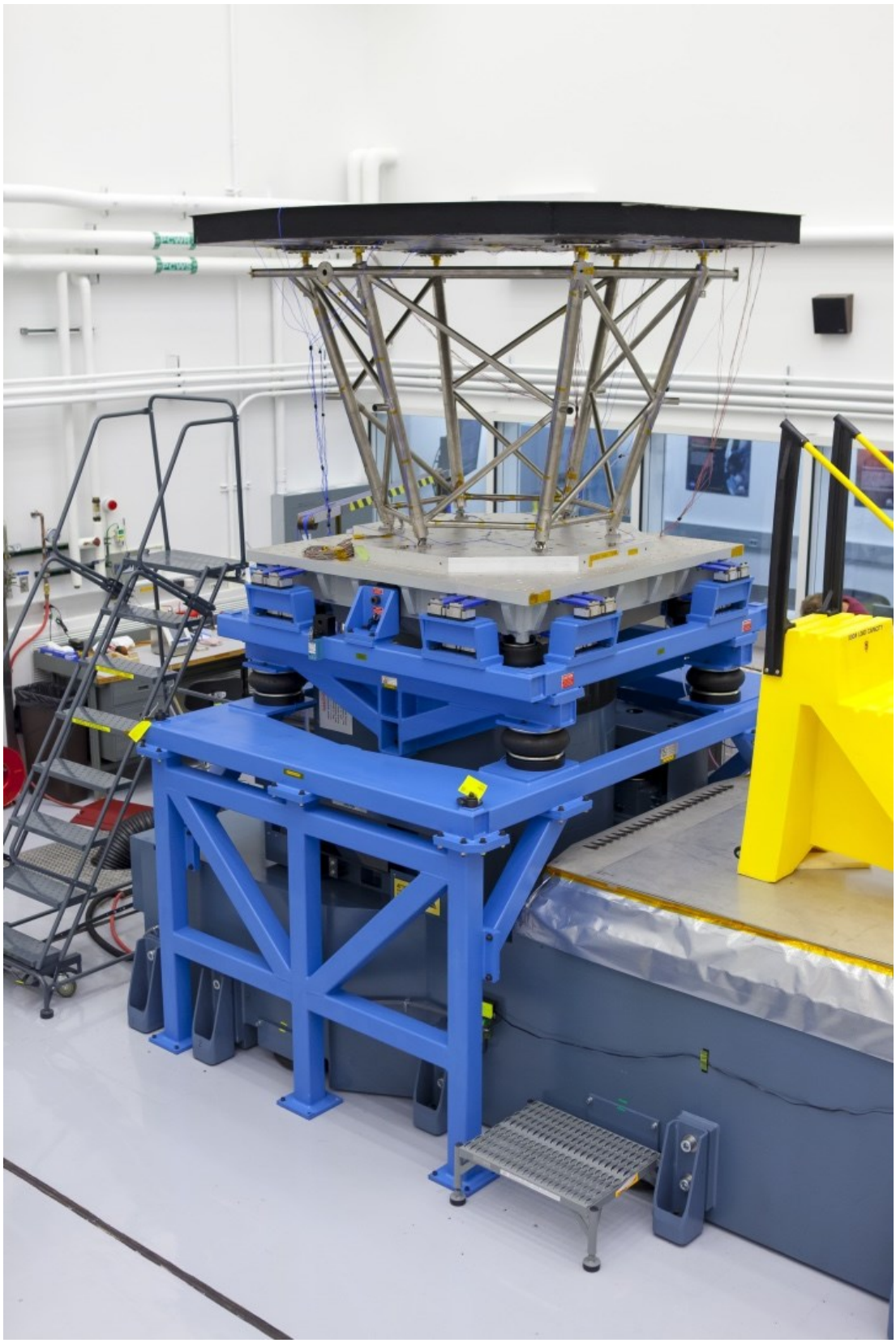

Figure 4-29 PSP TPS vibration test setup (Courtesy of Ed Whitman)

4.9. Summary of Structural Properties

Testing of structural properties was important to understand the behavior of the foam in the sandwich panel structure during launch and at the Sun and provided properties that were used in structural and thermal modeling. There were a variety of tests performed on the foam at the coupon, subsystem and full-scale level. These tests were designed to understand the effects of scale and structure on their subsequent results. The testing of interest to this work is coupon testing in tension, compression and shear on multiple foams and subscale fracture toughness tests.

Initially, coupon testing in tension, compression and shear was used to understand the material properties. All testing showed the foams studied to be brittle and anisotropic. In order to understand the anisotropy of the Ultramet 100 ppi 3% foam, the experimental data was compared to the Gibson and Ashby anisotropic model. The shear modulus anisotropy was not fully explained by the structural anisotropy described by the model. The foam was not consistently geometric anisotropic in a particular direction geometrically and the data suggested that there is further anisotropy within the material that forms the ligands of the foam.

Subscale testing was used to verify and understand the results of the coupon testing. The three-point bend testing results were in agreement with the coupon strength results but suggested less variation when compared to the coupon data. The three-point bend testing showed brittle failure like the coupon data and validated the failure in tension in bending.

Material properties from coupon testing were used to develop the full-scale and subscale models for the PSP TPS [72]. These models were used to design and verify the full-scale heat shields. For spacecraft design both dynamic and static loading must be considered. Ultimately, launch is a limited cycle dynamic event so the main concern is dynamic amplification either from the launch vehicle or the primary structure of the spacecraft. In order to avoid dynamic amplification, the natural frequencies of each component are required to be separated. These frequencies are evaluated through the FE model. These frequencies are verified in full scale testing through accelerometer data. In addition to dynamic analysis, static analysis is used to verify the components can survive the axial and lateral load factors imparted by launch. These loads are input into the FE model and stresses in the materials are derived. Using a failure criterion, material properties and proper margins of safety, the design is shown to meet all requirements from loading due to launch and handling. As a final qualification, all the heat shields were successfully tested in three axes vibration and acoustics to demonstrate they would survive the launch loads which was verified by the accelerometer data taken throughout testing [9].

In addition to launch loads, we needed to demonstrate that the heat shield would survive the thermal/structural loads at closest approach. Building on the coupon testing in thermal and structural testing, a subscale test was performed at Johnson Space Center (JSC) using a 56 cm by 56 cm by 11.4 cm TPS sandwich panel of carbon foam and carbon-carbon facesheets. This testing used embedded thermocouples and linear variable differential transformers (LVDTs) to record data at 1000°C, 1200°C and 1400°C.

Shelly Conkey built a subscale model based on a thermal model built by Elisabeth Abel. These models were used to generate a test correlated finite element model for the full scale structural-thermal analysis performed by Shelly Conkey which validated the design performance at its perihelion [73].

The successful full-scale testing was a verification of the overall design as the full-scale units remained intact throughout structural loading, both static and vibration. Using multiple scales of testing, the PSP TPS was successfully designed, fabricated, tested, verified, launched and operated within the harsh environments of the Sun. The PSP spacecraft with the TPS aboard launched on August 12, 2018. The TPS successfully survived launch as demonstrated by the thermal data from the spacecraft on the first six successful passes at three distinct solar distances. All the components remained protected behind the shield as designed throughout these solar encounters validating the thermal structural modeling and testing. The spacecraft and its heat shield will continue operating as designed for the next five years as it gets closer to the Sun and continues to send back groundbreaking science.

CHAPTER 5. Summary and Conclusions & Future Work

A mission to the Sun to study Earth's star has always been a top NASA priority, but several critical technologies had to be developed to enable this mission. These critical technologies included the heat shield, the solar power system and the mission profile. The heat shield, which needs to protect the electronics and scientific instruments on the spacecraft from the harsh environments (namely launch, radiation and heat flux) that occur when the spacecraft was launched and at its perihelion, remained a challenge for over 60 years. And, the revolutionary development of a heat shield that utilizes structurally integral thermal insulation was critical to the success of Parker Solar Probe (PSP) mission. This dissertation is focused on the thermal and structural testing that enabled the groundbreaking structurally-integral PSP TPS design; a multi-scale test approach, which developed properties for effective thermal conductivity, tension, compression and shear, demonstrated that the widely referenced Gibson and Ashby models do not explain anisotropic behavior for the structural properties of the foam or capture the radiative component of the thermal conductivity.

5.1. Summary of Findings and Accomplishments

The initial work started by surveying historic heat shields and their materials. Most of these heat shields were ablative and designed for entry into the atmosphere of Earth, which has oxygen. These ablative heat shields were not directly applicable to the design of the PSP Thermal Protection System (TPS) because they required an atmosphere to properly function and because they are heavy compared to the mass

limitations for PSP. Given the unique constraints of a spacecraft that will pass within 9.5 solar radii of the Sun, a structural sandwich panel with a carbon foam core was deemed highly desirable if the carbon foam could serve the dual role of structural support and thermal protection. Carbon foams have been around since at least the 1980s, but the design of a heat shield with it as the core component necessitated a foundational understanding of its intrinsic properties and the mechanisms by which it fails. Translating these properties into thermo-mechanical performance required the development and certification of mechanical and heat transport models. Realization and launch of the full-scale heat shield for the Parker Solar Probe required validation of the models and the integrity of the spacecraft at full scale.

To provide properties for the subscale and full-scale models and validate full scale performance through modeling, a program to experimentally characterize the carbon foam for both thermal and structural properties, at multiple scales, was developed and forms the basis of this dissertation. The multi-scale approach was broken down into three categories: coupon, subscale and full-scale testing.

Carbon foam thermal coupon testing was conducted to measure and characterize thermal transport through candidate foams.

- Guarded hot plate experiments were used to measure steady-state heat flux through the various foams and showed that the effective thermal conductivity around room temperature was dominated by the solid conductivity as predicted by the Gibson and Ashby model but that the efficiency factor deviated from the 2/3 predicted based on foam structure.

- Thermal diffusivity methods, which used an instantaneous heat pulse to determine thermal diffusivity, and indirectly effective thermal conductivity were less accurate around room temperature and underpredicted the solid conductivity components. This test data was also used to examine the effective thermal conductivity of the argon cover gas used for some testing. These results did not match the model prediction.
- The carbon foam effective thermal conductivity measured in these coupon-scale tests was used in the thermal modeling effort. Comparison with empirical models suggested by Gibson and Ashby indicated that at temperatures to 200°C the test data agreed with the model, which was governed by the solid conductivity of the material. From 200°C to 900°C, the radiation component began to influence the results, but the test data still matched the Gibson and Ashby model. Around 900°C and above, the model began to over predict the test data. This temperature was also where the subscale ORNL conductivity deviated from the coupon data.
    - Agreement between the model and the test data around room temperature was observed and interpreted as an indication that the heat conduction through the solid foam is the dominant factor at these temperatures and is well described by the Gibson and Ashby model.
    - By contrast, at elevated temperatures, radiation was found to be the dominant mode of heat transfer, and this component appears to be more complex than suggested by the Gibson and Ashby model.

- The coupon testing was also used to explore the mechanisms that govern the effective thermal conductivity. Using the coupon data, the effects of density and structure were investigated. The Grafoam data showed that the effective thermal conductivity does scale with relative density at low temperatures (around room temperature) as expected. However, structure was found to play a more important role than expected. Distinct differences in effective thermal conductivity of the Calcarb and the Grafoam FPA-10 foams, which both had a 10% relative density but different structures, were uncovered.

Structural coupon testing of the carbon foams was undertaken to ascertain the mechanical properties of the foams and to deduce the mechanisms that govern the mechanical response and failure of the candidate foams.

- Structural coupon testing consisted of tension, compression and shear assessments and the subset of data analyzed for this dissertation focused on Ultramet 100 ppi 3% and ERG 100 ppi 3% foams. Test data was taken in the three primary directions for each foam in tension and in compression. Each direction and loading type were distinct indicating anisotropy in the foam and different failure modes for the foam tension and compression as predicted.
- The torsional shear testing for the ERG 100 ppi 3% showed failure by brittle facture due to the development of tensile stresses at an angle of 45° from the loading axis, as predicted.
- The compression and tension data demonstrated anisotropy for all foams. Gibson and Ashby postulated that this anisotropy was mostly driven by

geometric structural differences in the lattice of the foam. Using their anisotropic model, the Ultramet 100 ppi 3% Young's and shear modulus ratios were compared to model predictions. While the Ultramet 100 ppi 3% displayed some geometric structural anisotropy in every block, geometric differences alone did not explain the elastic anisotropy.

The structural and thermal coupon testing had some common themes as they allowed us to acquire the intrinsic properties of a variety of candidate foam and compare these results to models. In addition to foam selection, the data from these measurements were used in full-scale models that allowed us to validate the design of the PSP heat shield. Initially, the coupon tests showed reasonable correlation to the classical Gibson and Ashby model, however, at elevated temperatures or increased levels of structural and material anisotropy the relationship between the G+A model and the experimental data broke down. This fact underscored the need for extensive testing, both at the coupon and subscale level, as part of the overall PSP test program.

Specifically, this dissertation reviewed the results of full thickness subscale tests that were conducted at Oak Ridge National Laboratory and fracture toughness testing that was conducted at Touchstone Research Laboratory and led to the following conclusions.

- The sub-scale tests elucidated the fact that thickness has a significant influenced on thermal transport through the foam, and that thermal coupon testing overestimates the effective thermal conductivity of the foam at higher temperatures where radiation dominates.

- Structural subscale testing, undertaken to confirm the properties measured coupon scale showed that coupon strength could be translated to larger pieces as predicted. An example highlighted in this dissertation was the unnotched fracture toughness beam test; a three-point bend test that showed the failure in bending to be consistent with the higher end of the tensile strength that was measured in the coupon tests. In general, subscale thermal and structural testing allowed the coupon results to be corroborated at larger scale with controlled boundary conditions.
- Taken as a whole, the subscale tests resulted in controlled failure allowing for assessment of the mechanisms and values from the coupon scale. Some of these tests verified the coupon results while some of these tests pointed to different mechanisms being at play for the larger scale. In thermal testing, thickness was shown to play a role in the results for effective thermal conductivity testing and in structural testing, bending subscale testing was less variable than tensile coupon testing indicating the larger scale is failure tolerant when the region of higher stress is small due to system level effects on the boundary conditions of the foam.

Given the premium demand on reliability for interplanetary spacecraft, the coupon and subscale data were used to develop limit values or ranges of values that were used in the full-scale models. A margin based on statistical variations was added to the required limit values to ensure success. Therefore, the full-scale design was nowhere near the limits of the material and the full-scale testing served as a pass/fail

test. The full-scale heat shield was expected to remain intact when subjected to the appropriate loading. The validation for launch of the flight TPS was accomplished through years of reviews of the testing and modeling effort culminating in a successful full-scale flight unit build, vibration testing, acoustic testing, cold thermal testing and integration onto the spacecraft.

In summary, the carbon foam selected for the core of the PSP heat shield were tested on multiple scales. Full-scale testing provided a go/no go criterion designed to ensure mission success. By its nature, full scale testing cannot be used to understand material behavior and failure criteria, because loading is complex and boundary conditions cannot be well controlled. In order to understand and design for the limitations of a system, coupon testing, subscale testing and full-scale testing must be used together. This study presented in this dissertation focused on one material of the PSP TPS, the carbon foam. The multi-scale testing approach outlined here made the PSP TPS possible and part of that development was extensive work put into understanding how to manufacture the entire unit into a system in a consistent manner. The interactive approach between coupon, subscale and full-scale testing was implemented across the efforts on the PSP TPS culminating in the successful launch of the spacecraft shown in Figure 5-1. In the early hours of August 12, 2108, PSP launched and started its journey to study the Sun.

Figure 5-1 Parker Solar Probe launch on August 12, 2018 (Photo courtesy of Billy Gallagher)

5.2. Future Work

This specific research ultimately ended with the successful launch of PSP on August 12, 2018, but the impact of this work continues. PSP has seen phenomena at the Sun that are changing our understanding of its inner workings. This mission has already redefined solar science and as Dr. Parker, the namesake of PSP, states: “over the past year, the data from PSP have revealed a new reality of the solar wind and the inner

reaches of the solar atmosphere. We anticipate finding clues to some old questions and posing more questions based on unexpected phenomena as this historic mission flies increasingly closer to the Sun, and also as solar activity increases with the rise of the new solar cycle," [5]. Over the next five years, as the spacecraft gets closer to the Sun, the science returns will continue.

While this specific research and development project has ended, the principles of this work provide a foundation that can be applied to future missions and spacecraft design. The techniques used to understand the behavior of the carbon foam are applicable to the development of complex systems, particularly high temperature ones. Interstellar Probe, which will use the Sun as a gravity assist body to send a spacecraft into interstellar space, will have a larger heat shield and need to withstand even harsher conditions. The Interstellar Probe Heat Shield is already building on the fundamentals developed for the PSP TPS [74]. Moreover, hypersonic body development is also rapidly gaining favor. These bodies will need to have material systems that work in extreme thermal and structural environments. As materials are developed for these systems, comprehending their behavior in the lab, in systems and in their functional environment, is critically important. Gaining an understanding of material properties and performance at multiple scales and evaluating material behavior in these contexts will be necessary develop the next generation of high temperature material systems.

When developing these types of systems for more extreme environments, the material limitations of the sandwich components must be understood first. The service temperatures and/or radiation environments boundaries where the materials

breakdown or lose all structural and thermal capabilities will be the edge of the usable space for a thermal protection system. Refractory metals have high service temperatures but are heavy and so extensive use in a thermal protection system would limit the mass for the rest of the spacecraft due to launch capacity. The material service temperatures required temperatures for the use case, and the overall mass of the system must be balanced in material selection.

For structurally integral insulation, the foundations of a test program should be effective thermal conductivity over the temperature range of interest and coupon testing in compression, tension, and shear in all three axes. Due to the delicate nature of the carbon foam studied here, almost all testing categories required multiple iterations before getting reliable results indicated by consistent data with proper failure modes. The basis of a proper test program on these types of materials is exploration and refining the proper test technique set. This basic coupon testing can illuminate where the material differs from the modeling. Likely, if temperatures of interest are above 900°C, traditional modeling and testing will not capture proper behavior and subscale testing, particularly using the proper thickness must be undertaken. For structural properties, the coupon testing will indicate the level of anisotropy present and subscale testing will be important to understand the effects of boundary conditions like point loading. These tests might indicate the need for more testing such as off axis loading, multi-axis loading testing, and high temperature compression and tension testing which were all performed on a small subset of carbon foam samples as part of the overall PSP TPS effort.

This methodology can be furthered to a wide variety of lattice materials and structures built through additive manufacturing. For these materials, the scale behaviors and the implications of the structure must be understood. These materials have a significant potential to optimize behavior for both structural and thermal properties. However, standard tests alone will not enable the user to understand the real behavior in extreme environments. Additive manufacturing can make lighter and optimized structures not possible through subtractive manufacturing. Much of this great promise of additive manufacturing is using lattices that are stronger and lighter than the bulk material of the parent material. The topology optimization used in additive processes can create internal lattice structures that are not possible through traditional subtractive manufacturing. Like the carbon foam, these parts often have lattice structures that make them very low density relative to the bulk material.

The possibilities of additive manufacturing or coatings on traditional lattices opens up new possibilities based on the knowledge from this dissertation. The effective thermal conductivity testing demonstrated that the properties around room temperature are driven by the bulk of the solid while the higher temperature performance is driven by optical properties. Lattice structures could be tailored based on the bulk properties of the strut materials while the optical properties could be manipulated through a coating or additively deposited outer surface. Additionally, this work showed that the anisotropy in the foams were not purely geometric structural anisotropy. In applications where unidirectional loading is critical, it is possible that the material properties within the lattice could be controlled to the user's benefit.

Many of the coupons and samples of additive lattices currently are built on small printers that have limitations on the print bed. As these techniques are scaled up using printers that are on the size of buildings or rockets [75], the size scale effect on material testing and how to accurately test these materials must be fully understood. This work demonstrated that traditional methodologies of using coupon testing to develop limit values for full scale systems without an intermediate size scale of testing may lead to inaccurate results. A new paradigm must be adapted for testing and designing with these materials.

The PSP TPS, building on decades of studies and materials development, went from a paper-concept to a full-scale article build in less than five years. This achievement was immediately followed by a similar timeline in which fabrication, qualification, and spacecraft integration took place. The PSP TPS development effort provides a blueprint for the ongoing and future simultaneous development of novel materials, design, analysis, and manufacturing techniques that are needed to enable the realization of revolutionary high temperature engineering systems.

REFERENCES

[1] N. J. Fox *et al.*, "The Solar Probe Plus Mission: Humanity's First Visit to Our Star," *Space Science Reviews,* vol. 204, no. 1-4, pp. 7-48, 2015, doi: 10.1007/s11214-015-0211-6.

[2] JHUAPL. "The Mission Overview." http://parkersolarprobe.jhuapl.edu/index.php#the-mission (accessed October 5, 2019).

[3] JHUAPL. "The Mission Overview." http://parkersolarprobe.jhuapl.edu/index.php#the-mission (accessed September 20, 2019).

[4] S. Frazier, "NASA's Parker Solar Probe Sheds New Light on the Sun," ed. www.nasa.gov, 2019.

[5] E. N. Parker, "Exploring the innermost solar atmosphere," *Nature Astronomy,* vol. 4, no. 1, pp. 19-20, 2019, doi: 10.1038/s41550-019-0985-7.

[6] R. A. Howard *et al.*, "Near-Sun observations of an F-corona decrease and K-corona fine structure," *Nature,* vol. 576, no. 7786, pp. 232-236, Dec 2019, doi: 10.1038/s41586-019-1807-x.

[7] J. C. Kasper *et al.*, "Alfvenic velocity spikes and rotational flows in the near-Sun solar wind," *Nature,* vol. 576, no. 7786, pp. 228-231, Dec 2019, doi: 10.1038/s41586-019-1813-z.

[8] S. D. Bale *et al.*, "Highly structured slow solar wind emerging from an equatorial coronal hole," *Nature,* vol. 576, no. 7786, pp. 237-242, Dec 2019, doi: 10.1038/s41586-019-1818-7.

[9] E. Congdon, S. Conkey, D. Mehoke, E. Schaefer, and E. Abel, "Case Study of the Parker Solar Probe Thermal Protection System: Development of a System Level Process for High Temperature Technology Achievement," presented at the 70th International Astronautical Congress (IAC), Washington, DC, 21-25 October 2019.

[10] E. Venkatapathy, B. Laub, G. J. Hartman, J. O. Arnold, M. J. Wright, and G. A. Allen, "Thermal protection system development, testing, and qualification for atmospheric probes and sample return missions," *Advances in Space Research,* vol. 44, no. 1, pp. 138-150, 2009, doi: 10.1016/j.asr.2008.12.023.

[11] C. Szalai, E. Slimko, and P. Hoffman, "Mars Science Laboratory Heatshield Development, Implementation, and Lessons Learned," *Journal of Spacecraft and Rockets,* vol. 51, no. 4, pp. 1167-1173, 2014, doi: 10.2514/1.A32673.

[12] D. Benningfield. (2011) Tough Skin: The orbiter's protection against the hellish heat of hypersonic flight. *Air & Space Magazine*.

[13] D. Leiser, "Space Shuttle Thermal Protection System," *American Ceramic Society Bulletin,* vol. 83, no. 8, August 2004.

[14] Ultramet. "Refractory Open Cell Foams." https://ultramet.com/refractory-open-cell-foams/ (accessed December 17, 2019).

[15] E. Aerospace. "The Basics of Duocel Foam." http://ergaerospace.com/technical-data/the-basics-of-duocel-foam/ (accessed January 4, 2020).

[16] Graftech. *Lightweight, stable large-tool concept requires no master model*, High Performance Composites, 2009, p. 50.

[17] Mersen. "Rigid Carbon Insulation." https://www.mersen.com/products/graphite-specialties/carbon-insulation/rigid-carbon-insulation (accessed September 23, 2020.

[18] V. S. Deshpande, M. F. Ashby, and N. A. Fleck, "Foam topology: bending versus stretching dominated architectures," *Acta Materialia,* vol. 49, no. 6, pp. 1035-1040, 2001/04/02/ 2001, doi: https://doi.org/10.1016/S1359-6454(00)00379-7.

[19] N. A. Fleck, V. S. Deshpande, and M. F. Ashby, "Micro-architectured materials: past, present and future," *Proceedings: Mathematical, Physical and Engineering Sciences,* vol. 466, no. 2121, pp. 2495-2516, 2010.

[20] M. Letellier, C. Delgado-Sanchez, M. Khelifa, V. Fierro, and A. Celzard, "Mechanical properties of model vitreous carbon foams," *Carbon,* vol. 116, pp. 562-571, 2017.

[21] S. Sihn and A. K. Roy, "Modeling and prediction of bulk properties of open-cell carbon foam," *Journal of the Mechanics and Physics of Solids,* vol. 52, no. 1, pp. 167-191, 1// 2004, doi: http://dx.doi.org/10.1016/S0022-5096(03)00072-3.

[22] R. M. Christensen, "Mechanics of Cellular and Other Low-Density Materials," *Int. J. Solids Struct.,* vol. 37, pp. 93-104, 2000.

[23] L. J. Gibson and M. F. Ashby, "Cellular Solids: Structure and Properties-Second Edition," in *Cambridge Solid State Science Series*. Cambridge, UK: Cambridge University Press, 1999. 1988.

[24] A. M. Druma, M. K. Alam, and C. Druma, "Analysis of thermal conduction in carbon foams," *International Journal of Thermal Sciences,* vol. 43, no. 7, pp. 689-695, 2004.

[25] S. W. Choi, J. M. Jung, H. M. Yoo, S. H. Kim, and W. I. Lee, "Analysis of thermal properties and heat transfer mechanisms for polyurethane foams blown with water," *Journal of Thermal Analysis and Calorimetry,* vol. 132, no. 2, pp. 1253-1262, 2018, doi: 10.1007/s10973-018-6990-8.

[26] J. E. Li and B. Wang, "Equivalent Thermal Conductivity of Open-Cell Ceramic Foams at High Temperatures," *International Journal of Thermophysics,* vol. 35, no. 1, pp. 105-122, 2013, doi: 10.1007/s10765-013-1545-5.

[27] J.-F. Sacadura, "Thermal Radiative Properties of Complex Media: Theoretical Prediction Versus Experimental Identification," *Heat Transfer Engineering,* vol. 32, no. 9, pp. 754-770, 2011, doi: 10.1080/01457632.2011.525140.

[28] M. Sans, V. Schick, G. Parent, and O. Farges, "Experimental characterization of the coupled conductive and radiative heat transfer in ceramic foams with a flash method at high temperature," *International Journal of Heat and Mass Transfer,* vol. 148, 2020, doi: 10.1016/j.ijheatmasstransfer.2019.119077.

[29] L. J. Gibson and M. F. Ashby, *Cellular Solids: Structure and Properties* (Cambridge Solid State Science Series). Cambridge, United Kingdom: Cambridge University Press, 1999.

[30] S. Choi and B. V. Sankar, "Fracture Toughness of Carbon Foam," *Journal of Composite Materials,* vol. 37, no. 23, pp. 2101-2116, 2003, doi: 10.1177/002199803036264.

[31] S. D. Ryan and J. L. Williams, "Tensile Testing of Rodlike Trabeculae Excised from Bovine Femoral Bone," *J. Biomechanics,* vol. 22, no. 4, pp. 351-355, 1989.

[32] M. m. k. m. i. a. i. Karamooz Ravari and M. k. c. i. a. i. Kadkhodaei, "A Computationally Efficient Modeling Approach for Predicting Mechanical Behavior of Cellular Lattice Structures," *Journal of Materials Engineering & Performance,* Article vol. 24, no. 1, pp. 245-252, 01// 2015, doi: 10.1007/s11665-014-1281-4.

[33] S. M. Mukhopadhyay, N. Mahadev, P. Joshi, A. K. Roy, K. M. Kearns, and D. P. Anderson, "Structural investigation of graphitic foam," *Journal of Applied Physics,* vol. 91, no. 5, p. 3415, 2002, doi: 10.1063/1.1448675.

[34] R. G. Hutchinson and N. A. Fleck, "Microarchitectured cellular solids – the hunt for statically determinate periodic trusses," *ZAMM - Journal of Applied Mathematics and Mechanics / Zeitschrift für Angewandte Mathematik und Mechanik,* vol. 85, no. 9, pp. 607-617, 2005, doi: doi:10.1002/zamm.200410208.

[35] A. J. Jacobsen, S. Mahoney, W. B. Carter, and S. Nutt, "Vitreous carbon micro-lattice structures," *Carbon,* vol. 49, no. 3, pp. 1025-1032, 2011/03/01/ 2011, doi: https://doi.org/10.1016/j.carbon.2010.10.059.

[36] L. R. Meza *et al.*, "Reexamining the mechanical property space of three-dimensional lattice architectures," *Acta Materialia,* vol. 140, pp. 424-432, 2017/11/01/ 2017, doi: https://doi.org/10.1016/j.actamat.2017.08.052.

[37] L. C. Montemayor and J. R. Greer, "Mechanical Response of Hollow Metallic Nanolattices: Combining Structural and Material Size Effects," *Journal of Applied Mechanics,* vol. 82, no. 7, pp. 071012-071012, 2015, doi: 10.1115/1.4030361.

[38] T. C. Triantafillou, J. Zhang, T. L. Shercliff, L. J. Gibson, and M. F. Ashby, "Failure Surfaces for Cellular Materials Under Multiaxial Loads-II. Comparison of Models with Experiment," *International Journal of Mechanical Sciences,* vol. 31, no. 9, pp. 665-678, 1989.

[39] L. Valdevit, A. J. Jacobsen, and J. R. Greer, "Protocols for the Optimal Design of Multi-Functional Cellular Structures: From Hypersonics to Micro-Architected Materials," *Journal of the American Ceramic Society,* Article vol. 94, pp. 1-20, 06// 2011, doi: 10.1111/j.1551-2916.2011.04599.x.

[40] L. Salari-Sharif and L. Valdevit, "Accurate Stiffness Measurement of Ultralight Hollow Metallic Microlattices by Laser Vibrometry," *Experimental Mechanics,* Article vol. 54, no. 8, pp. 1491-1495, 15 August 2014, doi: 10.1007/s11340-014-9917-8.

[41] Z. Hashin and S. Shtrikman, "A Variational Approach to the Theory of the Elastic Behaviour of Multiphase Materials," *J. Mech. Phys. Solids,* vol. 11, pp. 127-140, September 8, 1962.

[42] O. Zerhouni, M. G. Tarantino, and K. Danas, "Numerically-aided 3D printed random isotropic porous materials approaching the Hashin-Shtrikman bounds," *Composites Part B: Engineering,* vol. 156, pp. 344-354, 2019, doi: 10.1016/j.compositesb.2018.08.032.

[43] M. G. Tarantino, O. Zerhouni, and K. Danas, "Random 3D-printed isotropic composites with high volume fraction of pore-like polydisperse inclusions and near-optimal elastic stiffness," *Acta Materialia,* vol. 175, pp. 331-340, 2019, doi: 10.1016/j.actamat.2019.06.020.

[44] T. Uhlířová and W. Pabst, "Thermal conductivity and Young's modulus of cubic-cell metamaterials," *Ceramics International,* vol. 45, no. 1, pp. 954-962, 2019, doi: 10.1016/j.ceramint.2018.09.271.

[45] X. Fu, R. Viskanta, and J. P. Gore, "Prediction of Effective Thermal Conductivity of Cellular Ceramics," *Int. Comm. Heat Mass Transfer,* vol. 25, no. 2, pp. 151-160, 1998.

[46] J. K. Carson, S. J. Lovatt, D. J. Tanner, and A. C. Cleland, "Thermal conductivity bounds for isotropic, porous materials," *International Journal of Heat and Mass Transfer,* vol. 48, no. 11, pp. 2150-2158, 2005, doi: 10.1016/j.ijheatmasstransfer.2004.12.032.

[47] T. Mai. "Technology Readiness Level." NASA. https://www.nasa.gov/directorates/heo/scan/engineering/technology/txt_accordion1.html (accessed September 27, 2020.

[48] C. E. Howard, "Averting on-orbit mission failure," *Military & Aerospace Electronics,* vol. 26, no. 5, pp. 20-30, 2015.

[49] A. L. Olechowski, S. D. Eppinger, N. Joglekar, and K. Tomaschek, "Technology readiness levels: Shortcomings and improvement opportunities," *Systems Engineering,* vol. 23, no. 4, pp. 395-408, 2020, doi: 10.1002/sys.21533.

[50] B. Nielsen, D. Schneider, and D. Oakes. *Final Report for The Johns Hopkins University Applied Physics Laboratory Purchase Order Number 947563 Thermal Conductivity Measurements of Carbon Foam Specimens, 2009*.

[51] F. P. Incropera and D. P. DeWitt, *Fundamentals of Heat and Mass Transfer*, Fifth Edition ed. Hoboken, NJ: John Wiley & Sons, Inc., 2002.

[52] M. A. Schuetz and L. R. Glicksman, "A basic study of heat transfer through foam insulation," *J Cell Plast,* vol. 20, no. 2, pp. 114-21, 1984.

[53] J. Gembarovic and J. Freeman. *Thermophysical Properties of Six Carbon Samples in Vacuum, 2009.*

[54] Y. A. Cengel and M. A. Boles, *Thermodynamics: An Engineering Approach*, Fifth ed. NY, NY: McGraw-Hill, 2006.

[55] *ASTM E1461-13 Standard Test Method for Thermal Diffusivity by the Flash Method*, A. International, West Conchohocken, PA, 2013. [Online]. Available: https://doi.org/10.1520/E1461-13

[56] J. Gembarovic and R. E. Taylor, "A Method for Thermal Diffusivity Determination of Thermal Insulators," *International Journal of Thermophysics,* journal article vol. 28, no. 6, p. 2164, October 11 2007, doi: 10.1007/s10765-007-0279-7.

[57] A. S. Sabau, C. E. Duty, R. B. Dinwiddie, M. Nichols, C. A. Blue, and R. D. Ott, "A radiative transport model for heating paints using high density plasma arc lamps," *Journal of Applied Physics,* vol. 105, no. 8, p. 084901, 2009/04/15 2009, doi: 10.1063/1.3097356.

[58] JHUAPL, "Parker Solar Probe's Heat Shield Enters Thermal Vacuum Testing," ed. parkersolarprobe.jhuapl.edu, 2017.

[59] M. Khairul Alam and B. Maruyama, "Thermal Conductivity of Graphitic Carbon Foams," *Experimental Heat Transfer,* vol. 17, no. 3, pp. 227-241, 2004, doi: 10.1080/08916150490449055.

[60] R. Coquard, D. Rochais, and D. Baillis, "Conductive and Radiative Heat Transfer in Ceramic and Metal Foams at Fire Temperatures," *Fire Technology,* vol. 48, no. 3, pp. 699-732, 2010, doi: 10.1007/s10694-010-0167-8.

[61] C. C. Tseng, T. A. Parthasarathy, R. L. Sikorski, R. Viskanta, and M. Y. Chen, "Effect of thermal radiation on the effective thermal conductivity of open-cell SiC foams," *High Temperatures-High Pressures,* vol. 42, pp. 387-403, 2013.

[62] C. C. Tseng, R. L. Sikorski, R. Viskanta, M. Y. Chen, and D. Smith, "Effect of Foam Properties on Heat Transfer in High Temperature Open-Cell Foam Inserts," *Journal of the American Ceramic Society,* vol. 95, no. 6, pp. 2015-2021, 2012, doi: 10.1111/j.1551-2916.2012.05177.x.

[63] Z. Witzgall, "JH7094," Touchstone Research Laboratory, Tridelphia, WV, March 24, 2011.

[64] Z. Witzgall, "JH7191," Touchstone Research Laboratory, Tridelphia, WV, January 30, 2012.

[65] *Standard Test Method for Flatwise Tensile Strength of Sandwich Constructions*, A. International, West Conshohocken, PA, 2016.

[66] Z. Witzgall, "JH6965," Touchstone Research Laboratory Mechanical Testing, Tridelphia, WV, July 6, 2010.

[67] *C365/C365M-16 Standard Test Method for Flatwise Compressive Properties of Sandwich Cores*, A. International, West Conshohocken, PA, 2016.

[68] A. K. Roy and J. D. Camping, "Development of a Portable Shear Test Fixture for Low Modulus Porous (Foam) Materials," *Experimental Mechanics,* vol. 43, no. 1, pp. 39-44, 2003.

[69] F. Beer, E. R. J. Jr., and J. T. Dewolf, *Mechanics of Materials*, Fourth ed. New York, NY: McGraw-Hill, 2006.

[70] Z. Witzgall, "JH7028," Touchstone Research Laboratory, Tridelphia, WV, July 28, 2010.

[71] M. McBee, "JH7236," Touchstone Research Laboratory, Tridelphia, WV, December 11, 2012.

[72] E. Schaefer and S. Conkey, "Designing, Building and Testing of a Thermal Protection System for a Spacecraft Which Cannot be Qualified Using Standard Methodology," presented at the 70th International Astronautical Congress, Washington, DC, 2019.

[73] S. Conkey, E. Congdon, E. Schaefer, and E. Abel, "Solar Probe Structural-Thermal Analysis Challenges," Washington, DC, 21-25 October 2019.

[74] D. Oberhaus, "A Solar Powered Rocket Might Be Our Ticket to Interstellar Space," *WIRED*, November 20. 2020.

[75] R. Space. "Relativity Space." https://www.relativityspace.com/ (accessed October 2019)

[76] M. L. Huber and A. H. Harvey, "Thermal Conductivity of Gases," NIST. [Online]. Available: https://tsapps.nist.gov/publication/get_pdf.cfm?pub_id=907540

Appendix A: Calculation of Effective Thermal Conductivity Based on Gibson and Ashby

The effective thermal conductivity model according to Gibson and Ashby is based on the conduction of the solid [29]. For these materials, the solid is amorphous carbon. The thermal conductivity of amorphous carbon change over temperature and Incropera and DeWitt have the value of the thermal conductivity up to 1500 K [51]. Figure A-1 is adapted from the table in this textbook. It matches a cubic fit to the data so that the effective thermal conductivity can be calculated between the data points.

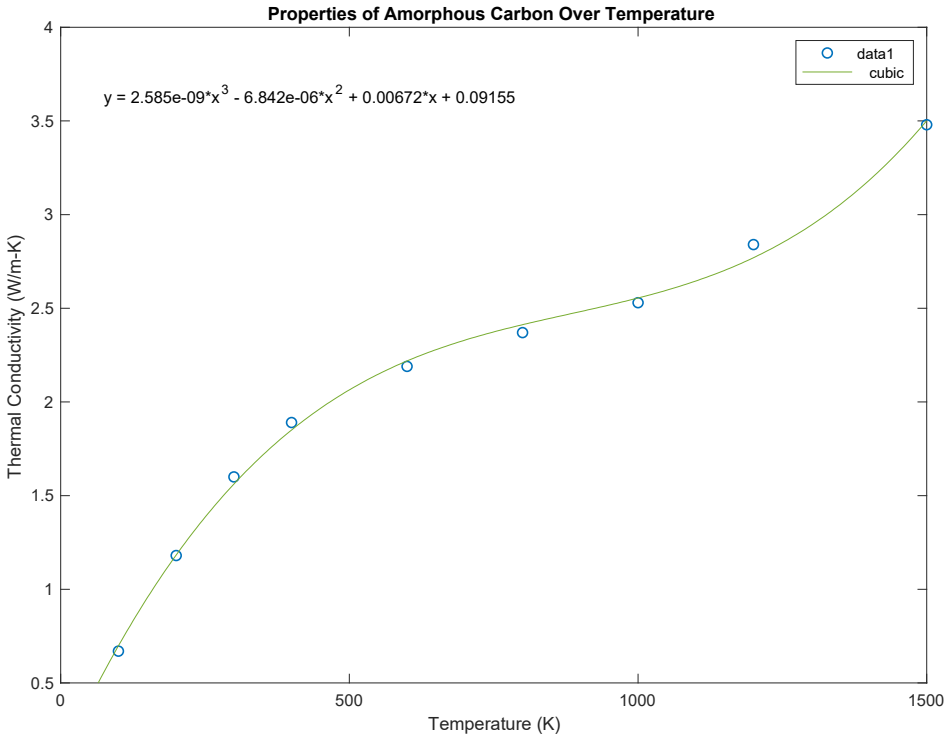

Figure A-1 Thermal Conductivity of Amorphous Carbon Adapted from Incropera and DeWitt [51]

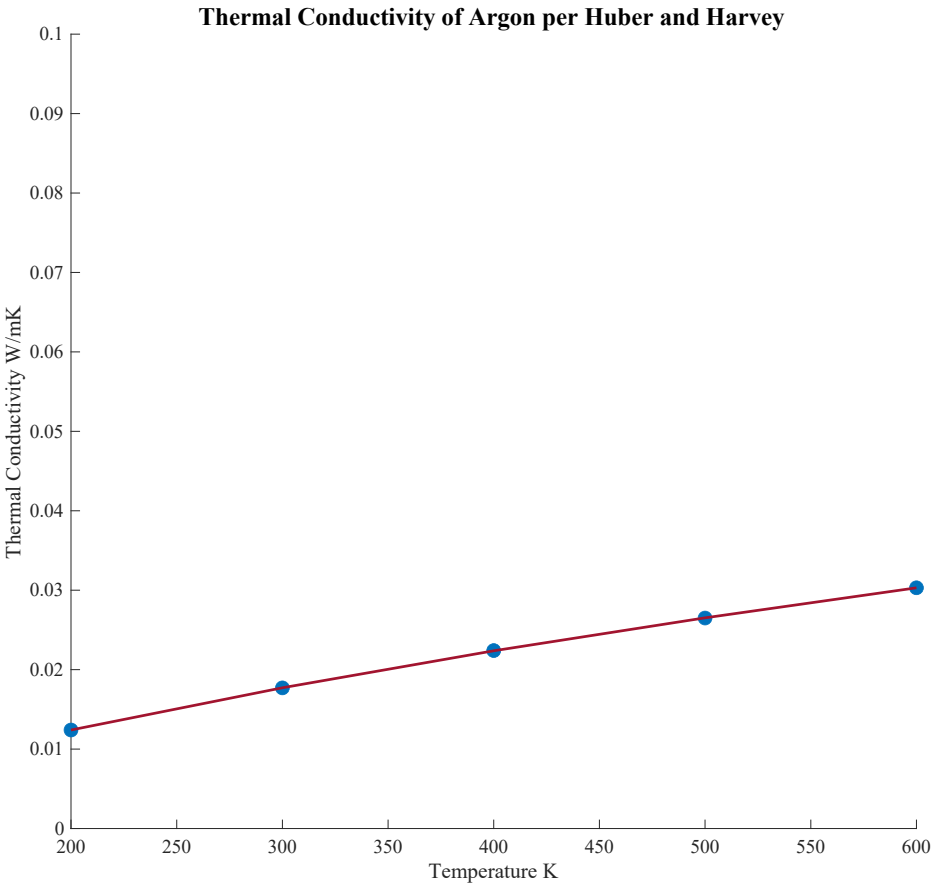

Figure A-2 The Thermal Conductivity of Argon per Huber and Harvey [76]

Appendix B: Effective Thermal Conductivity Coupon Testing Graphs at the Same Scale

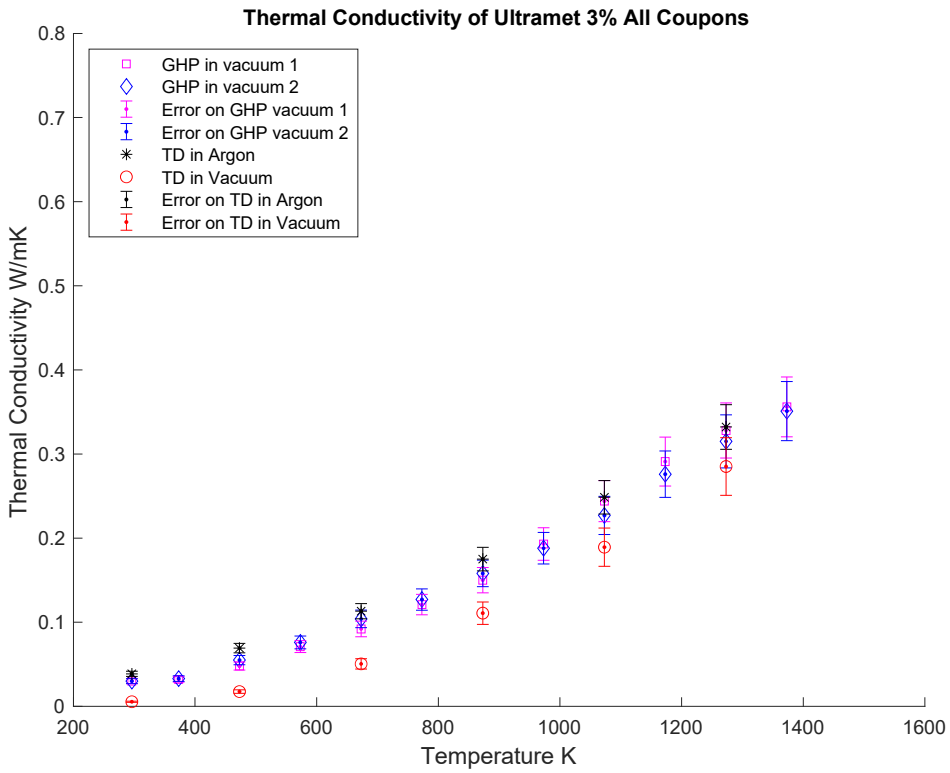

Figure B-1 All Coupon Data for Ultramet 3%

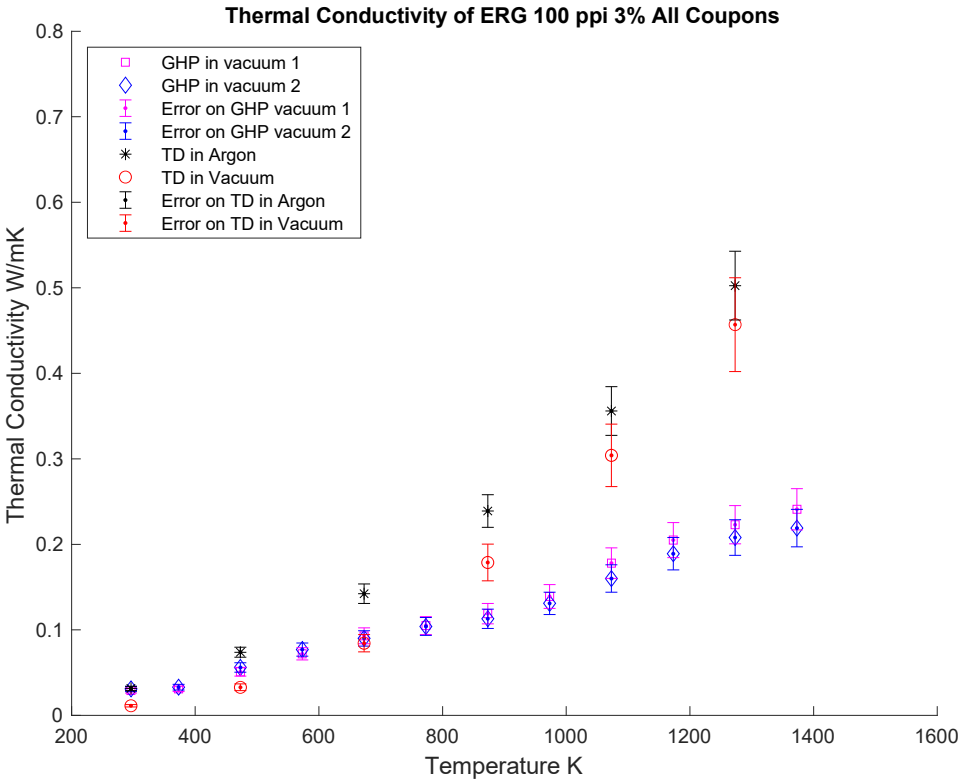

Figure B-2 ERG All Coupon Data

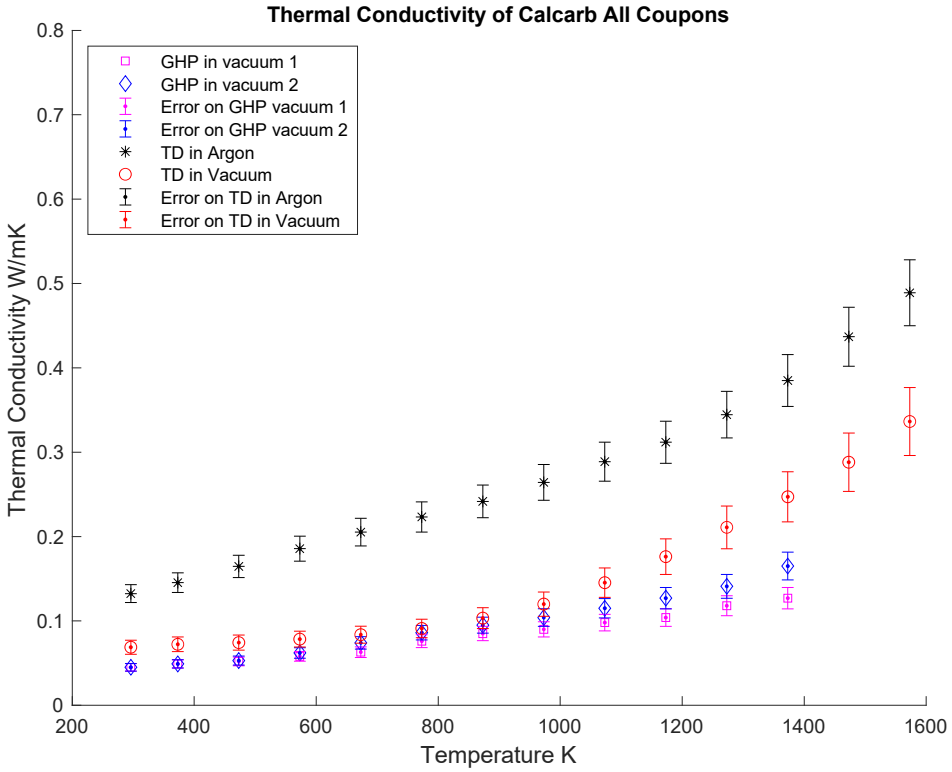

Figure B-3 All coupon data Calcarb

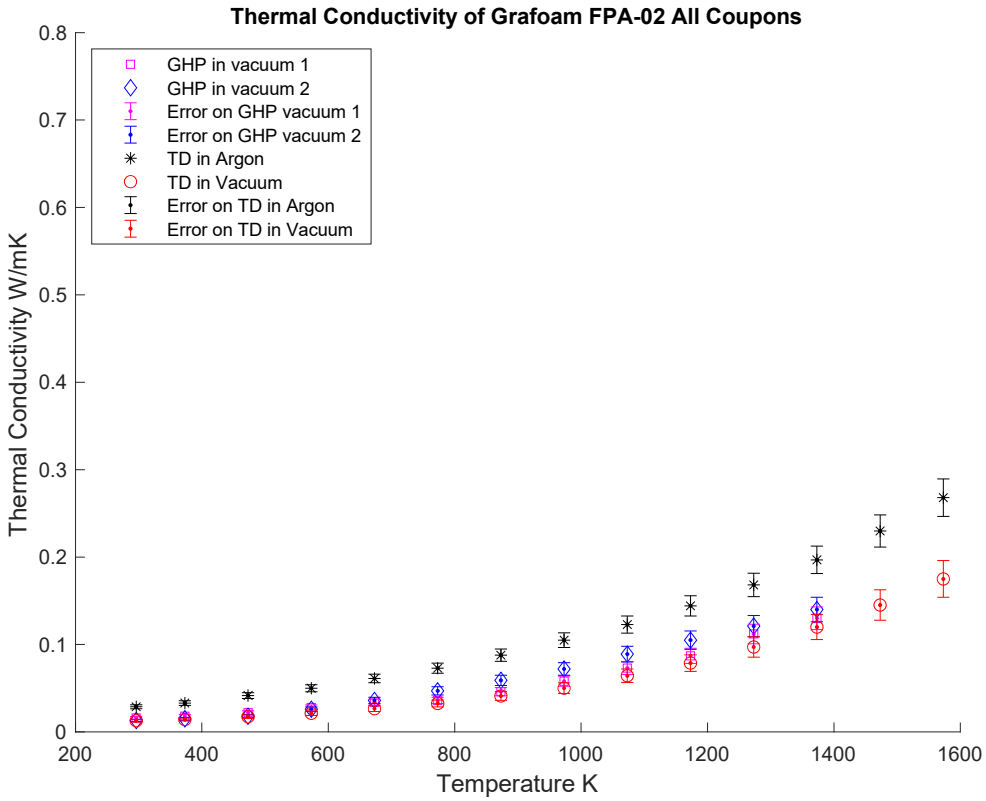

Figure B-4 Grafoam FPA-02 All Coupon Data

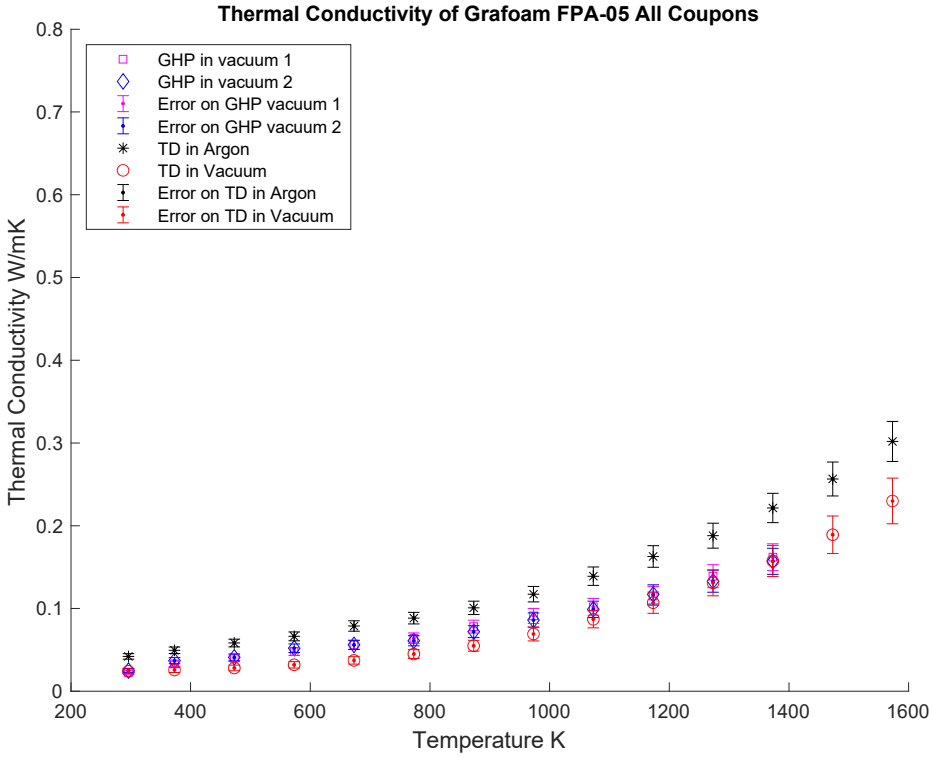

Figure B-5 Grafoam FPA-05 All Coupons

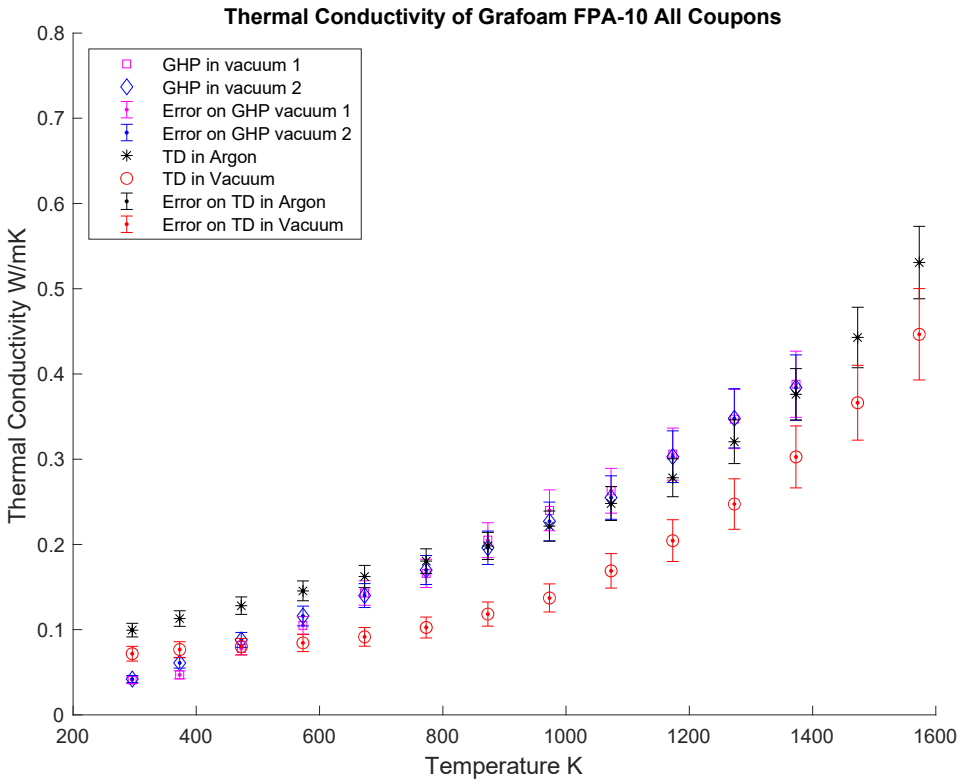

Figure B-6 Grafoam FPA-10 All Coupons

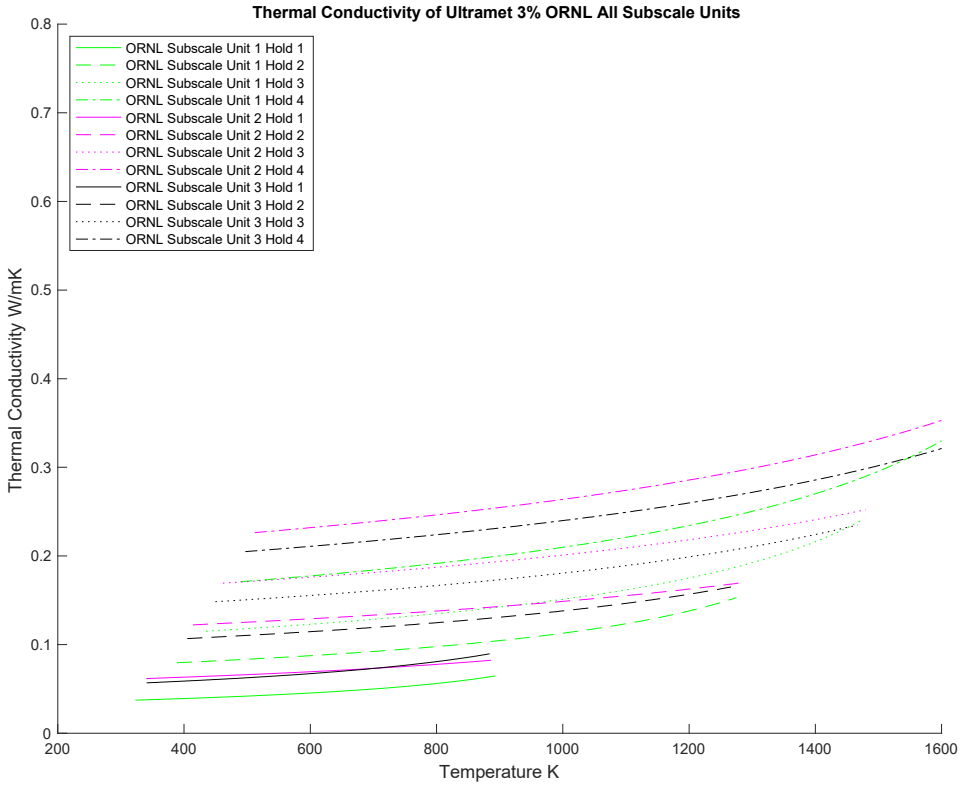

Figure B-7 ORNL Test Data

Appendix C: Effective Thermal onductivity Coupon Testing Graphs at Meaningful Scales

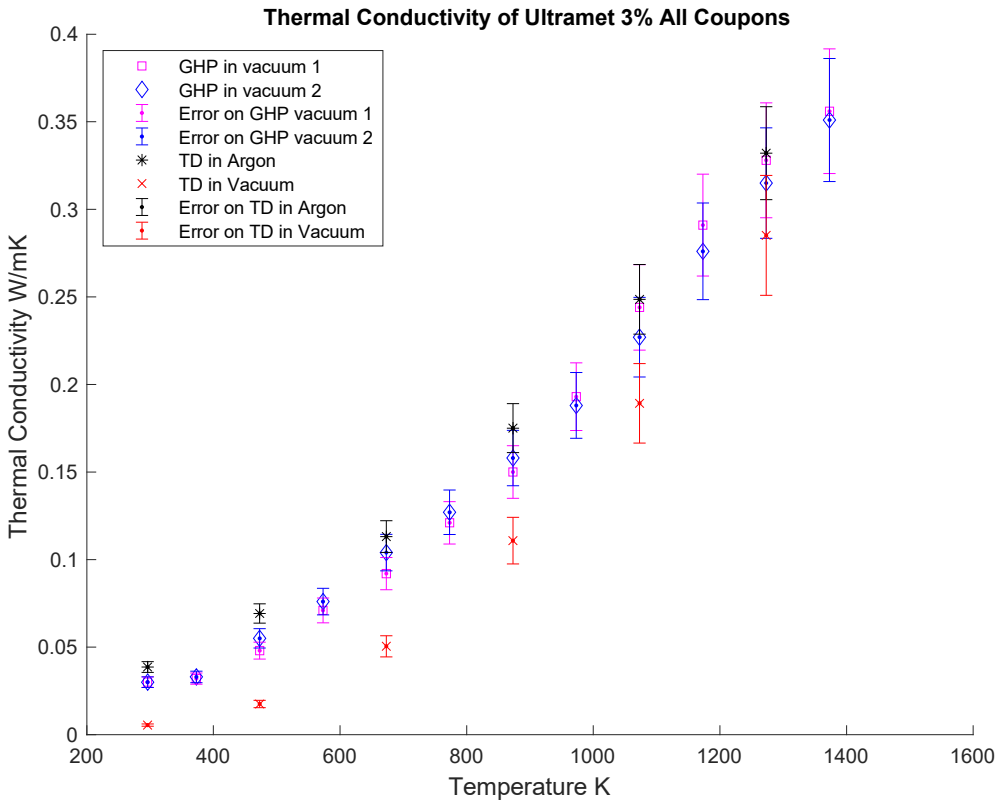

Figure C-1 Ultramet 3% 100 ppi Coupon Data

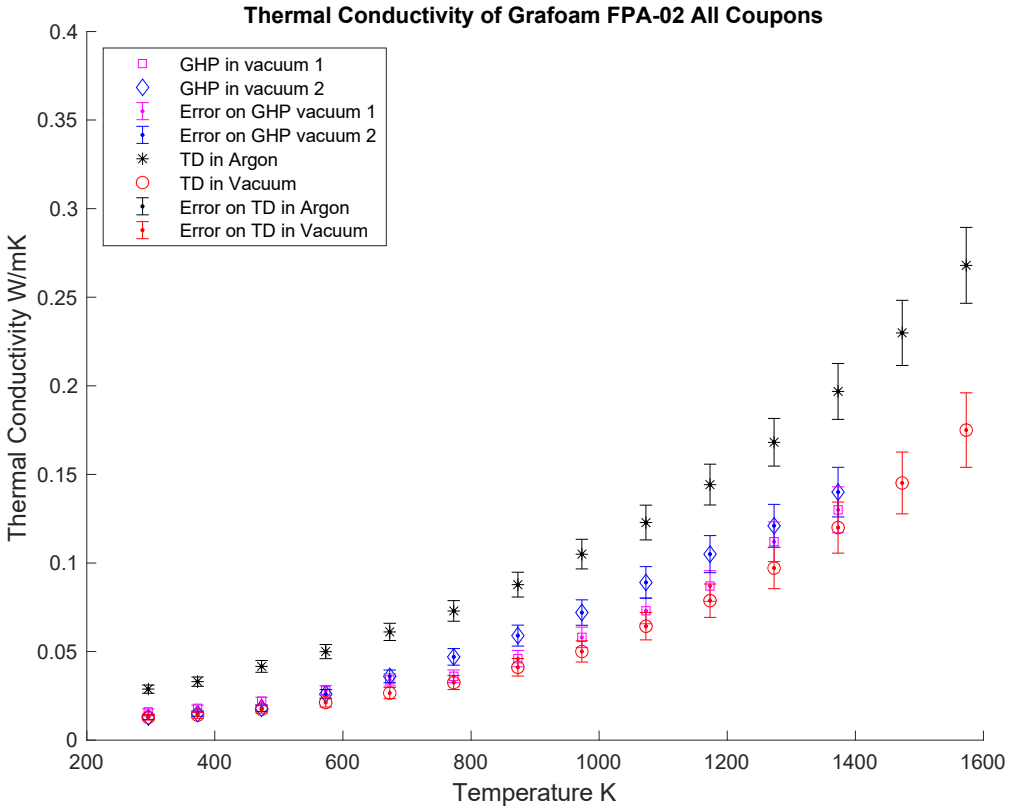

Figure C-2 Grafoam FPA-02 All Coupon Data

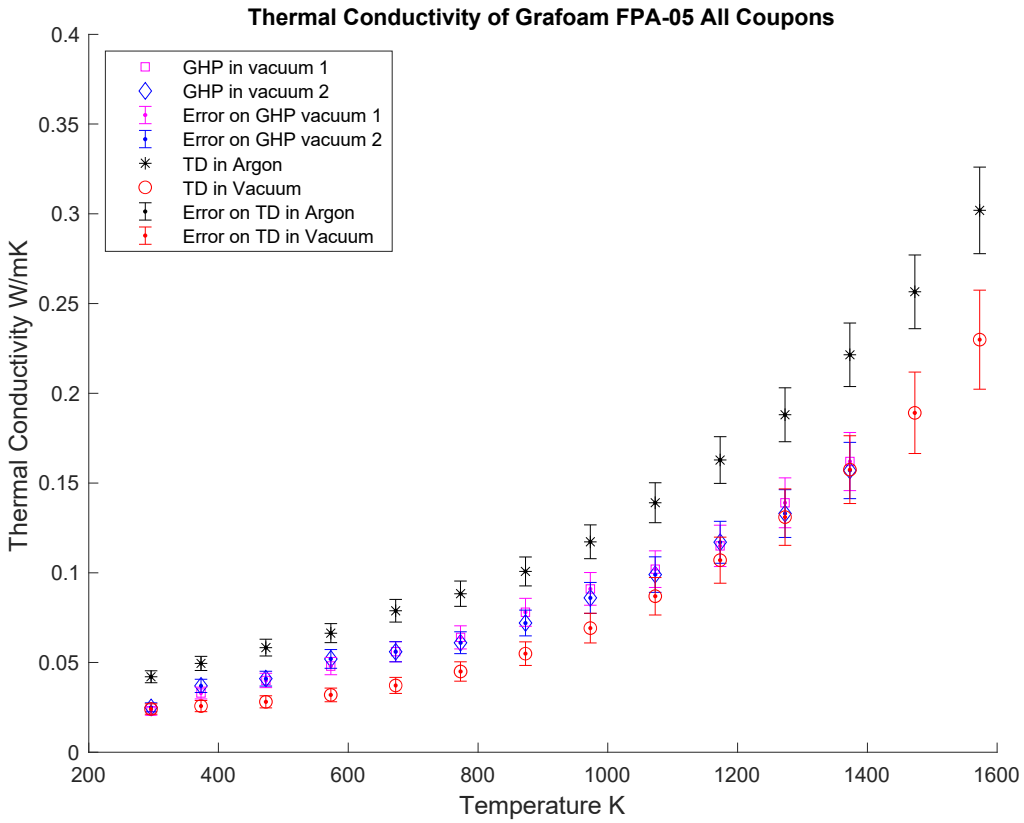

Figure C-3 Grafoam FPA-05 All Coupons

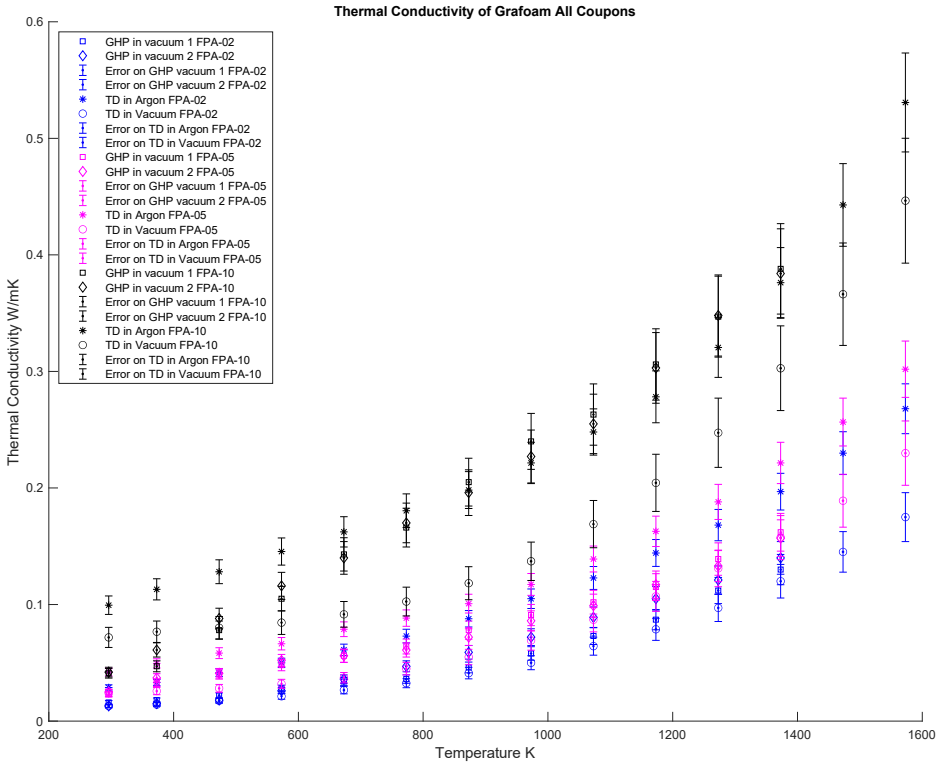

Figure C-4 Grafoam All Coupons

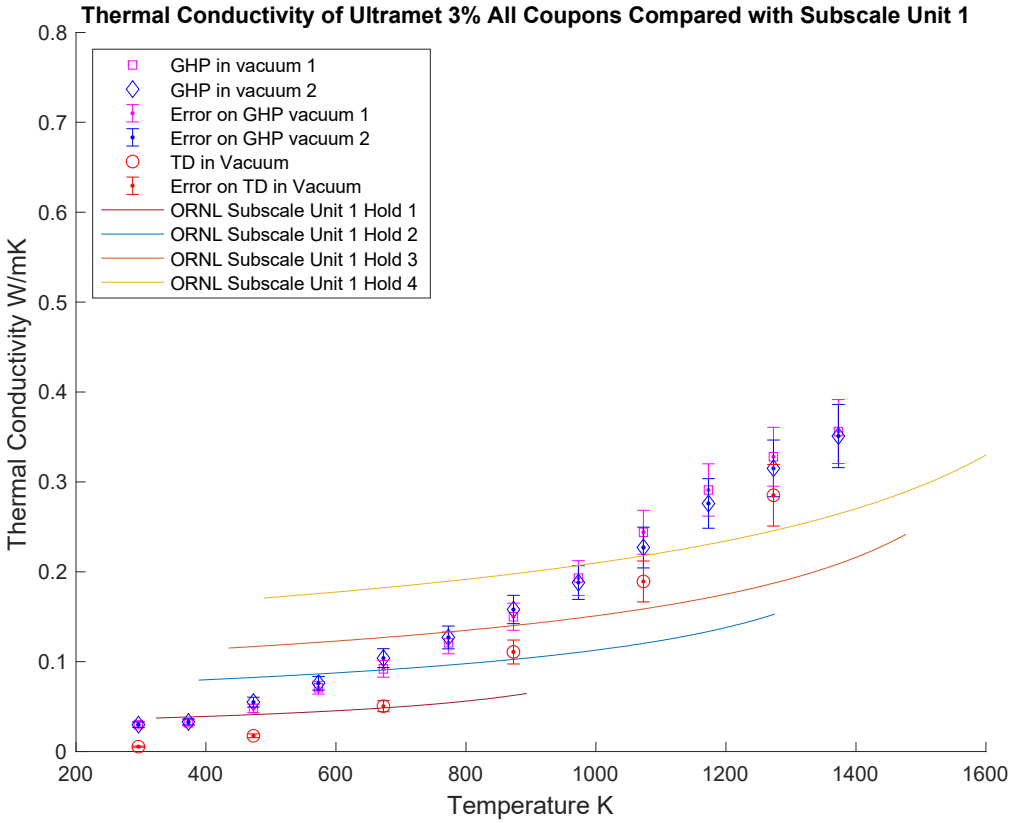

Figure C-5 Ultramet 100 ppi 3% Coupon and Subscale Unit 1 Data

VITA

Elizabeth Ann Congdon was born on May 20, 1986 in Roswell, GA to parents Katherine Bissell and Lee Congdon. She graduated from Summit High School in Summit, NJ in 2004 and attended Stanford University where she earned a Bachelor of Science in Mechanical Engineering in 2008. After graduating, she worked as a mechanical engineer for The Johns Hopkins Applied Physics Laboratory (JHUAPL) in the Mechanical Systems group and began her graduate work concurrently at Johns Hopkins University. Her work began at JHUAPL as the materials test lead for the Parker Solar Probe Spacecraft. In 2016, she assumed the role of Lead Engineer for the Parker Solar Probe Thermal Protection System and lead a team of eight people and multiple subcontractors to the delivery of the Flight TPS resulting in the successful launch of Parker Solar Probe on August 12, 2018. In 2019, she was named Chief Technologist for the Space Engineering Branch of the Space Sector.